POLITECNICO DI MILANO

Scuola di Ingegneria Industriale e dell'Informazione

Corso di Laurea in Ingegneria Aeronautica

DEVELOPMENT AND VALIDATION OF THE ANCHORING SYSTEM OF A BRIDGE SAFETY BARRIER NUMERICAL MODEL FOR CRASH TEST SIMULATIONS

Relatore: Prof. Marco ANGHILERI

Correlatore: Ing. Michele PITTOFRATI

Tesi di laurea di:

Giulio CALVETTI Matr. 783093

Anno Accademico 2013/2014

Sommario

In ambito di sicurezza stradale la modellazione numerica costituisce un importantissimo strumento di analisi e simulazione, che consente di ridurre i tempi e i costi particolarmente elevati che caratterizzano le fasi di progetto e ottimizzazione delle barriere di contenimento dei veicoli.
Data la particolare geometria delle barriere di bordo ponte, i modelli numerici maggiormente utilizzati per le simulazioni di crash test non possono essere considerati ben rappresentativi per questo tipo di strutture, in particolare per quanto riguarda il sistema di vincolo con il ponte.
Il lavoro svolto consiste nello sviluppo e nella successiva validazione di un modello numerico di barriera di sicurezza di bordo ponte per simulazioni di crash test, affidabile e ben rappresentativo della realtà fisica di queste strutture.
La realizzazione di tale modello è cominciata con la ricerca e la verifica di un'efficace metodo di modellazione del vincolo tra la barriera di sicurezza e la struttura sulla quale è installata, un metodo che tenesse conto di tutte le modalità di cedimento che possono aver luogo durante l'impatto con un veicolo.
Successivamente si è svolta la caratterizzazione del materiale, mediante una serie di test di compressione effettuati su provini standard di calcestruzzo, seguiti dallo sviluppo e dalla calibrazione dei relativi modelli numerici.
Il comportamento del vincolo e del materiale è stato poi verificato mediante una correlazione numerico-sperimentale di alcuni test full-scale.
In conclusione è stata effettuata una procedura di validazione del modello mediante lo svolgimento di simulazioni full-scale di crash test secondo la normativa europea EN 1317. È stato quindi in primis creato il modello completo di una barriera di sicurezza di bordo ponte realmente prodotta e testata, realizzato con le caratteristiche scelte e verificate in precedenza; i risultati ottenuti dalle simulazioni svolte su tale modello sono stati poi confrontati con quelli relativi ai crash test reali.

Parole chiave: barriere di bordo ponte, sistemi di ancoraggio, crash test, EN 1317, LS-Dyna®.

Abstract

In the framework of road safety, numerical modeling represents an important analysis and simulation tool, which allows to reduce the particularly high time and costs that characterize the design and optimization phases of vehicles containment systems.
Because of the bridge safety barriers peculiar geometry, the numerical models mostly used for crash test simulations cannot be considered as well representative for these type of structures, in particular concerning the linkage system with the bridge.
The work performed consists of the development and the following validation of a reliable and physically realistic bridge safety barrier numerical model for crash test simulations.
The development of such model began with the research and the verification of an effective method to model the link between the safety barrier and the structure on which it is installed, a method which took into account all the failure modalities that may occur during an impact with a vehicle.
Afterwards the material characterization has been carried out, through a series of compression tests performed on standard concrete specimens, followed by the development and the calibration of the correspondent numerical models.
The behavior of the link and the material has been then verified by means of a numerical-experimental correlation of several full-scale tests.
In conclusion, the model validation procedure has been performed through the fulfillment of full-scale crash test simulations according to the European standard EN 1317. Thus, the complete model of a bridge safety barrier actually built and tested has been firstly created, taking into account the characteristics previously chosen and verified; the results achieved from the simulations performed on this model have been eventually compared with the ones provided by the actual crash tests.

Keywords: bridge safety barriers, anchoring systems, crash tests, EN 1317, LS-Dyna®.

Estratto riassuntivo

Introduzione

Uno dei principali obiettivi nell'ambito del trasporto stradale è quello di assicurare agli utenti un adeguato livello di sicurezza.
Nel corso dell'ultimo decennio gli incidenti stradali sono stati causa in Italia di più di 50000 morti e tre milioni di feriti, determinando un inaccettabile costo in termini sia umani che economici.
Per contrastare questa situazione, l'impegno nel miglioramento della sicurezza stradale ha visto una forte crescita, caratterizzata da intense attività di ricerca e sviluppo di normative, con l'obiettivo di regolare e promuovere il concetto di sicurezza stradale, sia per quanto riguarda l'aspetto infrastrutturale che quello culturale.
La sicurezza, in ambito di trasporto stradale, può essere vista sotto due differenti punti di vista:

- Sicurezza attiva: serie di misure sviluppate al fine di evitare l'avvenimento dell'incidente; tra queste vi sono:

  - ABS (antilock brake system)
  - ESP (electronic stability program)
  - Limitatori di velocità
  - Campagne informative e di formazione
  - Criteri di progettazione per nuove strade
  - Miglioramenti di strade esistenti
  - Interventi infrastrutturali riguardanti pavimentazione, segnaletica, illuminazione, etc.

- Sicurezza passiva: serie di misure mirate a limitare i danni di un eventuale incidente; tra queste vi sono:

  - Cinture di sicurezza
  - Airbag
  - Obbligo del casco per motociclisti
  - Misure atte a garantire soccorsi sanitari tempestivi
  - Sistemi antincendio, rifugi e passaggi ausiliari (per lunghe gallerie), etc.
  - Sistemi di contenimento

Lo studio svolto per la stesura di questa tesi si concentra su uno degli elementi principali di sicurezza passiva, ossia i sistemi di contenimento dei veicoli e in particolare sulle barriere di sicurezza stradale installate su ponti in calcestruzzo.
Infrastrutture come ponti, viadotti e cavalcavia, sulle quali il veicolo è esposto al vuoto sottostante, sono caratterizzati da un elevato rischio in caso di incidente, decisamente più elevato rispetto a quanto concerne la comune accezione di sicurezza stradale.
Mente solitamente un erroneo comportamento di una barriera di sicurezza stradale, in caso di incidente ed eventuale superamento della stessa da parte del veicolo, non risulta necessariamente in un evento letale, il rischio che questo occorra è molto più alto se si parla di barriere di bordo ponte.
Questa è la ragione per cui le normative suggeriscono i livelli di contenimento più elevati per le barriere progettate per le infrastrutture in questione, a scapito di un eventuale maggiore severità del danno a carico degli occupanti del veicolo.
La storia degli incidenti stradali fornisce numerosi esempi delle disastrose conseguenze derivanti dal malfunzionamento di una barriera di bordo ponte.
Solitamente i suddetti esempi concernono veicoli pesanti come autoarticolati o autobus, essendo le barriere di bordo ponte, come detto, caratterizzate da un elevato livello di contenimento e quindi in grado di reindirizzare almeno veicoli leggeri come le automobili; teoricamente tali barriere dovrebbero essere progettate per contenere anche veicoli più pesanti, ma non sempre lo fanno, come nei seguenti casi avvenuti recentemente in Italia:

- Cesena (FC), 14 febbraio 2014.
- Siena, 13 ottobre 2013.
- Avellino, 28 luglio 2013.
- Cuneo, 22 luglio 2013.
- Sarezzo (BS), 18 giugno 2013.
- Caltanissetta, 24 aprile 2013.
- Cefalù (PA), 30 agosto 2012.
- Corato (BA), 18 aprile 2008.

Figura i. Esempio di incidente dovuto al malfunzionamento di una barriera di bordo ponte (Siena, 13 ottobre 2013).

L'obiettivo di questo lavoro è quindi quello di fornire un contributo al tema della sicurezza stradale, mediante lo sviluppo di un modello numerico affidabile di barriera di sicurezza di bordo ponte, da utilizzarsi per simulazioni di crash test. La simulazione numerica è un potente mezzo che permette oggi di minimizzare tempi e costi delle fasi di progetto e ottimizzazione delle barriere di sicurezza, riducendo la necessità di prove di crash reali, in questo campo estremamente lunghe e costose.
Lo sviluppo di tale modello è stato effettuato seguendo diversi passi:

- Studio e verifica di un'efficace tecnica per modellare numericamente il vincolo tra la barriera di sicurezza e la struttura sulla quale è installata, in modo da essere il più possibile fedele alla realtà fisica e da tenere conto di tutte le modalità di rottura che possono incorrere durante l'impatto di un veicolo.
- Caratterizzazione del materiale mediante una serie di test di compressione effettuati su provini standard in calcestruzzo, e successiva correlazione numerico-sperimentale dei corrispondenti modelli realizzati.
- Verifica del comportamento del vincolo e del materiale mediante correlazione numerico-sperimentale di alcuni test full-scale su paletti di barriera e su ancoranti.
- Validazione del modello sviluppato mediante lo svolgimento di simulazioni full-scale di crash test secondo la normativa europea EN 1317 e confronto con i risultati ottenuti dai crash test reali effettuati sulla medesima barriera.

Modellazione del sistema di ancoraggio della barriera

Il modello realizzato tiene conto di tutte le possibilità di cedimento contemplate per la struttura, ossia degli elementi metallici della barriera, incluse le varie bullonature presenti in essa, del cordolo di calcestruzzo e del vincolo tra quest'ultimo e gli ancoranti ad esso vincolati.
I modelli numerici per simulazioni di crash test utilizzati nella quasi totalità dei casi risultano rappresentativi per comuni barriere di sicurezza stradali, i cui paletti sono immersi nel terreno per una lunghezza definita; in questi casi il modello viene realizzato mediante una delle seguenti tecniche:

- Gli spostamenti e le rotazioni dei nodi della parte dei paletti immersa nel terreno vengono vincolati; si può eventualmente tenere conto della deformabilità del terreno non vincolando l'intera lunghezza immersa.
- La deformabilità del terreno può essere rappresentata da un set di molle non lineari, la cui rigidezza può essere funzione della profondità, delle caratteristiche del suolo, dello schiacciamento o della geometria del paletto; esse vengono vincolate alla parte immersa dei paletti.
- Il terreno può essere modellato come un qualunque elemento strutturale, creando dei volumi solitamente cilindrici che circondano la parte interrata di ogni paletto, discretizzandoli poi mediante elementi solidi e definendo opportunamente le proprietà del materiale.

Nessuno di questi modelli può essere considerato rappresentativo di una barriera di sicurezza di bordo ponte, il cui sistema di ancoraggio è completamente diverso; questo è infatti composto da una piastra orizzontale forata sulla quale il paletto è saldato (non vi è quindi alcuna parte interrata di quest'ultimo), e da un numero di bulloni ancoranti, o tirafondo, che varia in genere da tre a sei.
Vi sono una serie di metodi semplificati per rappresentare una struttura siffatta ma il modello realizzato durante questo lavoro è in grado di rappresentare correttamente tutti gli elementi dai quali è composta, considerandone le interazioni e le possibilità di cedimento.
In particolare, è stata scelta una particolare funzione disponibile nel software utilizzato per la modellazione numerica della barriera, LS-Dyna®, denominata *CONTACT_TIED_SURFACE_TO_SURFACE_FAILURE, per rappresentare l'interazione tra i tirafondo e il cordolo di calcestruzzo al quale sono vincolati mediante incollaggio chimico. Entrambe le due parti in questione sono state modellate con elementi solidi e l'introduzione del particolare contatto sopracitato per modellarne l'interazione consente di considerare la possibilità di distacco l'una dall'altra, come se la resina utilizzata cedesse sotto un carico eccessivo. La scheda del contatto consente infatti l'introduzione di uno sforzo

assiale e uno di taglio a rottura, raggiunti i quali le due superfici a contatto vengono distaccate.
L'affidabilità di questa rappresentazione è stata testata mediante due prove in cui un tirafondo è stato "incollato" a un blocco metallico tramite il contatto con cedimento descritto, prima sulla superficie di base poi su quella laterale, imponendo uno sforzo di cedimento dell'incollaggio di valore arbitrariamente pari a 100 N/mm^2. I risultati sono visibili nelle Figure ii e iii.

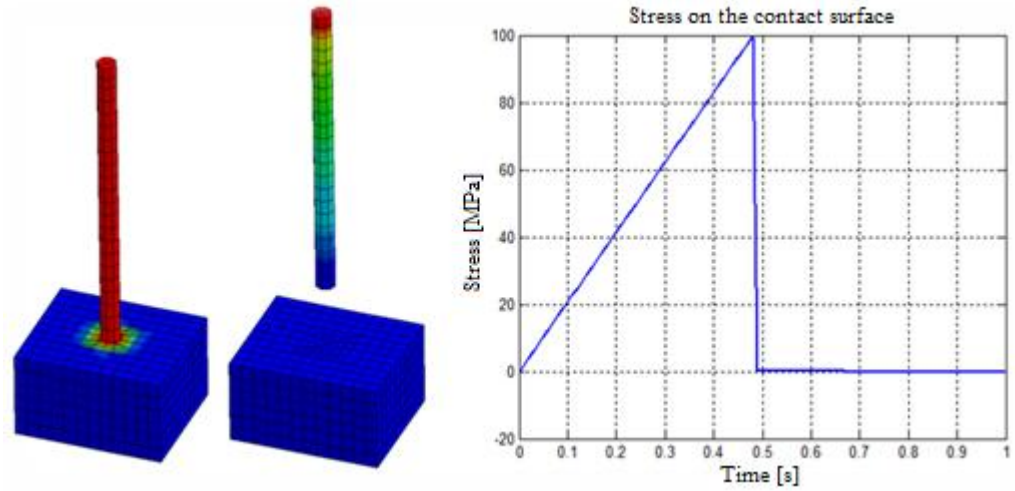

Figura ii. Primo test di funzionalità del contatto. Il grafico riporta l'andamento nel tempo dello sforzo sulla superficie di contatto.

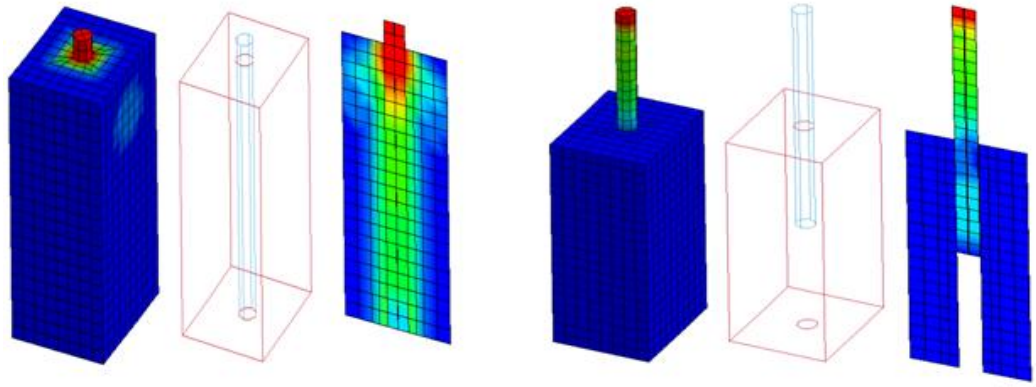

Figura iii. Secondo test di funzionalità del contatto. È visibile la trasmissione dello sforzo fra le due parti fino al distacco delle stesse.

Per una maggiore accuratezza del modello, in particolare della distribuzione delle sollecitazioni in esso presenti, è stato introdotto un precarico nei tirafondo, per tenere conto del fatto che questi sono sottoposti a uno sforzo dato dalla torsione dei dadi.

Questo è stato fatto sfruttando una funzione di LS-Dyna® nota come dynamic relaxation; si tratta di una fase di calcolo preliminare che consente di introdurre uno stato di precarico stazionario iniziale dal quale poi viene fatta partire la successiva analisi vera e propria.
L'introduzione del precarico negli elementi solidi con cui i tirafondo sono stati modellati è stata realizzata sfruttando le caratteristiche di dilatazione e contrazione termica tipiche dei metalli. Associando quindi un coefficiente di dilatazione termica all'acciaio è stato imposto un abbassamento di temperatura, il quale ha causato una contrazione dei tirafondo che, essendo vincolati, sono risultati sottoposti a uno sforzo. Il calcolo dello sforzo da imporre è stato fatto mediante formule empiriche che tengono conto delle caratteristiche geometriche del filetto, delle dimensioni dell'ancorante, dell'attrito e della coppia torcente applicata.

Caratteristiche e modellazione del calcestruzzo

Il calcestruzzo è un materiale composito dal comportamento molto complesso. Si può definire tale in quanto è costituito da numerosi componenti, i cui tre principali sono:

- Aggregati: elementi rocciosi di differente diametro, che varia dai decimi alle decine di millimetri, che conferiscono gran parte della resistenza strutturale.
- Cemento: funge da legante per gli aggregati.
- Acqua: a contatto con il cemento forma un composto semiliquido modellabile; a seguito dell'idratazione si ottiene un materiale roccioso solido.

Altri elementi che possono essere aggiunti per conferire differenti caratteristiche sono: rinforzi, acceleranti o ritardanti di idratazione, elasticizzanti, inibitori di corrosione, leganti, pigmenti, etc.
Il calcestruzzo viene classificato in base a diverse caratteristiche, che possono essere la resistenza, l'esposizione, la consistenza; la più interessante dal punto di vista del lavoro svolto è la prima.
La resistenza del calcestruzzo viene determinata mediante test di compressione effettuati su provini cubici di lato 150 mm o su provini cilindrici di diametro 150 mm e altezza 300 mm; si ottengono così la resistenza caratteristica a compressione cubica, R_{ck}, e la resistenza caratteristica di compressione

cilindrica, $f_{ck,}$ mediante le quali si identificano 18 classi di resistenza, denominate mediante sigle nella forma C f_{ck}/R_{ck}.
Il calcestruzzo ha un comportamento meccanico particolare, presentandosi molto resistente in compressione, grazie alla presenza degli aggregati, e molto debole in trazione, carenza che viene spesso sopperita mediante l'uso di rinforzi metallici, con cui si realizza il cosiddetto cemento armato.
La curva σ-ε del materiale, molto diversa da quella dei metalli, presenta i tre campi caratteristici visibili in Figura iv. Il campo blu rappresenta l'iniziale comportamento elastico, che obbedisce approssimativamente alla legge di Hooke, quello rosso rappresenta il campo plastico e quello verde rappresenta il danneggiamento.

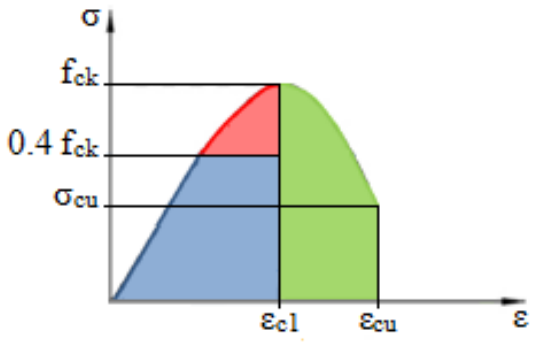

Figura iv. Tipica curva σ-ε del calcestruzzo.

Per quanto riguarda la rappresentazione del cordolo di calcestruzzo presente nel modello di barriera, il software LS-Dyna® fornisce differenti modelli di materiale, ognuno con diverse caratteristiche che lo rendono idoneo a una particolare applicazione.
Per la struttura in questione è stato scelto il modello denominato *MAT_CSCM_CONCRETE.
Esso definisce nello spazio degli sforzi principali una superficie di rottura e una superficie limite di elasticità tridimensionali, che si sviluppano attorno all'asse idrostatico.

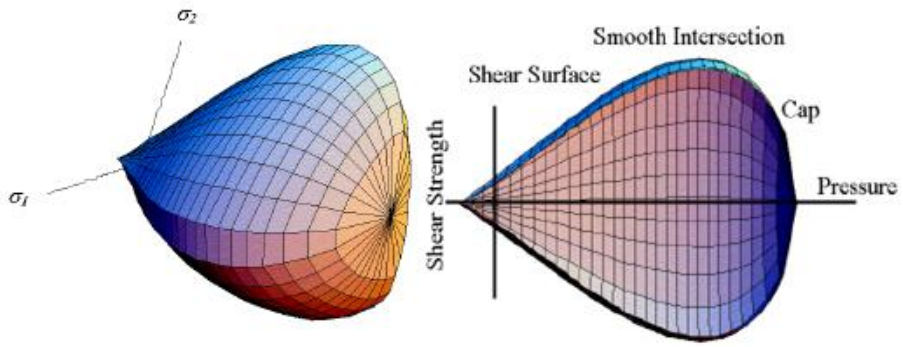

Figura v. Rappresentazione della superficie limite di elasticità.

Qualsiasi configurazione di sforzo definita da un punto interno alla superficie di rottura rappresenta uno stato non danneggiato del materiale.
La superficie di rottura costituisce invece tutti gli stati di sforzo in corrispondenza dei quali il materiale raggiunge la sua resistenza limite; una volta superata, il danneggiamento comincia.

Prove di caratterizzazione del materiale

La caratterizzazione del materiale è stata svolta mediante una serie di test di compressione effettuati su provini standard in calcestruzzo; successivamente, allo scopo di verificare e validare il modello di materiale scelto, è stata effettuata la correlazione numerico-sperimentale dei corrispondenti modelli realizzati.
I test sperimentali in corso di svolgimento sono i seguenti:

- Test di compressione uniassiale su provini cubici
- Test di compressione uniassiale su provini cilindrici
- Test di compressione idrostatica su provini cilindrici
- Test di compressione triassiale su provini cilindrici
- Test di estensione triassiale su provini cilindrici
- Test di deformazione uniassiale su provini cilindrici

La correlazione numerico-sperimentale è stata effettuata per i primi due test.

<u>Test di compressione uniassiale su provini cubici</u>

Questa prova è stata svolta su tre gruppi di cinque provini di calcestruzzo di lato 150 mm; i gruppi sono caratterizzati da una composizione diversa ma la classe di appartenenza è per tutti C30/37.

I risultati ottenuti da questa prova sono la resistenza caratteristica a compressione R_{ck} di questi provini e la forma da essi assunta a rottura.
I valori di resistenza ottenuti sono riportati nelle Tabelle i, ii e iii.

Tabella i. Risultati dei test sui provini di tipo MC(0.45) – CEM I 52.2.

MC(0.45) – CEM I 52.2					
Provino	**Massa [Kg]**	**Dimensioni [mm]**	**Densità [Kg/m^3]**	**Carico rottura [kN]**	**Sforzo rottura [MPa]**
1	7.85	150x150x150	2330	1500	66.7
2	7.85	150x150x150	2330	1415	62.9
3	7.80	150x150x150	2310	1455	64.7
4	7.85	150x150x150	2330	1500	66.7
5	8.10	153x150x150	2350	1515	66.0
Sforzo di rottura medio: R_{ck} = 65.4 MPa					

Tabella ii. Risultati dei test sui provini di tipo MC(0.50) – CEM I 52.2.

MC(0.50) – CEM I 52.2					
Provino	**Massa [Kg]**	**Dimensioni [mm]**	**Densità [Kg/m^3]**	**Carico rottura [kN]**	**Sforzo rottura [MPa]**
1	7.60	147x150x150	2300	1250	56.7
2	7.85	150x150x150	2330	1330	59.1
3	7.65	148x150x150	2300	1225	55.2
4	7.60	147x150x150	2300	1260	57.1
5	7.80	150x150x150	2310	1300	57.8
Sforzo di rottura medio: R_{ck} = 57.2 MPa					

Tabella iii. Risultati dei test sui provini di tipo MC(0.45) – CEM I 42.2.

MC(0.45) – CEM I 42.2					
Provino	**Massa [Kg]**	**Dimensioni [mm]**	**Densità [Kg/m^3]**	**Carico rottura [kN]**	**Sforzo rottura [MPa]**
1	7.75	150x150x150	2300	1180	52.4
2	7.70	150x150x150	2290	1190	52.9
3	7.80	150x150x150	2310	1160	51.6
4	7.70	150x150x150	2280	1150	51.1
5	7.75	150x150x150	2300	1170	52.0
Sforzo di rottura medio: R_{ck} = 52.0 MPa					

La Figura vi fornisce un'idea sulla dispersione dei dati per quanto concerne questa prova.

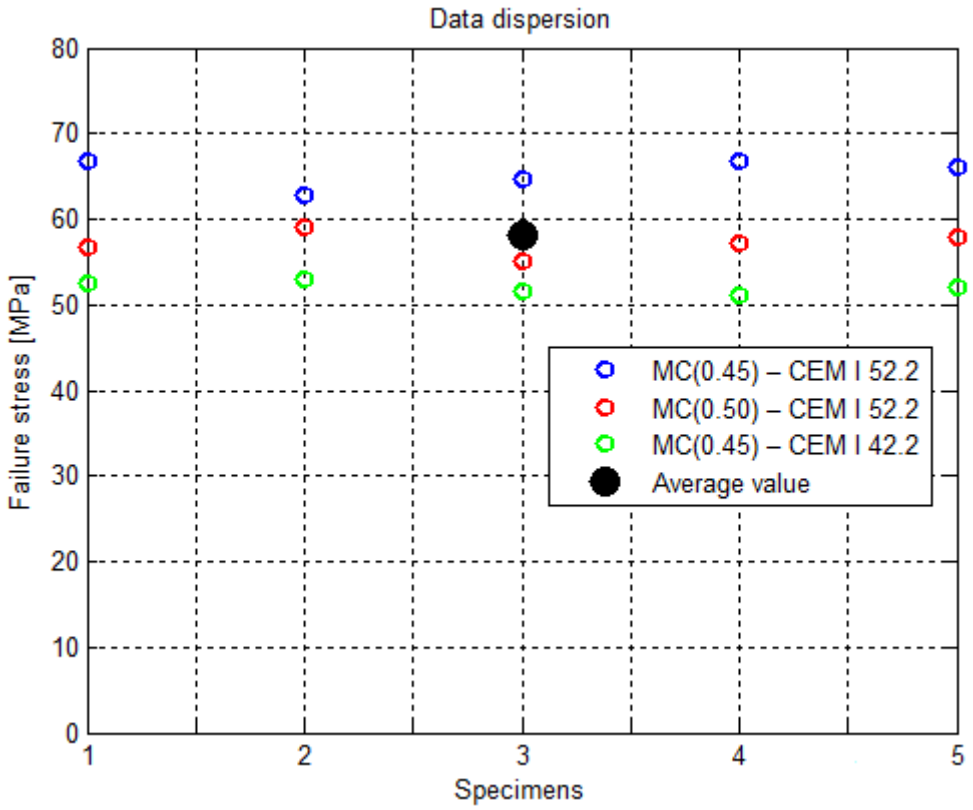

Figura vi. Dispersione dei dati relativi al test di compressione su provini cubici.

La ragione dell'elevata resistenza di questi provini, molto superiore al valore teorico di 37 MPa è riconducibile all'ottima qualità degli stessi, i quali sono stati prodotti seguendo rigidamente la normativa, miscelando i componenti in perfetta quantità e lasciandoli riposare per 28 giorni in condizioni ideali, ossia in acqua alla temperatura di 20 °C. Le strutture in calcestruzzo tipicamente presentano una resistenza inferiore in quanto durante la loro produzione queste condizioni non possono essere rispettate così rigorosamente.

In generale si può dire che 37 MPa è la resistenza minima garantita per questa classe, ma che generalmente la resistenza di una struttura è molto variabile in un intervallo superiore a questo valore, a seconda di varie caratteristiche come la qualità e le condizioni operative.

In Figura vii è visibile un confronto fra il modello sperimentale e quello numerico al momento della rottura; è individuabile una forma di rottura a clessidra.

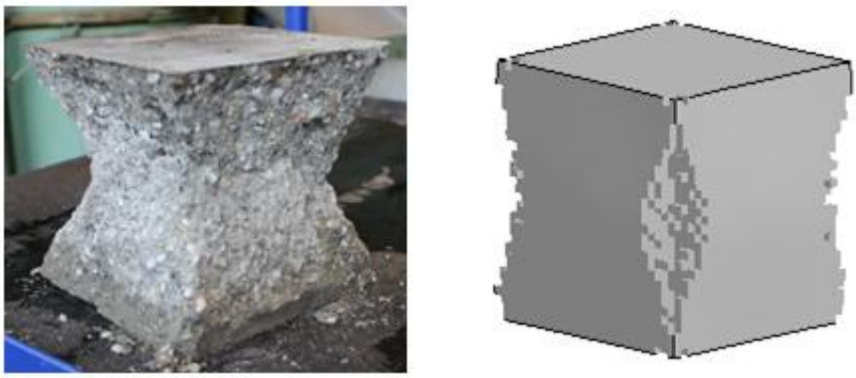

Figura vii. Confronto tra le modalità di rottura dei provini cubici nei casi sperimentale e numerico.

La Tabella iv mette a confronto le tre resistenze a compressione di questo materiale: teorica, numerica e sperimentale (media).

Tabella iv. Confronto tra i valori teorico, numerico e sperimentale di R_{ck}.

	Teoria	**Simulazione numerica**	**Prove sperimentali**
R_{ck} [MPa]	37	36.88	58.2

Test di compressione uniassiale su provini cilindrici

I risultati ottenuti da questa prova sono:

- La resistenza a compressione dei provini f_{ck}
- L'andamento dello sforzo assiale in funzione della deformazione assiale (curva σ_1-ε_1)
- L'andamento dello sforzo assiale in funzione della deformazione trasversale (curva σ_1-ε_3)
- La forma dei provini a rottura

I valori di resistenza ottenuti per questi provini sono riportati in Tabella v e in Figura viii, che fornisce anche la dispersione dei dati per questa prova.

Tabella v. Risultati dei test di compressione sui provini cilindrici.

Provino	Massa [g]	Diametro [mm]	Altezza [mm]	Densità [Kg/m^3]	Sforzo rottura [MPa]
1	424.44	5.05	9.448	2243	31.90
2	450.85	5.05	9.909	2272	27.80
3	451.88	5.05	10.06	2242	26.40
4	55.72	2.38	5.599	2237	31.60
5	55.54	2.38	5.66	2206	21.90
6	55.49	2.383	5.603	2221	31.10
7	55.81	2.38	5.519	2273	23.72
Sforzo di rottura medio: f_{ck} = 27.77 MPa					

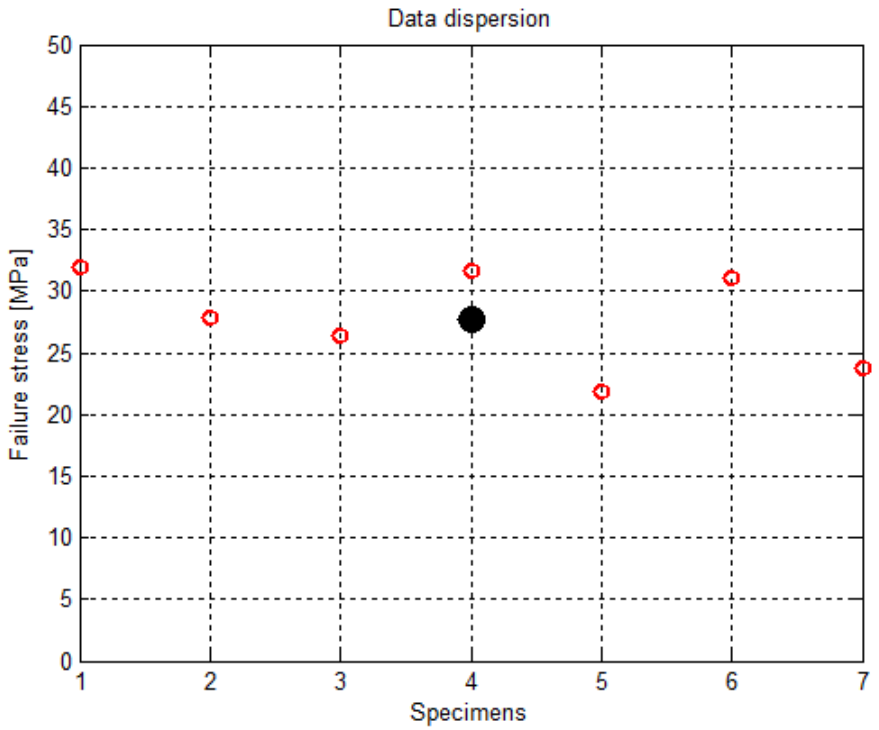

Figura viii. Dispersione dei dati relativi al test di compressione su provini cilindrici.

Le Figure ix e x riportano l'andamento dello sforzo assiale in funzione delle deformazioni assiale e trasversale per questo test.

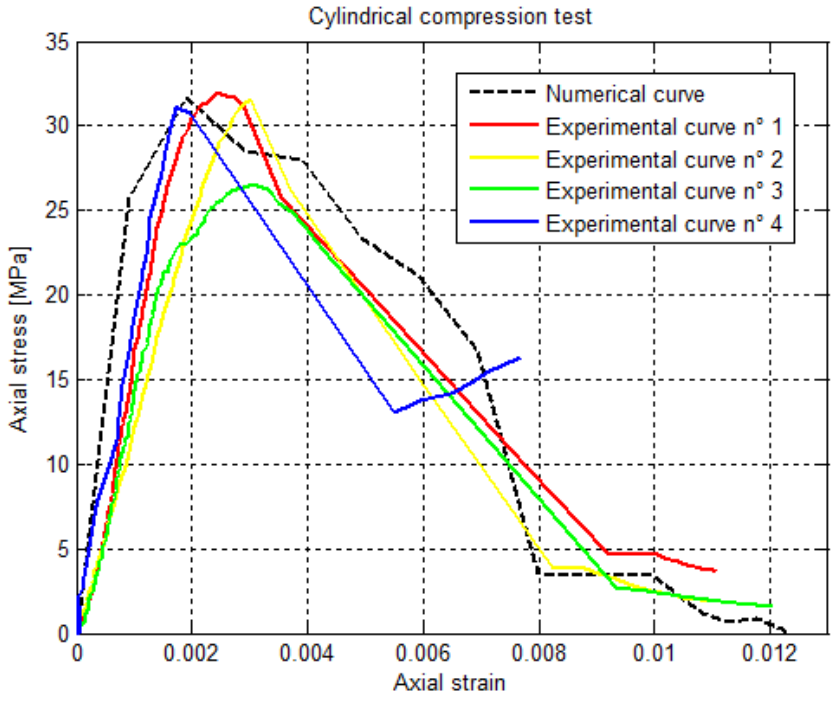

Figura ix. Confronto numerico-sperimentale della curva σ_1-ε_1.

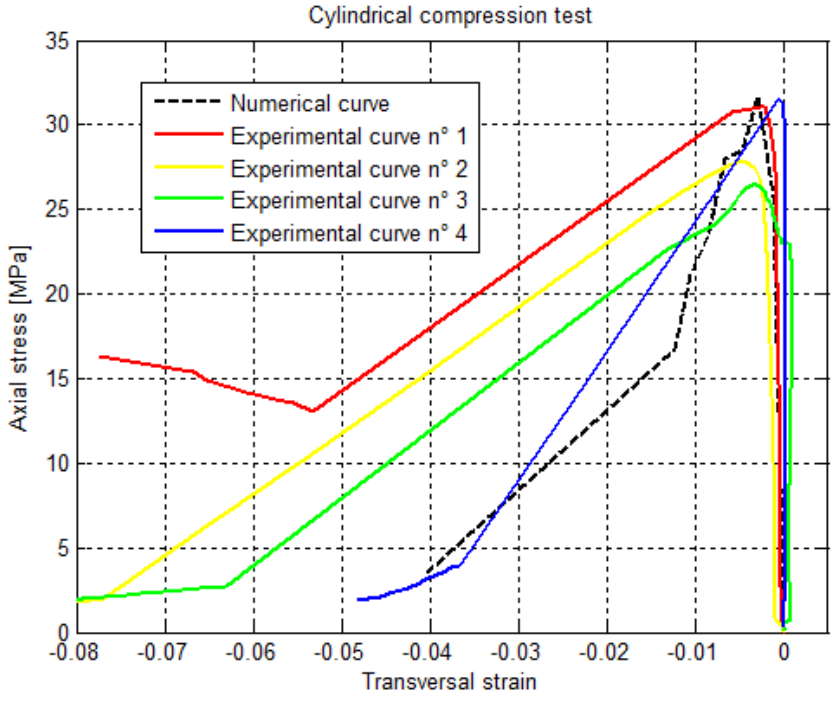

Figura x. Confronto numerico-sperimentale della curva σ_1-ε_3.

In Figura xi è visibile il confronto numerico-sperimentale della rottura dei provini per questo test.

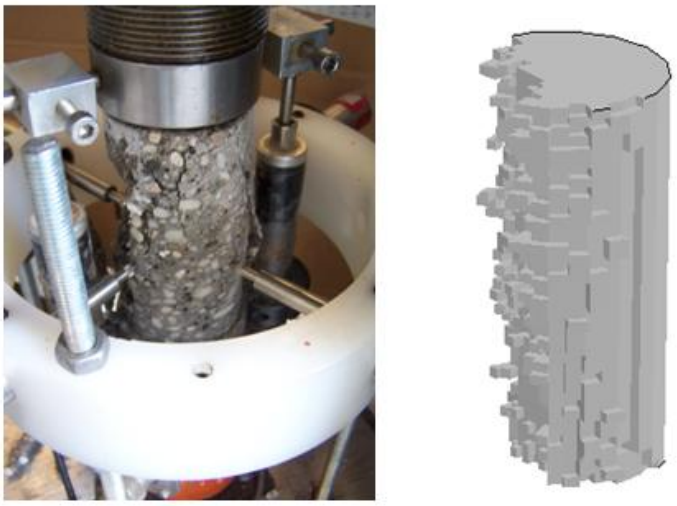

Figura xi. Confronto tra le modalità di rottura dei provini cilindrici nei casi sperimentale e numerico.

La Tabella vi confronta i tre valori della resistenza a compressione per questa prova: teorico, numerico e sperimentale (medio).

Tabella vi. Confronto tra i valori teorico, numerico e sperimentale di f_{ck}.

	Teoria	**Simulazione numerica**	**Test sperimentale**
f_{ck} [MPa]	30	31.63	27.77

Il valori sperimentali ottenuti in questo caso sono molto più vicini alla teoria rispetto al caso precedente; la maggior resistenza dei provini cubici rispetto a quelli cilindrici è dovuta al fatto che questi ultimi, molto più snelli, sono meno soggetti allo sforzo di confinamento laterale, che contribuisce ad aumentare la forza necessaria per portare a rottura il provino.
In alcuni casi si è ottenuta addirittura una resistenza a compressione inferiore al valore minimio garantito di 30 MPa, fatto probabilmente dovuto a un micro-danneggiamento del provino durante il carotaggio.

Confronto numerico-sperimentale di test full-scale

Successivamente sono state realizzate e calibrate le rappresentazioni numeriche delle seguenti prove sperimentali:

- Spinta di un paletto C125 ancorato in un blocco di calcestruzzo
- Spinta di un paletto HEA120 ancorato in un blocco di calcestruzzo
- Trazione assiale contemporanea di due tirafondo ancorati in un blocco di calcestruzzo

Mentre nella prima prova si è assistito alla sola rottura del paletto, senza evidenti danni al calcestruzzo, particolarmente interessanti ai fini dello studio del comportamento di questo materiale sono risultate le altre due prove.
I risultati vengono mostrati qui di seguito, riportando un confronto fra le modalità di rottura e tra le forze in gioco; in particolare nel primo caso sono state misurate la forza imposta dalla macchina e le forze assiali agenti sui quattro tirafondo, nel secondo caso solo le forze agenti sui tirafondo e nel terzo caso solo la forza imposta dalla macchina.
I risultati della prova di tiro del paletto C125 sono i seguenti:

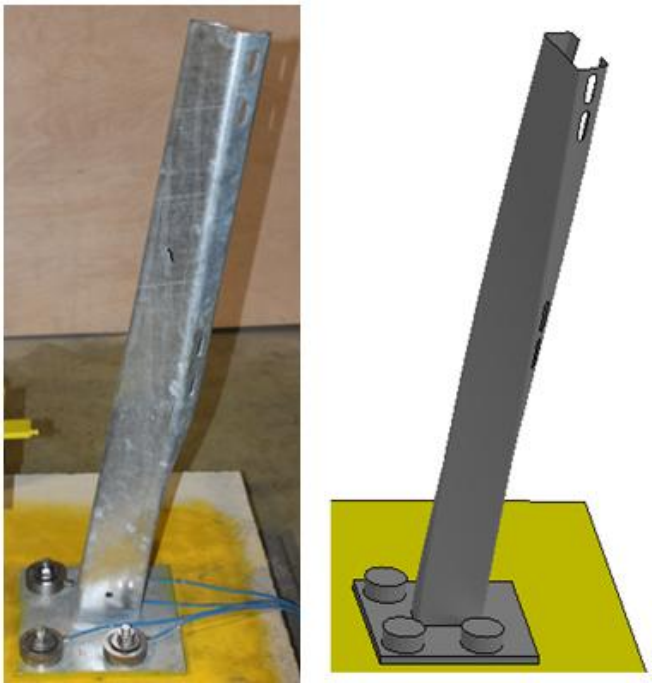

Figura xii. Confronto numerico-sperimentale della modalità di cedimento del paletto C125.

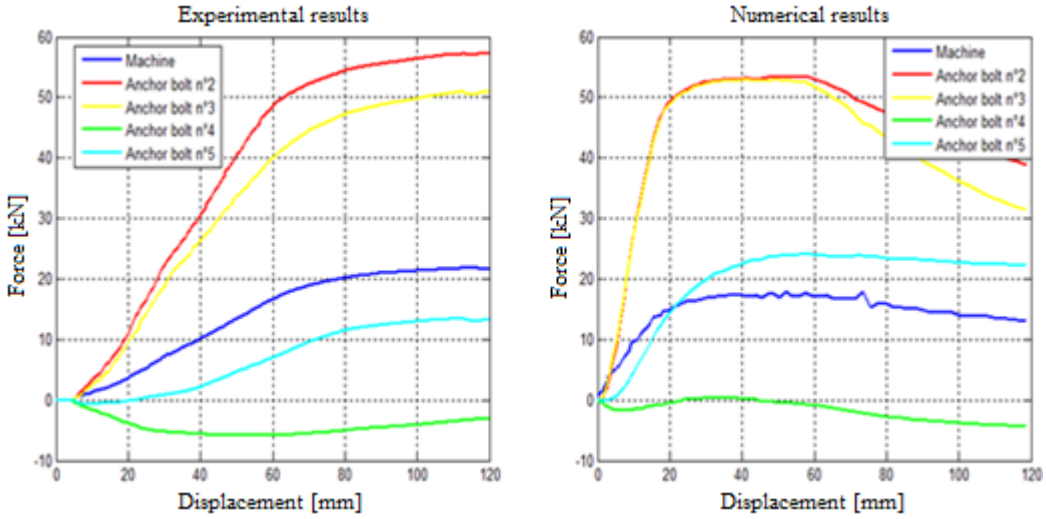

Figura xiii. Confronto numerico-sperimentale delle forze misurate durante il test sul paletto C125: carico imposto e forze agenti sui tirafondo in funzione dello spostamento.

I risultati della prova di tiro del paletto HEA120 sono i seguenti:

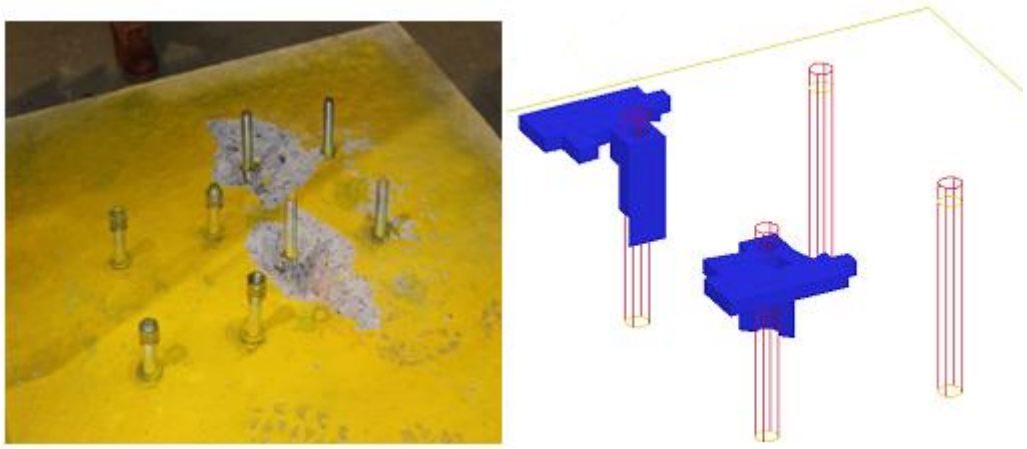

Figura xiv. Confronto numerico-sperimentale della modalità di cedimento del paletto HEA120.

Nel modello numerico gli elementi evidenziati in blu sono quelli danneggiati.

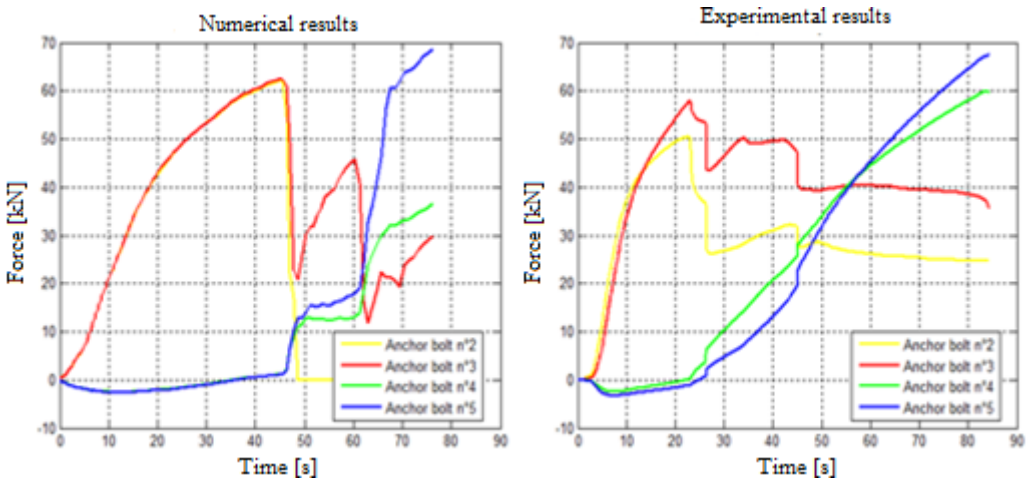

Figura xv. Confronto numerico-sperimentale delle forze misurate durante il test sul paletto HEA120: forze agenti sui tirafondo in funzione dello spostamento.

I risultati della prova di trazione assiale dei due tirafondo sono i seguenti:

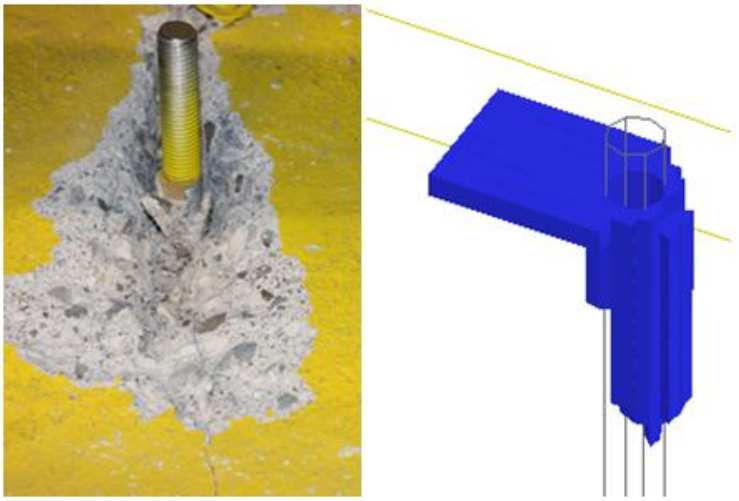

Figura xvi. Confronto numerico-sperimentale della modalità di cedimento dei tirafondo.

Come in precedenza, vengono evidenziati in blu gli elementi che subiscono danneggiamento.

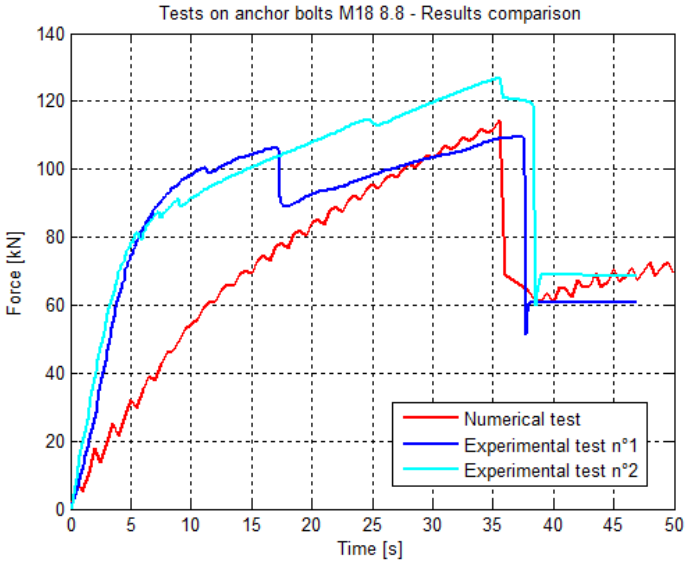

Figura xvii. Confronto numerico-sperimentale della forza di trazione imposta sui tirafondo.

Validazione del modello mediante prove full-scale di crash test

Il lavoro è stato infine completato con due simulazioni full-scale di crash test: è stato in primis realizzato il modello numerico di una barriera di bordo ponte prodotta e testata realmente; successivamente tale modello è stato utilizzato per simulare due prove di crash in accordo con la normativa EN 1317 e i risultati ottenuti sono stati confrontati con quelli sperimentali.

Le barriere di sicurezza stradale vengono classificate in base al loro livello di contenimento, ossia alla massima energia cinetica relativa alla componente della velocità del veicolo perpendicolare alla direzione di sviluppo della barriera che sono in grado di assorbire; il livello di contenimento è quindi definito come segue:

$$L_c = \frac{1}{2} \cdot M \cdot (V \cdot \sin\theta)^2$$

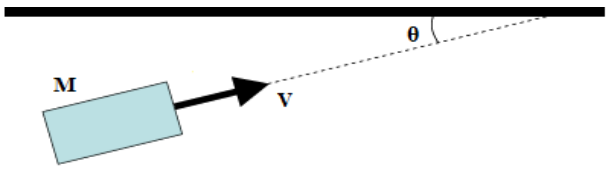

Figura xviii. Schema rappresentativo del calcolo del livello di contenimento.

In Figura xviii M è la massa del veicolo, V la sua velocità e θ l'angolo d'impatto. In base al livello di contenimento si definiscono le classi elencate in Tabella vii.

Tabella vii. Livelli di contenimento delle barriere stradali.

Classe	L_c [kJ]	Test di validazione
T1	6	TB21
T2	21	TB22
T3	37	TB41 – TB21
N1	44	TB31
N2	82	TB32 – TB11
H1	127	TB42 – TB11
H2	288	TB51 – TB11
H3	463	TB61 – TB11
H4a	572	TB71 – TB11
H4b	724	TB81 – TB11
L1	127	TB42 – TB32 – TB11
L2	288	TB51 – TB32 – TB11
L3	463	TB61 – TB32 – TB11
L4a	572	TB71 – TB32 – TB11
L4b	724	TB81 – TB32 – TB11

La terza colonna della Tabella vii riporta i test necessari alla verifica del livello di contenimento di una barriera; questi vengono effettuati facendo impattare contro la barriera da testare differenti tipi di veicolo a determinate velocità e angoli d'impatto, come definito in Tabella viii.

Tabella viii. Test di validazione dei livelli di contenimento delle barriere stradali.

Codice	Veicolo	Massa [ton]	Velocità [km/h]	Angolo d'impatto [°]
TB11	Automobile	0.9	100	20
TB21	Automobile	1.3	80	8
TB22	Automobile	1.3	80	15
TB31	Automobile	1.5	80	20
TB32	Automobile	1.5	110	20
TB41	Autocarro rigido	10	70	8
TB42	Autocarro rigido	10	70	15
TB51	Bus	13	70	20
TB61	Autocarro rigido	16	80	20
TB71	Autocarro rigido	30	65	20
TB81	Autoarticolato	38	65	20

La severità di un impatto tra un veicolo e una barriera di sicurezza viene determinata mediante una valutazione dei danni che occorrono all'occupante, alla barriera e al veicolo.
I danni all'occupante vengono determinati mediante i seguenti indici:

- ASI – Acceleration severity index: è un parametro che tiene conto delle accelerazioni del veicolo nelle tre direzioni durante l'impatto, valutate in un intervallo di 50 ms e normalizzate in base a valori limite.

$$\mathrm{ASI} = \sqrt{\left(\frac{a_x}{\hat{a}_x}\right)^2+\left(\frac{a_y}{\hat{a}_y}\right)^2+\left(\frac{a_z}{\hat{a}_z}\right)^2}$$

  $\hat{a}_x$ = 12 g
  $\hat{a}_y$ = 9 g
  $\hat{a}_z$ = 10 g
- THIV – Theoretical Head Impact Velocity: è un parametro utilizzato per valutare la severità dell'impatto sulla testa dell'occupante del veicolo, considerata come un oggetto che si muove liberamente quando il veicolo cambia la sua velocità finché non impatta contro una superficie interna dello stesso.

$$\mathrm{THIV} = \sqrt{v_x(t)^2+v_y(t)^2}$$

  v_x e v_y sono le componenti della velocità della testa nel sistema di riferimento del veicolo. THIV deve essere inferiore a 33 km/h.
- PHD – Post-impact Head Deceleration: è un parametro che descrive l'entità della decelerazione della testa dopo l'impatto. Deve essere inferiore a 20 g; è stato recentemente eliminato perché considerato fortemente dipendente dal tipo di veicolo.

$$\mathrm{PHD} = \sqrt{a_x(t)^2+a_y(t)^2}$$

A seconda del valore di tali indici si definiscono tre classi di severità dell'impatto, riportate in Tabella ix.

Tabella ix. Livelli di severità di un impatto.

Livello di severità dell'impatto	Indici		
	ASI	THIV	PHD
A	≤ 1.0	≤ 33 km/h	≤ 20 g
B	≤ 1.4	≤ 33 km/h	≤ 20 g
C	≤ 1.9	≤ 33 km/h	≤ 20 g

I danni alla barriera vengono determinati mediante i seguenti indici:

- Working width (W) – Distanza tra il lato della barriera rivolto verso la carreggiata e la massima posizione laterale raggiunta da un qualunque punto della barriera durante l'impatto.
- Dynamic Deflection (D) – Massimo spostamento laterale subito dal lato della barriera rivolto verso la carreggiata.
- Vehicle Intrusion (VI) – Massima posizione laterale raggiunta da un qualsiasi punto del veicolo durante l'impatto, considerata a partire dalla posizione del lato della barriera rivolto verso il traffico prima dell'impatto.

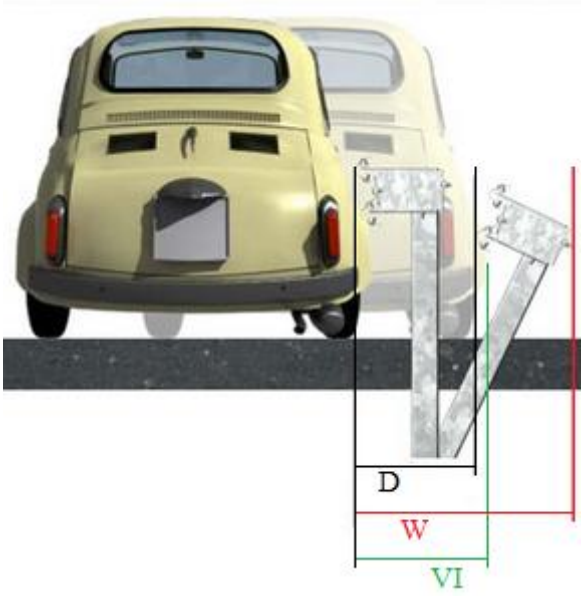

Figura xix. Parametri di deformazione della barriera: Working Width, Dynamic Deflection e Vehicle Intrusion.

La barriera di sicurezza di bordo ponte considerata per la realizzazione delle simulazioni full-scale appartiene alla classe di contenimento H4b ed è stata quindi testata mediante le prove designate dai codici TB11 e TB81.

La barriera in questione, mostrata in Figura xx, è composta da diversi elementi e materiali, riassunti in Tabella x.

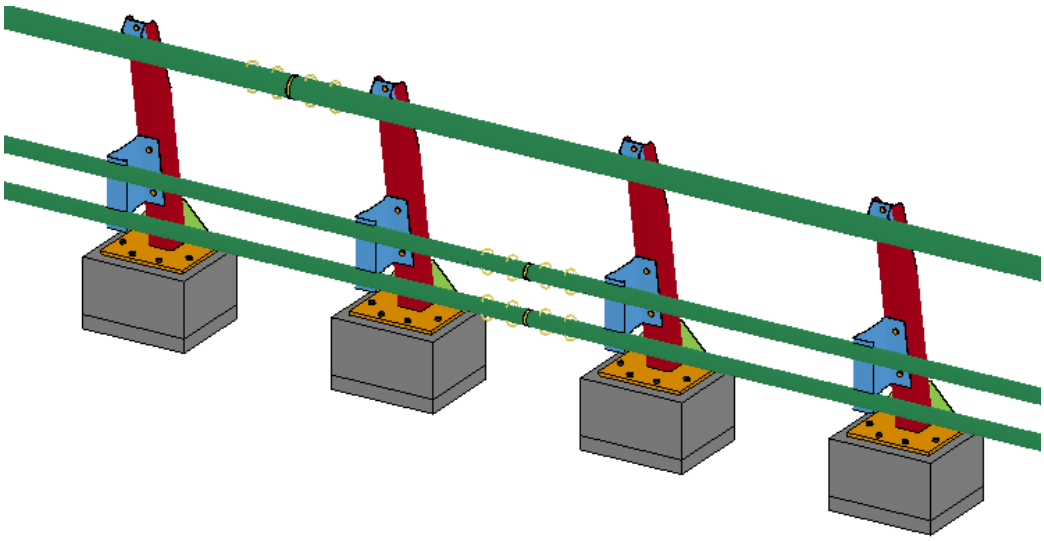

Figura xx. Modello numerico della barriera realizzato per le simulazioni di crash test.

Tabella x. Elementi e materiali della barriera di bordo ponte testata.

Elementi	Materiali
Paletti	S355-MC
Rinforzi triangolari	S355-MC
Piastre	S355-MC
Ancoranti	Acciaio di classe 8.8
Distanziatori	S355-MC
Tubi	S355-JRH
Elementi di connessione (tubi inferiori)	S235-JRH
Elementi di connessione (tubo superiore)	S335-JRH
Bullonature	Acciaio di classe 8.8

Il cordolo è stato realizzato con un calcestruzzo di classe C30/37, mediante il modello *MAT_CSCM_CONCRETE; l'interazione tra quest'ultimo e i tirafondo e il precarico dovuto alla torsione sono stati introdotti secondo le modalità precedentemente descritte.

Come test preliminare è stata effettuata una prova di spinta sul singolo paletto, ripetuta per tre volte e riprodotta numericamente.

Dal confronto numerico-sperimentale è emersa una modalità di cedimento identica, che vede la rottura del materiale concentrarsi in un punto sopra i rinforzi triangolari; in Figura xxi sono visibili lo sforzo di Von Mises e la deformazione plastica.

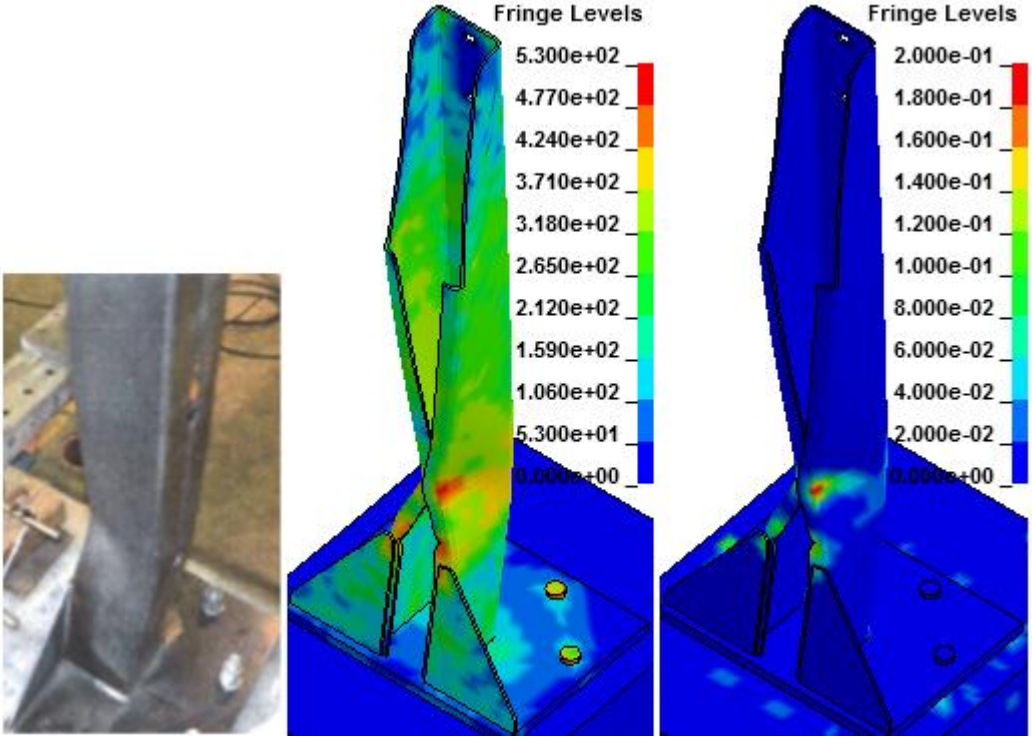

Figura xxi. Confronto numerico-sperimentale della modalità di cedimento del paletto di barriera: caso sperimentale (a sinistra), sforzo di Von Mises (al centro) e deformazione plastica (a destra).

I grafici in Figura xxii mostrano un confronto fra l'andamento della forza imposta in funzione dello spostamento nei tre casi sperimentali e in quello numerico.

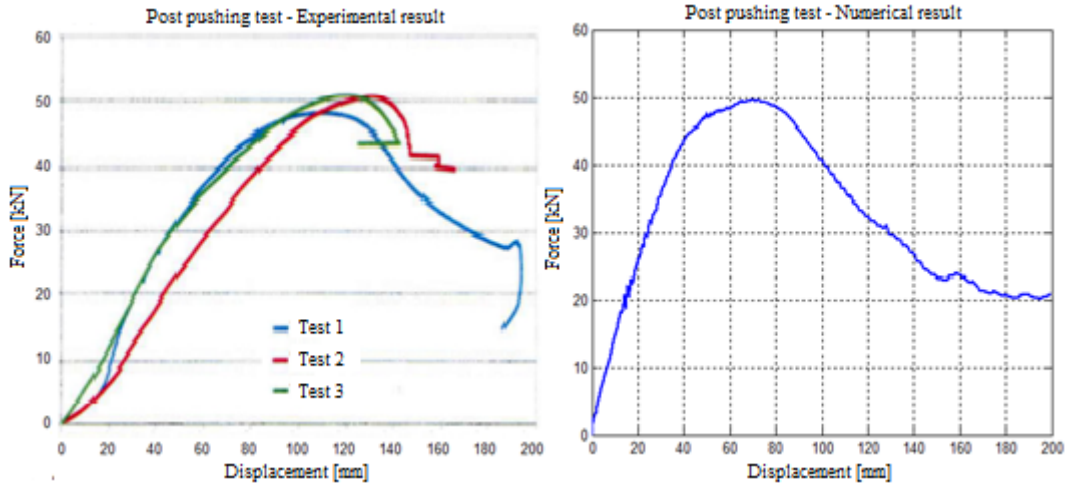

Figura xxii. Confronto numerico-sperimentale della forza imposta sul paletto di barriera in tre casi sperimentali (a sinistra) e in quello numerico (a destra).

Successivamente sono state effettuate le due simulazioni di crash test designate con i codici TB11 e TB81 e i risultati ottenuti sono stati confrontati con quelli relativi alle prove di crash reali precedentemente effettuate.
La procedura di verifica e validazione del modello numerico di barriera, in accordo con quanto imposto dalla normativa EN 1317, consiste innanzitutto in una analisi qualitativa preliminare del corretto comportamento della barriera; ciò significa che la barriera deve essere in grado di reindirizzare il veicolo in svio evitandone il ribaltamento e senza che alcun elemento della barriera penetri l'abitacolo.
In secondo luogo vengono calcolati i principali indici di severità dell'impatto, che devono essere al di sotto dei limiti imposti dalla normativa, e di deformazione della barriera.
Infine si verifica l'attendibilità dell'analisi numerica svolta attraverso una serie di controlli, al fine di assicurasi che essa non sia stata inficiata da alcun problema numerico che ne possa averne compromesso l'affidabilità.

Per quanto riguarda il test TB11 il comportamento qualitativo del modello numerico di barriera risulta accettabile e ben correlato con quello sperimentale.

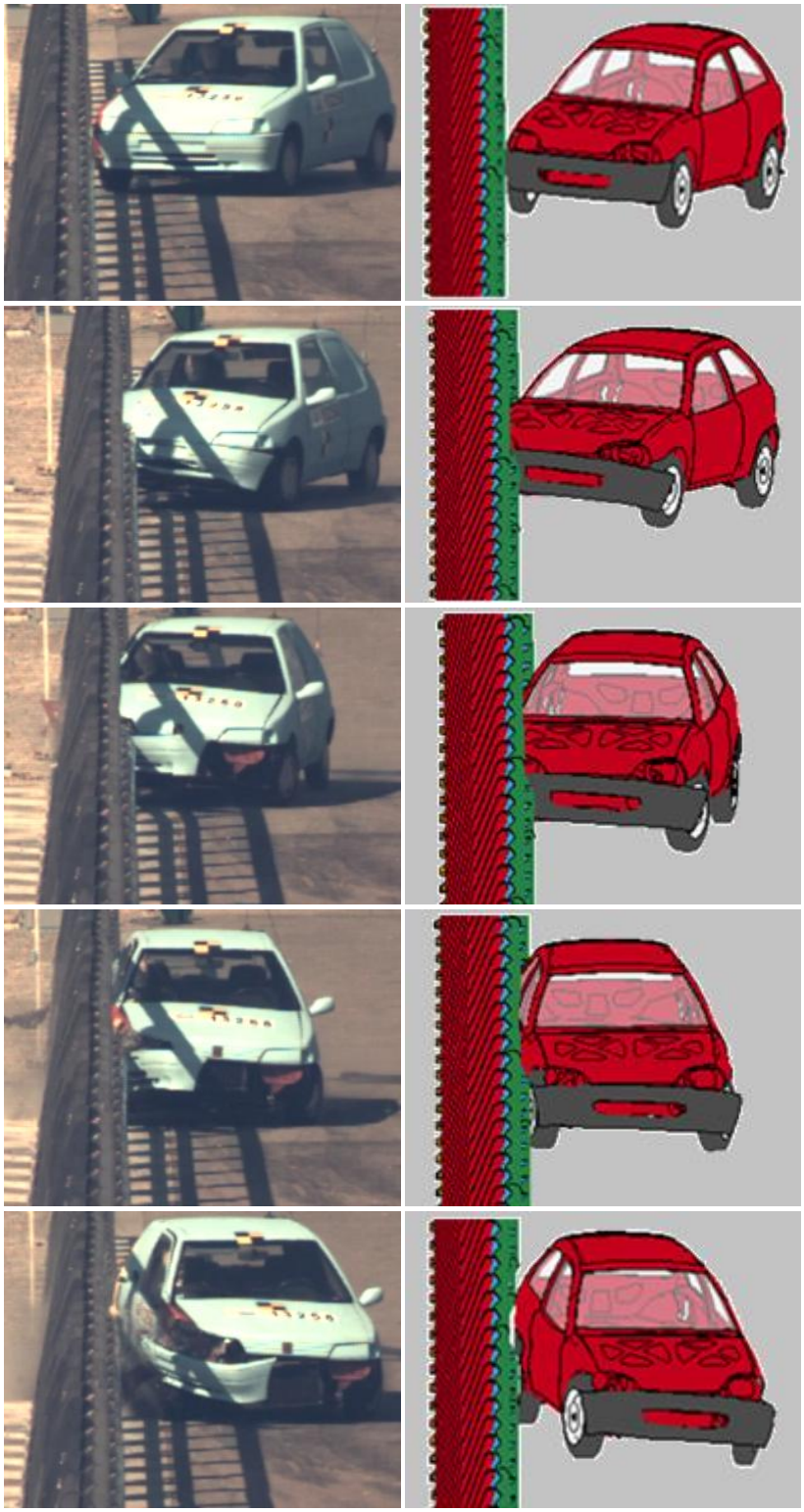

Figura xxiii. Test TB11: confronto numerico-sperimentale della dinamica dell'impatto.

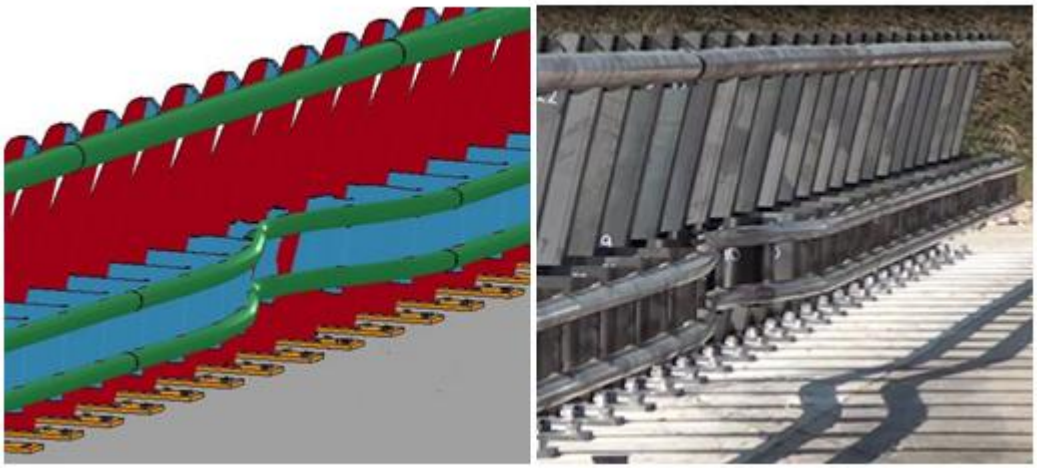

Figura xxiv. Test TB11: confronto numerico-sperimentale della deformata della barriera dopo l'impatto.

Il calcolo degli indici di severità dell'impatto e di deformazione della barriera ha fornito i risultati riportati in Tabella xi.

Tabella xi. Test TB11: indici di severità dell'impatto e deformazione della barriera.

	Crash test reale	Simulazione numerica	Massimo valore ammesso
Working width [m]	-	0.66	-
Vehicle intrusion [m]	-	0.33	-
Dynamic deflection [m]	-	0.35	-
ASI [-]	1.2	1.37	1.4
THIV [km/h]	28	30.7	33
PHD [-]	-	9.8 g	20 g

La Figura xxv mostra i tre indici di deformazione della barriera.

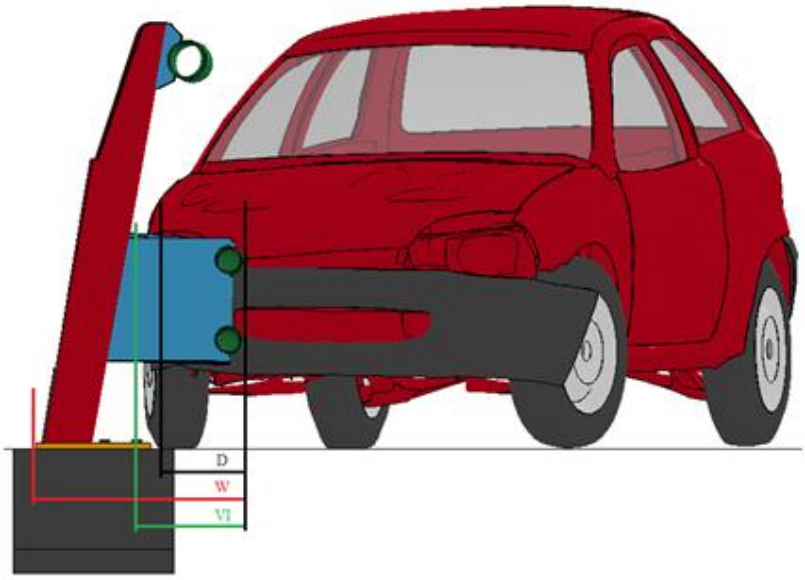

Figura xxv. Test TB11: schematizzazione dei parametri di deformazione della barriera.

L'andamento dell'indice ASI durante l'impatto è riportato nel grafico in Figura xxvi.

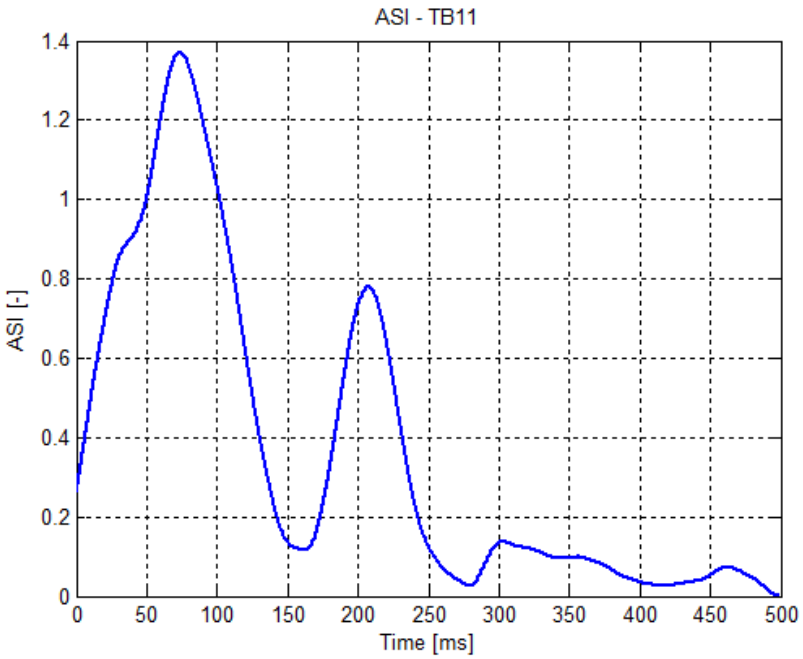

Figura xxvi. Test TB11: andamento dell'indice ASI durante l'impatto.

I risultati dei controlli numerici eseguiti sono riportati in Tabella xii.

Tabella xii. Test TB11: controlli numerici.

Controllo	Risultato	Massimo valore ammesso
Variazione dell'energia totale	0.73%	10%
Energia di hourglass globale rispetto all'energia totale	0.01%	5%
Energia di hourglass globale rispetto all'energia interna globale	0.50%	10%
Energia di hourglass locale rispetto all'energia interna locale	0.06%	10%
Massa aggiunta globale	0.04%	5%
Massa aggiunta locale	6.25%	10%
Energia cinetica aggiunta	0.26%	5%
Nodi shooting	0	0
Volumi negativi	0	0

La stessa procedura è stata seguita per quanto riguarda il test TB81. Il comportamento qualitativo del modello è mostrato nelle Figure xxvii e xxviii; risulta accettabile e correlato con la prova sperimentale.

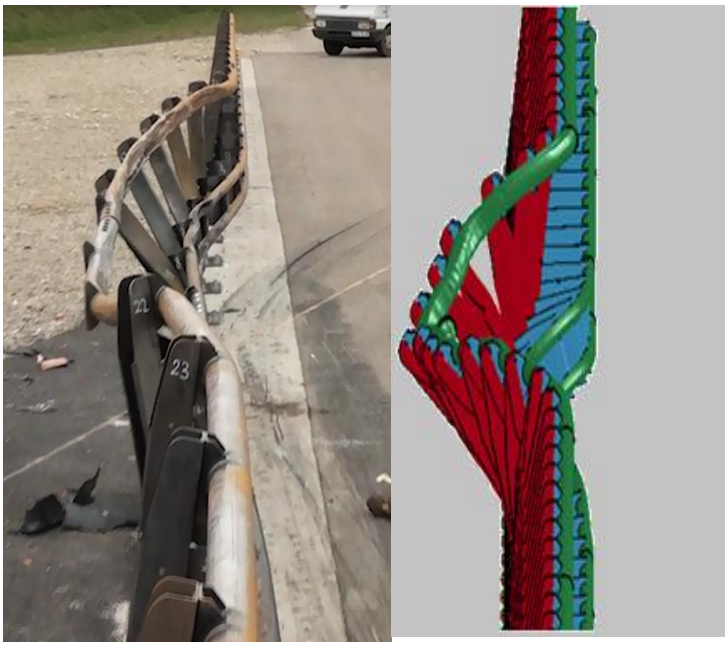

Figura xxvii. Test TB81: confronto numerico-sperimentale della deformata della barriera dopo l'impatto.

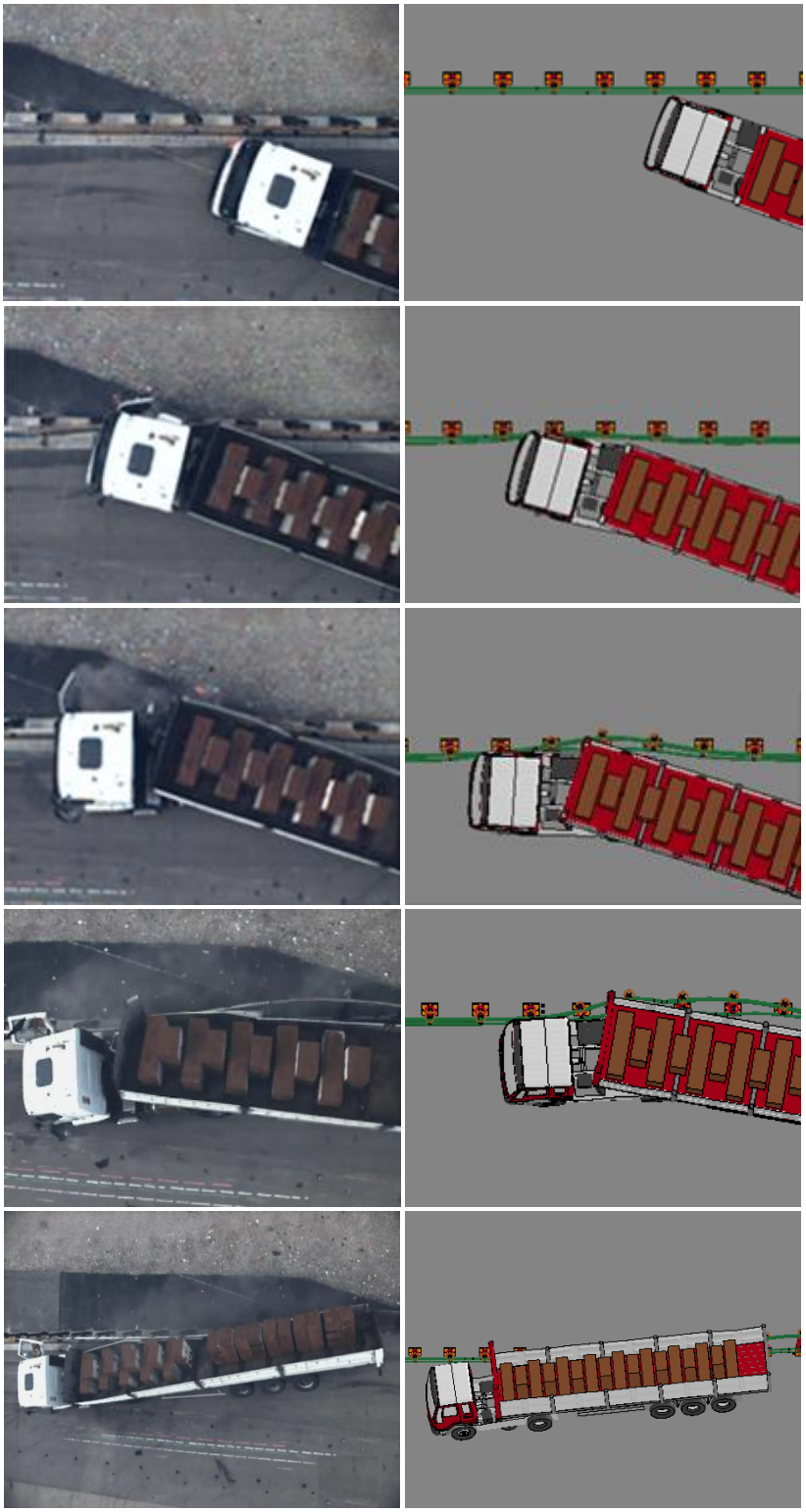

Figura xxviii. Test TB81: confronto numerico-sperimentale della dinamica dell'impatto.

Il calcolo degli indici di severità dell'impatto e di deformazione della barriera ha fornito i risultati riportati in Tabella xiii.

Tabella xiii. Test TB81: indici di severità dell'impatto e deformazione della barriera.

	Crash test reale	Simulazione numerica	Massimo valore ammesso
Working width [m]	1.30	1.10	-
Vehicle intrusion [m]	3.5	2.5	-
Dynamic deflection [m]	-	0.61	-
ASI [-]	-	0.82	1.4
THIV [km/h]	-	20.4	33
PHD [-]	-	12.2 g	20 g

Il parametro VI per veicoli pesanti (Heavy Goods Vehicles – HGV), come l'autoarticolato in questione, viene calcolato considerando un carico ideale avente la larghezza e la lunghezza del pianale del mezzo e un'altezza pari a 4 m. Viene calcolato considerando la posizione e l'inclinazione del pianale e ipotizzando che il carico rimanga indeformato e di forma rettangolare.
La Figura xxix mostra i tre indici di deformazione della barriera.

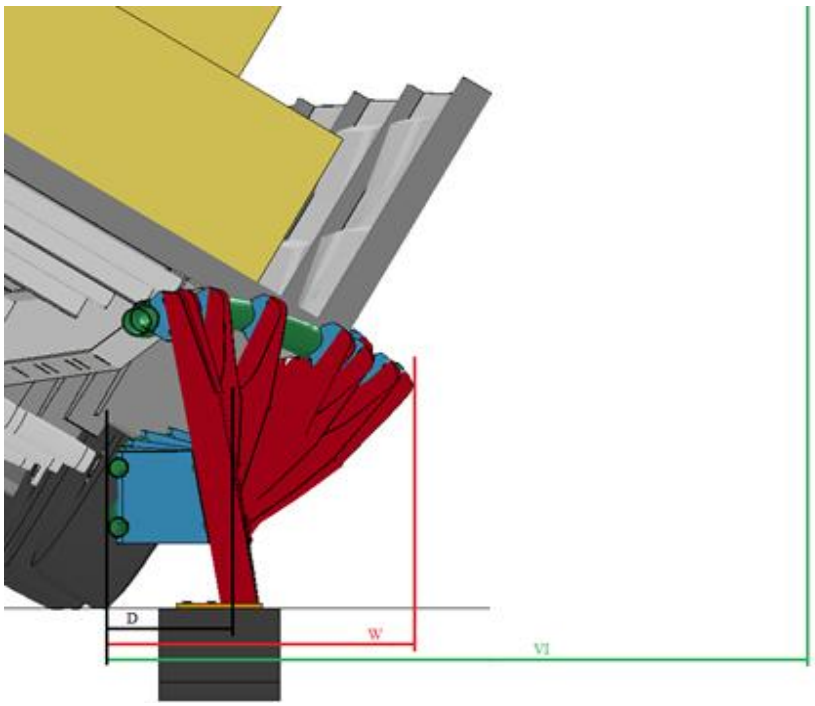

Figura xxix. Test TB81: schematizzazione dei parametri di deformazione della barriera.

L’andamento dell’indice ASI durante l’impatto è riportato nel grafico in Figura xxx.

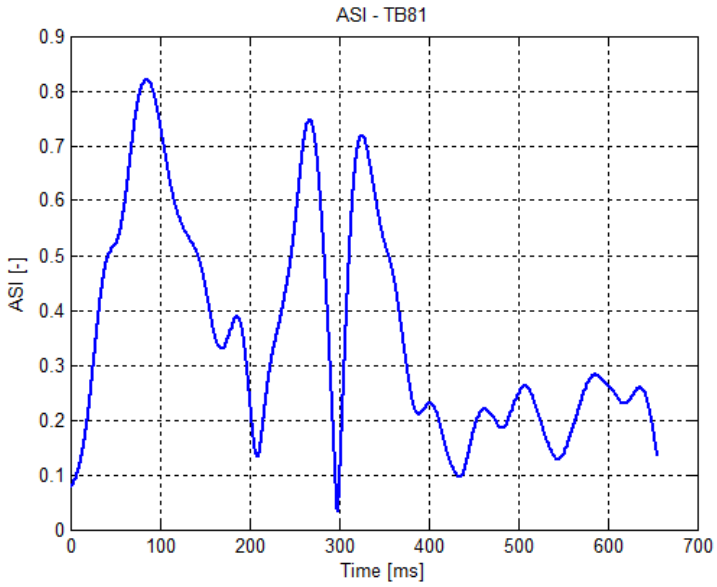

Figura xxx. Test TB81: andamento dell’indice ASI durante l’impatto.

I risultati dei controlli numerici eseguiti sono riportati in Tabella xiv.

Tabella xiv. Test TB81: controlli numerici.

Controllo	Risultato	Massimo valore ammesso
Variazione dell’energia totale	1.85%	10%
Energia di hourglass globale rispetto all’energia totale	0.0006%	5%
Energia di hourglass globale rispetto all’energia interna globale	0.09%	10%
Energia di hourglass locale rispetto all’energia interna locale	4.58%	10%
Massa aggiunta globale	0.03%	5%
Massa aggiunta locale	0.47%	10%
Energia cinetica aggiunta	3.08%	5%
Nodi shooting	0	0
Volumi negativi	0	0

In questo test il veicolo ha avuto un problema di roll-over. Da un confronto con i video relativi al crash test reale è emerso un comportamento del modello piuttosto diverso rispetto a quello dell'autoarticolato reale.
Quindi un possibile sviluppo consisterà in uno studio di miglioramento del modello di veicolo, in modo da ottenere risultati più vicini alla realtà.
La barriera, invece, risulta in grado di reindirizzare correttamente il veicolo e ha mostrato un comportamento simile al caso sperimentale; quindi, in questa analisi preliminare, il modello di barriera può essere considerato accettabile.

Conclusioni e sviluppi futuri

Lo studio svolto in questo lavoro di tesi ha permesso di sviluppare un modello numerico completo di barriera di sicurezza di bordo ponte da poter utilizzare per simulazioni di crash test, affidabile e ben rappresentativo della realtà fisica di queste strutture.
La procedura di caratterizzazione del materiale e di correlazione numerico-sperimentale delle prove ha fornito risultati soddisfacenti.
Il comportamento del modello scelto per rappresentare il vincolo tra barriera e ponte si è rivelato adeguato, sia a livello locale, nei test di tiro di paletti di barriera, che a livello full-scale, nelle simulazioni di crash test svolte alla fine del lavoro.
Il modello realizzato include tutti i componenti presenti in una barriera di bordo ponte, per cui può essere utilizzato per effettuare simulazioni numeriche di crash test su questo tipo di strutture, con la possibilità di analizzare diversi aspetti:

- Sforzi e deformazioni a cui i vari elementi della barriera sono soggetti, per esempio gli sforzi di trazione e taglio agenti sui tirafondo o sui dadi durante un impatto, allo scopo di verificarne il corretto dimensionamento (vedi Figura xxxi);
- Sforzi all'interfaccia fra tirafondo e cordolo di calcestruzzo, al fine di determinare la resistenza minima dell'incollaggio da realizzare;
- Sollecitazioni trasmesse dalla barriera alla struttura del ponte durante un impatto; è possibile infatti definire dei piani, orizzontali o verticali, all'altezza desiderata lungo il cordolo, in corrispondenza dei quali il software può calcolare le forze e i momenti generati, in modo da avere un idea dei carichi ai quali è soggetto il ponte durante l'impatto ed individuare eventuali problematiche.

Una volta ottenute le informazioni desiderate, è possibile procedere ad un eventuale ottimizzazione del progetto, variando opportunamente i parametri presenti nel modello, come le proprietà dei materiale o le caratteristiche

geometriche, al fine di ottenere dei risultati soddisfacenti, per esempio in termini di resistenza dell'incollaggio o di carichi trasmessi al ponte.

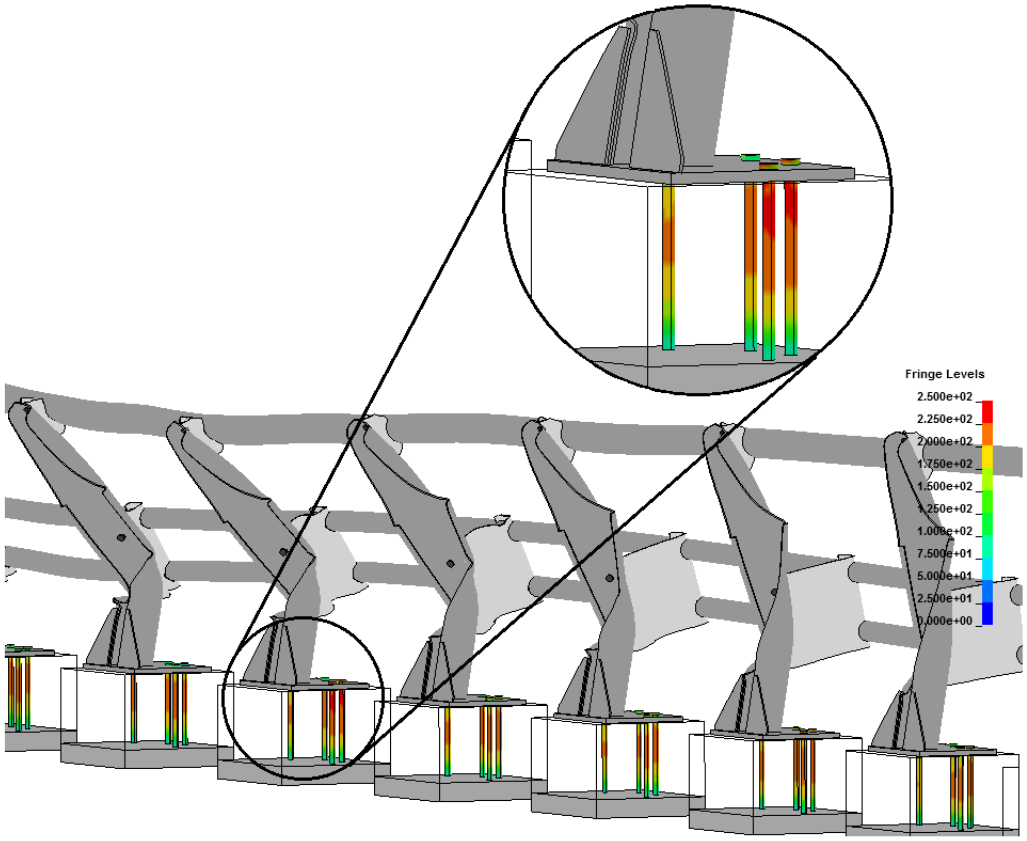

Figura xxxi. Esempio di sforzo di Von Mises agente sui tirafondo durante un impatto.

Il lavoro svolto nell'ultimo capitolo aveva il fine di verificare che il modello di barriera così realizzato mostrasse un comportamento accettabile, ma non prevedeva una procedura di calibrazione numerico-sperimentale.
A questo scopo un primo passo potrebbe essere quello di cercare di migliorare ulteriormente il modello di barriera per ottenere dei risultati, in termini di indici di severità dell'impatto e di deformazione della barriera, più vicini a quelli sperimentali. Vi sono infatti molti parametri su cui è possibile effettuare uno studio di miglioramento, basti pensare che nel modello sono presenti quattro diversi tipi di acciaio e tre tipi di bullonatura, di cui è possibile variare la curva σ-ε o i carichi di rottura.

Per quanto riguarda il calcestruzzo, è stata effettuata una caratterizzazione mediante lo svolgimento di due prove sperimentali di compressione uniassiale, su provini cubici e su provini cilindrici, e la successiva correlazione numerico-sperimentale dei relativi modelli realizzati.

Ulteriori prove verranno realizzate, ossia dei test di compressione ed estensione triassiali, di compressione idrostatica e di deformazione uniassiale; queste saranno utilizzate per migliorare ulteriormente la caratterizzazione del materiale.
Infine, per quanto riguarda la rappresentazione del contatto tra i tirafondo e il calcestruzzo, nel modello realizzato sono stati imposti gli sforzi di cedimento a trazione e taglio che si sono supposti per quel tipo di incollaggio.
Una modellazione più accurata includerebbe una serie di prove di trazione su tirafondo incollati, simili a quelle svolte numericamente e descritte in Appendice A.2, dalle quali si potrebbero determinare gli sforzi di cedimento esatti relativi a quel tipo di incollaggio.
Inoltre, si è detto che questo modello tiene conto della possibilità di cedimento del vincolo tra i tirafondo e il cordolo di calcestruzzo, ma il funzionamento del contatto introdotto consiste solo nel distacco delle due parti in questione nel momento in cui lo sforzo all'interfaccia raggiunge il valore di rottura imposto.
Un ulteriore sviluppo potrebbe essere quello di modellare anche la resina, quindi tenendo conto della sua cedevolezza, per esempio introducendo una nuova parte tra il tirafondo e la parete del foro, a cui si dovrebbero poi assegnare un modulo elastico, un modulo di taglio, una curva σ-ε, una deformazione a rottura, etc.

Contents

List of figures

List of tables

1. Introduction

In this first chapter, the work carried out in this master thesis will be presented. An overview about road safety will be first proposed. Afterwards, a series of examples about accidents involving bridge safety barriers will be described, in order to justify how this work and the research about bridge safety barriers in general can provide an improvement in the field of road safety. At last the main objectives of this study will be explained and the structure of this work will be briefly described.

1.1. Road safety

One of the major tasks in road transportation is to assure an adequate safety level for road users. Road safety includes the protection of vehicle passengers in the event of an accident, trying to avoid or limit damages to those passengers. During the last decade, road accidents have caused in Italy more than 50000 deaths and three millions of injured [1], determining an unacceptable cost concerning first of all the human lives loss, but even regarding economic aspects (temporary or permanent disabilities, reduction of the national healthcare system resources, insurances, destroyed vehicles and infrastructures, etc.).
In order to counteract this situation, the commitment in the road safety improvement has been strongly increased, carrying forward an intensive activity of research and norms development, to regulate the safety road issue and to promote it, regarding both the cultural aspect and the infrastructural one.
Roadside safety addresses an area outside of the roadway and is an important component of the total roadway design. From a safety perspective, the ideal highway has roadsides and median areas that are flat and unobstructed by hazards. Elements such as side slopes, fixed objects and water are potential hazards which a vehicle might encounter when it leaves the roadway. These hazards present varying degree of danger to vehicle and its occupants. Unfortunately, geography and economics do not always allow ideal highway conditions.
Road design in the future will increasingly focus on the safety of all users. Upgrading existing roads to higher safety standards, coupled with greater awareness of the drivers, will lead to significant savings in road trauma and

crash costs. Road maintenance such as resurfacing to improve skid resistance will continue to be a priority.
To achieve the goal of making roads safer designers and road authorities have to consider three key areas:

- Safer people: to encourage safe behavior by ensuring that the drivers adhere to the speed limits, that they do not drive, if impaired by alcohol or fatigue, that all vehicle occupants are using seatbelts and that young drivers have adequate knowledge and supervision.
- Safer vehicles: continuing improvements in vehicle safety with introduction of advanced active and passive safety devices continues to be a priority in automotive industry; current developments in vehicle engineering ensure that all systems within a vehicle are combined to provide optimum safety levels.
- Safer roads: to lower the speed limits, to build and maintain better and safer roads, to improve safety barriers, to build traffic priority systems to ensure quicker responses by emergency services; current improvements in road building legislation ensure that all new roads are built to the most stringent safety standards.

Safety, in the field of road transportation, may be considered from two points of view:

- Active safety: set of measures developed in order to avoid the accident to occurs, or at least to reduce the probability that it does; it includes:

  - ABS (antilock brake system)
  - ESP (electronic stability program)
  - Speed limiters
  - Formation and information campaigns
  - Design criteria for new roads
  - Current roads adjustments
  - Structural interventions regarding pavements, signage, lighting, etc.

- Passive safety: set of measures developed in order to mitigate the damages, principally occurring to people, in the event of an accident; it includes:

  - Safety belts
  - Airbags
  - Obligation to wear a helmet for motorcyclists
  - Measures to enable a timely medical help

- Fire-fighting systems, shelters and auxiliary passages (for long tunnels), etc.
- Restraint systems

In this work much attention has been paid to one of the most important passive safety elements, i.e. the vehicles containment systems, particularly the road safety barriers installed on concrete bridges.
The norm EN 1317 classifies road safety barriers according to the correspondent level of containment, which is the kinetic energy related to the component of the vehicle velocity perpendicular to the carriageway that the barrier is able to absorb during an impact [2].

Table 1.1. Levels of containment of road safety barriers.

Barrier class	L_c [kJ]
T1	6
T2	21
T3	37
N1	44
N2	82
H1	127
H2	288
H3	463
H4a	572
H4b	724
L1	127
L2	288
L3	463
L4a	572
L4b	724

The levels of containment are verified by means of crash tests; the norm defines the type of vehicle, the velocity and the angle of impact.

1.2. Accidents involving bridge safety barriers

Infrastructures like bridges, overpasses, viaducts, on which the vehicles are exposed to the vacuum, are characterized by a very high risk of severe damages in case of accidents, definitely higher than what concerns the common acceptation of road safety.

While usually the wrong behavior of a road safety barrier, in the case of an accident, does not necessarily result in lethal injuries, this is much more likely when the concerned barrier is installed on a bridge.
Bridge safety barriers play a crucial role in the field of the road traffic safety, and if a wrong behavior of the normal barriers is not admitted, this is even more strict as far as bridge barriers are concerned.
These are the reasons why the regulations suggest that the barriers designed to be installed on bridges should belong to the higher containment classes.
The history of road accidents provides many examples of the disastrous consequences caused by the malfunctioning of a bridge safety barrier.
Usually, those examples regard heavy vehicles, such as articulated trucks or buses, because the barriers commonly installed on bridges are characterized by a high level of containment (minimum H2), so they are supposed to restrain at least the cars. They actually should be designed in order to restrain also the heavy vehicles, but they often do not absolve this duty correctly.
There are several cases occurred in Italy, which prove the fact that not always the barriers work as they are supposed to do.
On October 13th 2013 a truck which was travelling along the beltway of Siena dropped from an overpass, crashing on the road below [3].

Figure 1.1. Example of accident involving bridge safety barriers (Siena, October 13th 2013) [3].

This is a clear evidence of the safety barrier bad behavior, which has not been able to prevent the truck drop.

The reasons why it did not work correctly are difficult to explain. The concrete curb on which the barrier is placed did not fail; this means that the problem has been the inadequacy of the safety barrier chosen for that stretch of road.
This barrier is clearly not appropriate to restrain heavy errant vehicles, such as an articulated truck, like the one in the picture.
The road along which it has been installed is a beltway, hence a main suburban road characterized by an intense traffic, even with heavy vehicles that travel fast. It should have been tested by means of a crash test TB81, which is the only one performed using an articulated truck.
Other recent Italian similar cases, in which the safety barriers turned out to be not suitable to restrain heavy vehicles, are the following:

- Cesena (FC), February 14th 2014.
- Cuneo, July 22nd 2013.
- Sarezzo (BS), June 18th 2013.
- Caltanissetta, April 24th 2013.
- Cefalù (PA), August 30th 2012.
- Corato (BA), April 28th 2008.

As visible in Figure 1.2, the safety barriers used on those bridges were definitely not adequate to restrain vehicles like articulated trucks.

Figure 1.2. Example of accident involving bridge safety barriers (Caltanissetta, April 24th 2013).

In the following case, instead, the barrier was not even able to restrain a lightweight vehicle, like the van that dropped from a viaduct nearby Florence on July 16th 2013, ending on tie rods, shown in Figure 1.3. This barrier turned out to be absolutely not suitable to be installed on any infrastructure like this one [4].

Figure 1.3. Example of accident involving bridge safety barriers (Florence, July 13th 2013) [4].

Lastly, one of the most tragic road accidents occurred on July 28th 2013 on the motorway which connects Naples to Canosa (BA), when a bus dropped from a viaduct, causing 38 dead and 11 injured.
The causes of this accident have been identified in a mechanical failure of the brakes and in the malfunctioning of the safety barrier installed along the side of the viaduct, shown after the accident in Figure 1.4.

Figure 1.4. Example of accident involving bridge safety barriers (Avellino, July 28th 2013) [5].

As far as concerns the barrier, it is a New Jersey, made of concrete; it belongs to the containment class H4, according to the regulations, which suggest to install this type of barriers on highway bridges.
This barrier was hence supposed to absorb an impact until 572 kJ and restrain a 38 tons articulated truck travelling at the speed of 65 km/h, thus almost 3 times heavier than a bus. Moreover, the fact that the bus dropped from the viaduct almost vertically prove that its velocity was quite low, since the driver tried to slow it down by crawling against the walls of a tunnel.

The main reason why the barrier has been so easily broken through may be identified in the poor maintenance of the barrier itself.
This barrier was in fact still utilized after it has been probably subjected to many impacts, perhaps characterized by a low energy, caused by cars; the succession, over the years, of these impacts brought eventually the barrier to the failure, since its residual strength has been certainly much reduced [5].

1.3. Objectives of the work

The improvement of vehicles containment systems is one of the most important tasks in the road safety framework and numerical simulations represent an excellent instrument for the analysis of crash phenomena: in this way it is possible to improve barriers design, in order to reach better performances, strongly reducing testing costs and time.
The peculiar geometry of a bridge safety barrier, in particular of the anchoring system, cannot be well represented by the models commonly used for crash test simulations.
Hence, the main purpose of this work is to provide a contribution in the field of road safety through the development of a bridge safety barrier numerical model for crash test simulations, capable of correctly representing the physical behavior of this type of structures, taking into account all the failure modes which may occur during an impact.
This has been achieved in four main steps:

- A research has been firstly carried on in order to find out the best way to represent the link between the barrier and the bridge.
- Afterwards the material characterization has been fulfilled, through a series of compression tests performed on standard concrete specimens, followed by the development and the calibration of the correspondent numerical models.
- The behavior of the modeling solution chosen in the first step and of the material has been then verified through a numerical-experimental comparison of several full-scale tests.
- At last, the model behavior has been certified by means of two full-scale crash test simulations, performed on a commercial bridge safety barrier, according to the European standard EN 1317.

1.4. Thesis organization

A brief description of each chapter is reported below:

Chapter 1: introduction to road safety and objectives of the work.

Chapter 2: description of the anchoring methods commonly used to connect safety barriers to concrete bridges; modeling of the link between the barrier and the bridge considering all the failure possibilities.

Chapter 3: overview on concrete characteristics and mechanical properties; brief description of the concrete numerical model chosen.

Chapter 4: description of the experimental tests performed on concrete specimens and the numerical-experimental correlation procedure.

Chapter 5: description of the push tests performed on two posts and of a traction test performed on two anchor bolts; explanation of the correspondent numerical models developed and the numerical-experimental correlation procedure carried out.

Chapter 6: overview on road safety barriers, particularly focused on bridge safety barriers, and explanation the characteristic parameters of a crash test; description of the barrier model developed and the full-scale crash tests performed; comparison between the experimental results and the numerical ones.

2. Anchoring system

While common road safety barriers are constrained by embedding the posts into the soil, barriers designed for bridges are placed on a drilled concrete curb and constrained by means of a certain number of metallic anchor bolts, which are linked to the surrounding concrete.
In this chapter, an overview of the techniques utilized to install a safety barrier on a bridge and link the anchor bolts to the concrete will be presented.
Afterwards, a possible way to model numerically the anchoring system, considering all its possible behaviors and failures, will be described.

2.1. Anchoring systems general features

2.1.1. Anchoring methods and installation techniques

During the last five decades the development of post-installed anchoring systems has considerably increased in the field of the concrete structures, mostly thanks to the improvement of the prefabrication and perforation techniques; this led to the necessity of define criteria and norms to regulate the production of these systems.
The first response came in 1973 from the German Institute for the Construction Techniques, which defined the first criteria for employment and testing of systems used for the anchoring into the concrete. The current reference standards for the anchoring methods are reported in [6].
It is possible to assert that for many structures this norm is regularly applied by designers, but bridge safety barriers, both New Jersey and guard rail, are an exception. In this sector, the overview of anchor products and design procedures is not yet exactly defined.
Currently there are three ways to place metal anchors into drilled concrete slabs:

- Anchoring by expansion
- Undercutting
- Bonding

Expansion anchors are constrained in drilled holes by means of a forced expansion. A tensile force applied to the anchor is transferred to the concrete by

the friction which originates between an expanded sleeve and the concrete. Two types of expansion anchors are covered:

- Torque-controlled
- Deformation-controlled

With torque-controlled anchors, the expansion is achieved by a torque acting on the screw or bolt; the intensity of the anchorage is controlled by this torque.
With deformation-controlled anchors, the expansion is generally achieved by impacts acting on a sleeve or a cone.

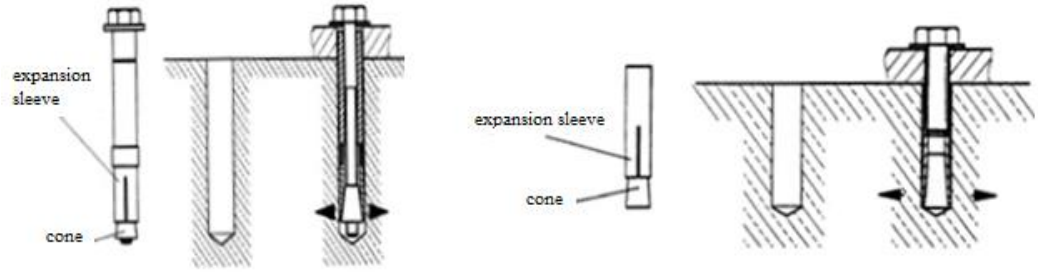

Figure 2.1. Example of torque-controlled (on the left) and deformation-controlled (on the right) expansion anchors [6].

Undercut anchors are constrained mainly by mechanical interlock provided by an undercut in the concrete.

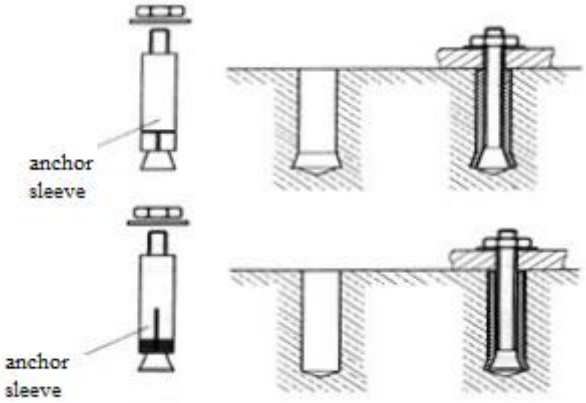

Figure 2.2. Example of undercut anchors [6].

Lastly, bonded anchors are constrained in drilled holes by bonding the metal parts to the sides of the drilled hole with a mortar (e.g. resin mortar). Tensile

loads are transmitted to the concrete via bond stresses between the metal parts and the mortar and between the mortar and the concrete face of the drilled hole.

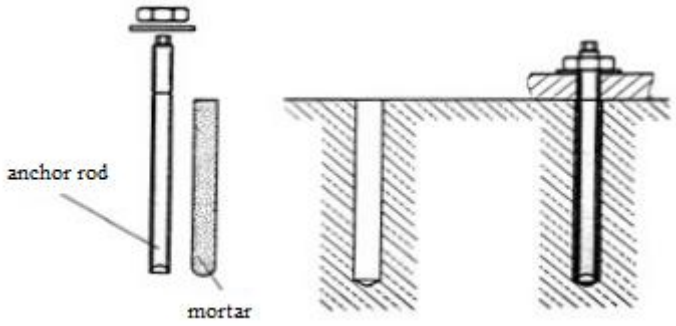

Figure 2.3. Example of bonded anchors [6].

More than 90% of the bridge safety barriers anchoring systems is currently realized by means of bonded anchors.
The bolt dimensions mostly used are M12, M16, M20, M24, generally belonging to the class 8.8, according to the barrier category considered. The holes depth is usually comprised between 150 and 350 mm.
The embedded part of the anchor may be threaded rod, deformed reinforcing bar, internally threaded socket or other shapes.
The bonding materials may be manufactured from synthetic mortar, cementitious mortar or a mixture of the two including fillers and/or additives. The most employed products for bonded anchors are mixtures of two-component castable synthetic resin, mostly made of epoxy polyester.

There are three possible installation techniques of bonded anchors. In the first case, a capsule is placed in the hole and the embedded part is driven by a machine with simultaneous hammering and turning.

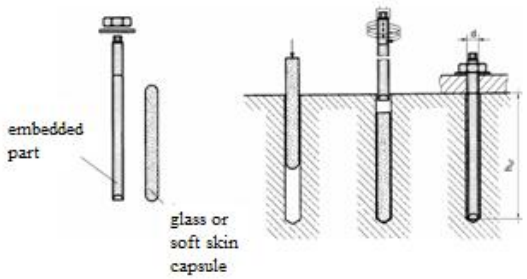

Figure 2.4. Example of installation technique of bonded anchors (capsule type) [7].

With the second technique, the bonding material is injected into the hole. Embedded part may be inserted manually or mechanically.

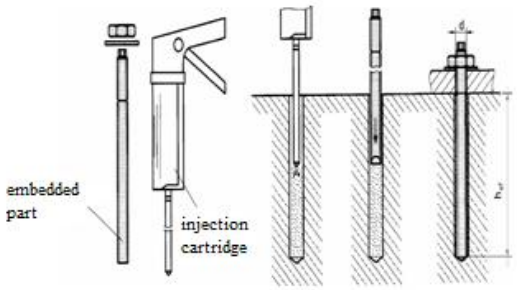

Figure 2.5. Example of installation technique of bonded anchors (injection type) [7].

Eventually, the third technique consists of pouring the bonding material into the hole; afterwards the embedded part is inserted.

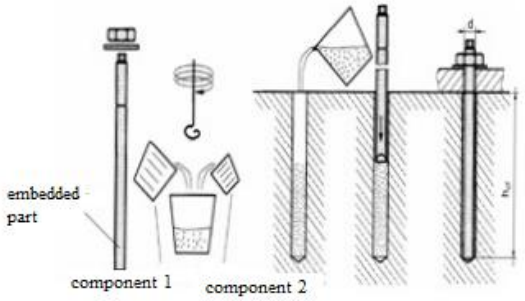

Figure 2.6. Example of installation technique of bonded anchors (bulk type) [7].

2.1.2. Anchoring systems verification criteria

The standard [8] defines the methods utilized to estimate the anchoring systems resistance, in order to verify that a barrier fulfills the requirements imposed by the norms to designers.
These methods share a “limit states” approach, which consists of the comparison between the calculated value of the loads and the design resistance; those parameters are usually defined according to the theory of partial safety coefficients, which may be used either to multiply the value of the loads or to divide the value of the resistance.
This verification is repeated considering different possible rupture scenarios, that may be characterized by shear ruptures, traction ruptures or a combination

of these two conditions, and that can involve the steel, the concrete or the interface between these two materials.
The criterion described in [8] schematizes the functioning mechanism of an anchoring system through a simplified configuration, which considers the single anchor as "specialized" to withstand a certain load: the front anchors (the ones facing the carriageway) are supposed to withstand only traction loads, while the rear anchors are considered solicited only by shear loads.
According to this model, the possible failure modes (assuming that the installation of the anchors is totally made in compliance with the prescribed requirements) are the concrete conical rupture due to traction and the failure of the concrete edge due to shear.
The model expresses the anchor system resistance with respect to those two failure modalities, introducing the parameters $N_{Rk,c}$ and $V_{Rk,c}$. These values are considered as proportional to the resistances of one single anchor embedded in a concrete slab, named $N^0_{Rk,c}$ and $V^0_{Rk,c}$, through the following equations [9]:

$$N_{Rk,c} = N^0_{Rk,c} \cdot \frac{A_{c,N}}{A^0_{c,N}} \cdot \prod_i \psi_{i,N} \tag{2.1}$$

$$V_{Rk,c} = V^0_{Rk,c} \cdot \frac{A_{c,V}}{A^0_{c,V}} \cdot \prod_i \psi_{i,V} \tag{2.2}$$

where

- $A_{c,N}$ is the base area of the concrete cone defined for the designed anchoring system.
- $A^0_{c,N}$ is the base area of the concrete cone defined for an analogous isolated anchor.
- $A_{c,V}$ is the area on the lateral edge of the concrete slab, corresponding to the concrete cone height and width, defined for the designed anchoring system.
- $A^0_{c,V}$ is the area on the lateral edge of the concrete slab, corresponding to the concrete cone height and width, defined for an analogous isolated anchor.
- Ψ_i are corrective factors, which take in account several aspects that may influence the anchoring system performances, such as the concrete cracking state, the presence of steel reinforcements, the slab thickness, etc.

The above mentioned areas are calculated by means of empirical formulas.
$A^0_{c,N}$ is calculated as the area of a square surface whose side size depend on the bolt length. According to the previous experience, the concrete cone can be approximated as a pyramid with square base, whose height is equal to the bolt length and whose base side is three times the height.
Hence, if h is the embedded length of the bolt,

$$A^0_{c,N} = s^2 = (3 \cdot h)^2 \tag{2.3}$$

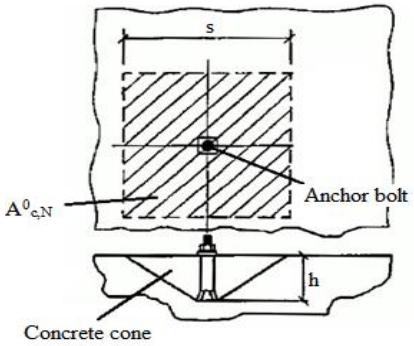

Figure 2.7. Schematic representation of the concrete breaking cone with one anchor bolt [8].

$A_{c,N}$ depends on the anchor bolts number, length and position and it is calculated by means of formulas which take in account these parameters. As an example, the formula usable to calculate the area $A_{c,N}$ concerning an anchoring system constituted by four bolts is the following (all the other cases are reported in details in [8]):

$$A_{c,N} = (C_1 + S_1 + 0.5 \cdot s) \cdot (C_2 + S_2 + 0.5 \cdot s) \tag{2.4}$$

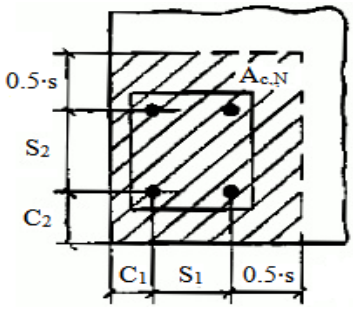

Figure 2.8. Schematic representation of the base area of the concrete breaking cone with four anchor bolts [8].

where s is the same used in the calculus of $A^0_{c,N}$.
As far as concerns the shear, the area $A^0_{c,V}$ is calculated as follows:

$$A^0_{c,V} = (2 \cdot 1.5 \cdot C_1) \cdot 1.5 \cdot C_1 \quad (2.5)$$

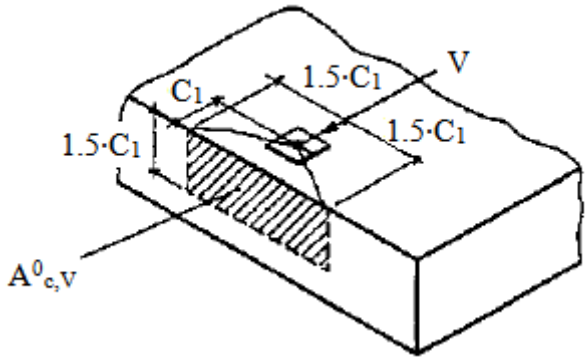

Figure 2.9. Schematic representation of the area on the lateral edge of the concrete slab corresponding to the concrete cone height and width, for one anchor bolt [8].

The area $A_{c,V}$, considering as example again an anchoring system made by four bolts, is:

$$A_{c,V} = (1.5 \cdot C_1 + C_2 + S_2) \cdot h_c \quad (2.6)$$

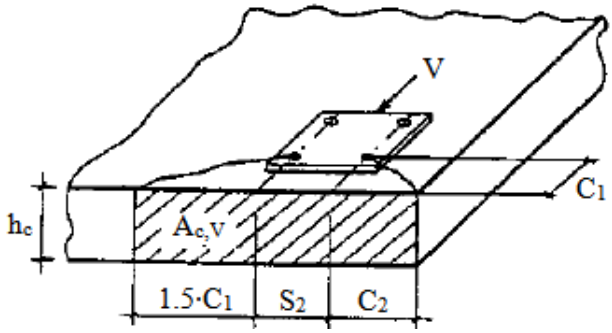

Figure 2.10. Schematic representation of the area on the lateral edge of the concrete slab corresponding to the concrete cone height and width, for a system of four anchor bolts [8].

where h_c is the concrete slab height.
The main approximation of this method is that it has been developed considering static loads, while the anchoring systems are typically subjected to dynamic impulsive loads.

According to this method, the critical issues are mostly related to the concrete characteristic strength, which influences the values of $N^0_{Rk,c}$ and $V^0_{Rk,c}$; for instance, the value of $N^0_{Rk,c}$ depends on the concrete characteristic strength R_{ck} and the bolt length h according to the following equation [8]:

$$N^0_{Rk,c} = 7.2 \cdot \sqrt{R_{ck}} \cdot h^{1.5} \tag{2.7}$$

Another parameter that strongly influence the anchoring system resistance is the concrete slab width, and the distance at which the bolts are placed from the slab edge.
This method assumes that the above defined areas are limited by the slab edges, which results in a decreased resistance with respect to the ideal case of indefinite surface; this condition is instead well represented by the crash tests, because of the large width of the slabs commonly used, which is usually not less than 70 cm.
This aspect is shown by the graphic in Figure 2.11, in which the resistance of an anchor bolt subjected to a traction load is plotted as a function of the distance d at which it is placed from concrete slab edge; each curve refers to a certain value of the concrete strength R_{ck}.

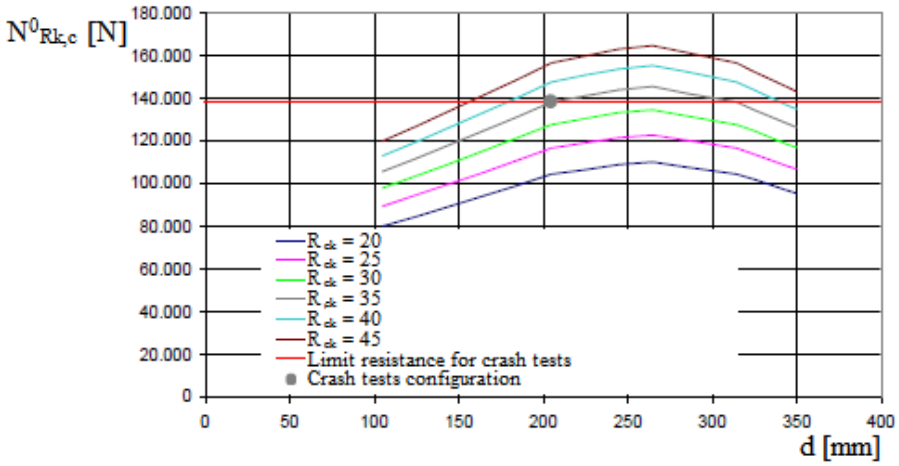

Figure 2.11. Resistance of an anchor bolt subjected to a traction load as a function of its distance from the concrete slab edge and the concrete strength [9].

Firstly, it can be noted the strong influence that both the parameters R_{ck} and d have on the anchor bolt resistance; plus, all the curves show that exists an

optimum point, where to place the anchor bolt in order to maximize its resistance.
The graphic regarding the shear shows a different behavior: the influence of the concrete strength is less relevant and the anchor bolt resistance increases exponentially with the distance from the concrete slab edge.

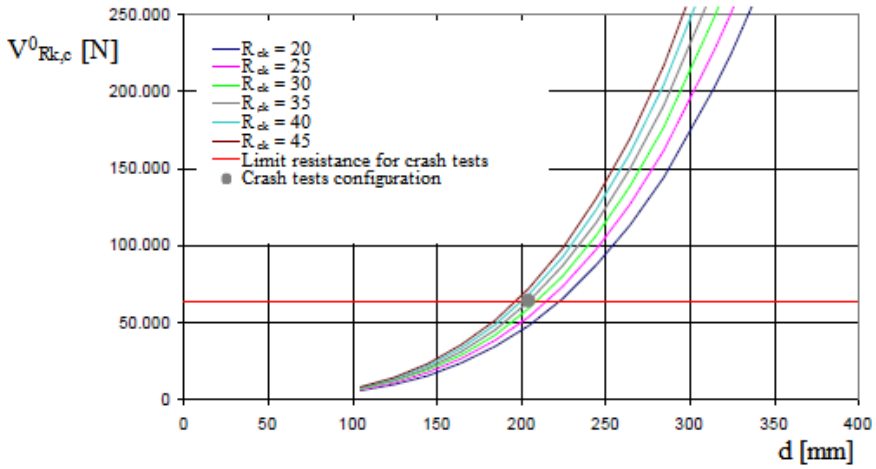

Figure 2.12. Resistance of an anchor bolt subjected to a shear load as a function of its distance from the concrete slab edge and the concrete strength [9].

Hence, the design of an anchoring system always heads toward a compromise solution, since the placement of the bolts as far as possible from the concrete slab edge improves the performances as far as concerns the shear, but may cause an estrangement from the optimal condition regarding the traction resistance.
Possible interventions which can improve the anchoring system performances are:

- Optimization of the anchors position with respect to the concrete slab edge
- Increase of the bolts number
- Increase of the bolts size
- Increase of the concrete characteristic strength

2.2. Modeling of the anchoring system

The model here developed takes into account all the possible failure modalities which concern bridge safety barriers; hence, the failure of all the metallic

elements, the bolting, the concrete and the link between the anchor bolts and the curb.
The numerical models mostly used for crash test simulations are well representative for common road safety barriers, whose posts are embedded into the soil for a certain length. In these cases the model is realized by means of one of the techniques here shortly described (further details are provided in Appendix A.1) [10]:

- Displacements and rotations of the part of the posts embedded into the soil are constrained; in order to consider somehow the soil deformability, not the entire embedded length may be constrained.
- Soil deformability can be represented by a set of non-linear spring elements, whose stiffness may be a function of depth, soil characteristics, crushing or post geometry; they are linked to the embedded part of the posts.
- The soil can be represented as a common structural element of the model, by creating volumes, usually cylindrical, which surround the embedded part of each post, meshing them by means of solid elements and opportunely defining the material properties.

Clearly none of these models can well represent a bridge safety barrier, whose anchoring system is totally different; this system is indeed composed by an horizontal plate on which the post is welded (thus, there is not any embedded part of the post), and several anchor bolts, whose number may vary from three to six.
There are some simplified methods to represent such a structure (described in Appendix A.1), but the model realized in this work is able to correctly represent all the elements which it is composed by, the interactions among them and the possible failure of each of them.
As previously explained, the most common types of anchoring methods are the bonded anchors. In order to represent the actual behavior of the bonding, a contact which took in consideration the resin failure possibility was needed.
When the anchor bolts are pulled out of the concrete, a shear stress and a tensile stress originate respectively on the lateral and on the bottom surface of the bolts. If neither the bolts nor the concrete break before the resin failure, the whole bolt is pulled out of the concrete when the maximum admissible stress of the resin is reached.

In order to represent this behavior, the LS-Dyna® feature *CONTACT_TIED_SURFACE_TO_SURFACE_FAILURE has been chosen, because it has the option of introducing two parameters which represent respectively the tensile and the shear stresses at failure, that are exactly the variables needed to represent a bonded link, and which are usually provided from the industrial bonding resins supply companies.
The only requirement that this kind of contact needs is to have two surfaces with coincident nodes. Those nodes are considered tied until the local value of the stress reaches the admissible limit. If it happens, the concerned nodes are released from each other. When two nodes are released, the stress on the nodes which are still tied increases, until all of them are released and the two surfaces detach from each other.
This is the reason why a beam element was not suitable to use with this type of contact.
Hence, a special attention should be paid when the concrete slab and the shank of the bolts are meshed; as discussed above, the mesh size on the external cylindrical surface of the shank must be exactly the same used for the surface of the holes, in order to have coincident nodes on the two surfaces.
Functional tests have been carried on using simple models in order to check the effectiveness of this feature; the results are shown in Figures 2.13 and 2.14. It can be noted that when the stress on the contact surfaces reaches the settled value the two parts are detached from each other. Details about how these tests have been carried out are provided in Appendix A.2.

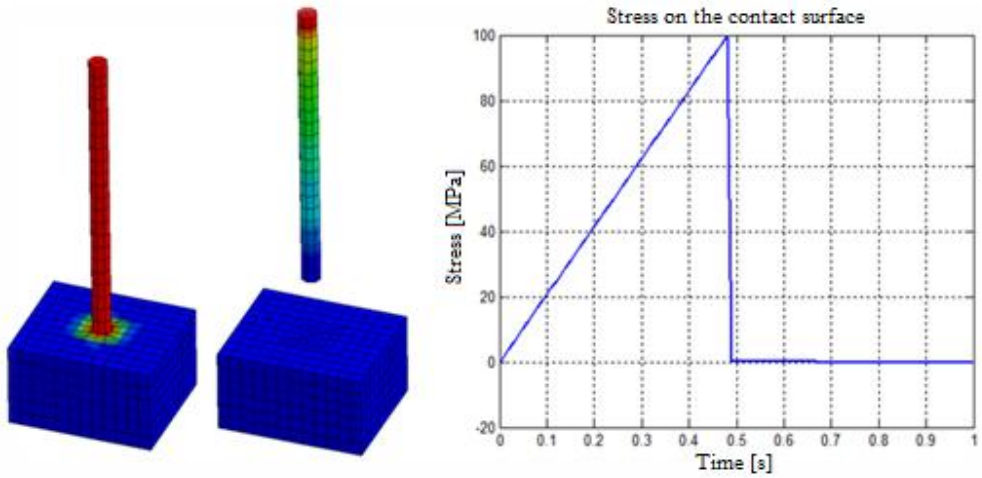

Figure 2.13. First functional test of the contact. The graphic shows the trend of the stress on the contact surface.

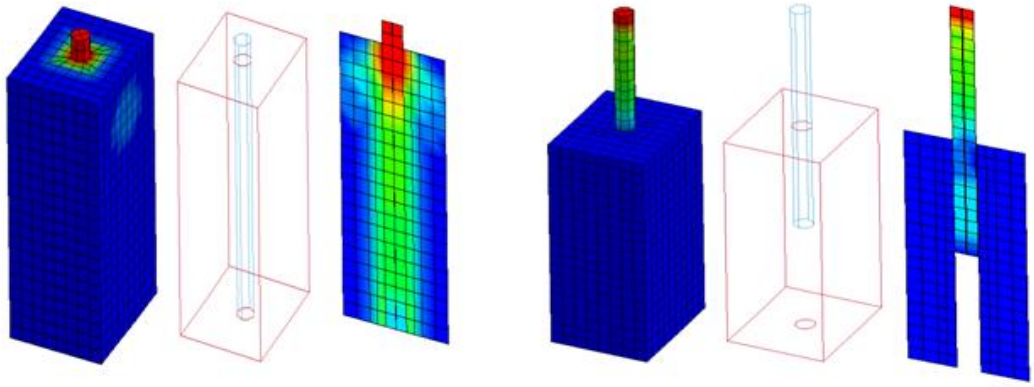

Figure 2.14. Second functional test of the contact. The stress is transmitted between the two parts until the detachment.

Anchor bolts preloading

Numerical models like the one here developed require the introduction of a steady preloaded state before performing the normal transient dynamic analysis (see Appendix A.3); in this case, this is due to the torque applied to the anchor bolts.
The anchor bolts, which are modeled through solid elements, have been preloaded by means of a thermal contraction; the idea is to shrink the bolt by cooling it: as bolt contracts, the preload is induced.
The temperature variation ΔT (or the coefficient of thermal expansion α) to produce a target stress σ can be estimated as follows

$$\sigma = E \cdot \alpha \cdot \Delta T \tag{2.8}$$

where

E = Young's modulus
α = Coefficient of thermal expansion
ΔT = Temperature variation

In Figure 2.15 are shown the anchor bolts at their initial condition. Neither forces nor displacements have been applied yet, but the anchor bolts are already loaded by a settled stress. The stress to impose depends on the bolts size, the thread characteristics and the torque applied; its calculation will be explained in Paragraph 5.2.

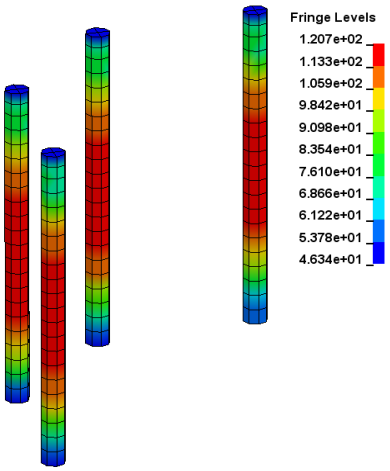

Figure 2.15. Von Mises stress acting on the anchor bolts due to the torque applied.

Since the temperature reduction causes a contraction of the anchor bolts shanks, a stress concentration, due to the contact with the nuts, originates around the holes on the plate; it can be seen in Figure 2.16.
Figure 2.16 shows also the stress distribution on the holes surfaces in the concrete slab.

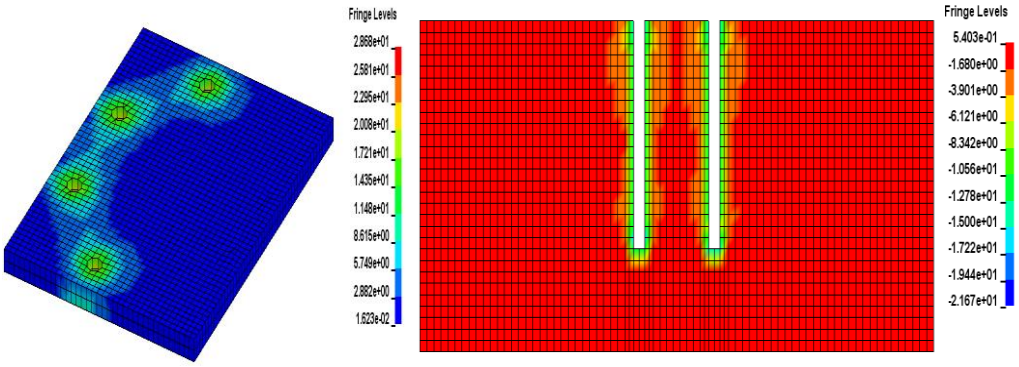

Figure 2.16. Von Mises stress acting on the plate and third principal stress acting on the concrete slab due to the bolts contraction.

3. The concrete

In this chapter, an overview of the concrete general features, such as composition, production technique, properties, mechanical characteristics and possible ways to classify it, will be presented.
In the second part of the chapter, the constitutive model used to represent concrete behavior will be described.

3.1. Concrete general features

3.1.1. Composition

Since it is constituted by several different components, concrete can be considered as a composite material.
It is principally composed by a coarse granular material (the aggregates) embedded in a hard matrix (the cement) that fills the space among the particles and glues them together.
There are many types of concrete available, created by varying the proportions and the characteristics of the ingredients. In this way the finished product can be tailored to its application, varying the strength, the density, or the chemical and thermal resistance properties.
Concrete is made by the following components:

- Aggregates: large chunks of material, generally a coarse gravel or crushed rocks such as limestone or granite, along with finer materials such as sand.
- Cement: commonly Portland cement and other cementitious materials such as fly ash and slag cement, which serve as binder for the aggregates.
- Water: mixed with the other components produces a semi-liquid that workers can shape (typically by pouring it into a form). The concrete solidifies and hardens through a chemical process called hydration. The water reacts with the cement, which bonds the other components together, creating a robust stone-like material.
- Chemical admixtures: added in order to achieve varied properties. These ingredients may speed or slow down the rate at which the concrete hardens, and impart many other useful properties.
- Reinforcements: concrete is strong in compression, as the aggregates efficiently carries the compression loads, and weak in tension, as the cement holding the aggregates in place can crack, allowing the structure to

fail; reinforced concrete adds steel reinforcing bars, steel fibers, glass fiber, or plastic fiber to carry tensile loads.

- Mineral admixtures: they are becoming more popular in recent decades. The use of recycled materials as concrete ingredients has been gaining popularity because of the increasingly stringent environmental legislation, and the discovery that such materials often have complimentary and valuable properties. The most conspicuous of these elements are fly ash, a byproduct of coal-fired power plants, and silica fume, a byproduct of industrial electric arc furnaces. The use of these materials in concrete reduces the amount of resources required, as ash and fume act as a cement replacement. This avoids the cement production, an energetically expensive and environmentally problematic process, while reducing the amount of industrial waste that must be disposed of.

The average composition of 1 m^3 of concrete is shown in Figure 3.1.

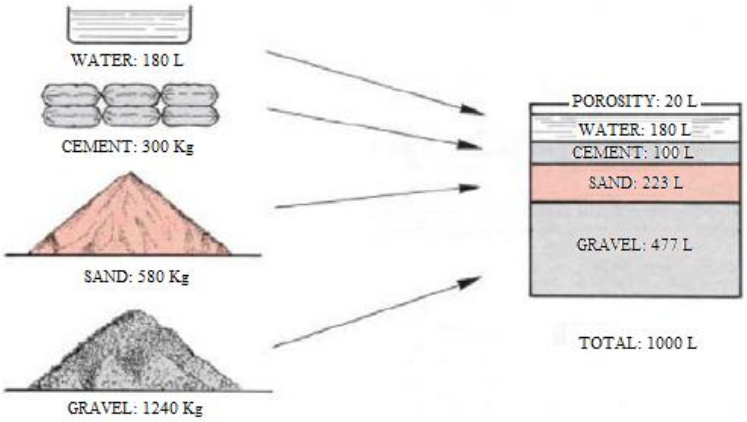

Figure 3.1. Average composition of 1 m^3 of concrete.

Depending on its density, the concrete can be classified in three categories:

- Light concrete ($\rho < 1800$ Kg/m^3)
- Normal concrete ($\rho \approx 2400$ Kg/m^3)
- Heavy concrete ($\rho > 3200$ Kg/m^3)

Cement and water

A lower water/cement ratio yields a stronger, more durable concrete, while more water gives a freer-flowing concrete with an higher slump (see Appendix B.2).

Impure water used to make concrete can cause problems such as the premature failure of the structure.
Hydration involves many different reactions, often occurring at the same time. As the reactions proceed, the products of the cement hydration process gradually bond together the individual sand and gravel particles and the other components of the concrete to form a solid mass.

Aggregates

Fine and coarse aggregates make up the bulk of a concrete mixture. Sand, natural gravel and crushed stone are used mainly for this purpose.
The presence of aggregates greatly increases the durability of concrete above that of cement, which is a brittle material in its pure state. Thus concrete is a true composite material.
An inhomogeneous distribution of aggregates can lead to strength gradients.
In order to minimize the volume of the blanks in the mixture, aggregates with different diameters are utilized:

- Large size aggregates (gravel and crushed stone)
- Small size aggregates (sand)

In order to achieve a good concrete, the aggregates mixture must be characterized by a correct particle size, obtained by mixing in suitable proportions aggregates of different type. In Figure 3.2 are shown three different mixtures: in the first one, large size aggregates are used, which leads to a mixture characterized by big blanks; in the second one, the usage of small size aggregates reduces the blanks but increases the interface area between aggregates and cement, which, as a discontinuity point, is always a weakness area; in the last one, the mixing of aggregates of different sizes leads to a compound with few blanks and a reduced contact surface.

Figure 3.2. Concrete different compositions according to the aggregates size.

The control of the aggregates size can be carried out through the grading curve of the mixture, which is obtained by plotting in a diagram the percentage by weight of the aggregates which pass in sieves with holes of increasing diameter. A valid criterion for judging the quality of the curve is to verify that it is within a particular zone (zone Fuller).

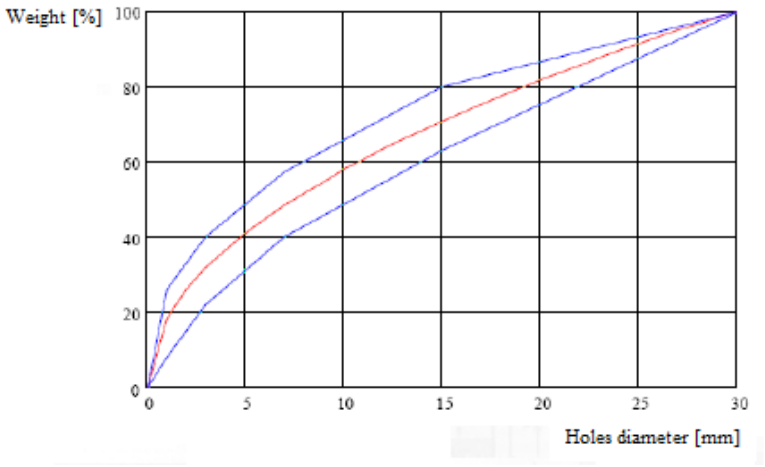

Figure 3.3. Grading curve of the concrete.

Chemical admixtures

Chemical admixtures are materials in the form of powder or fluids that are added to the concrete to give it certain characteristics not obtainable with plain concrete mixes. In normal use, admixture dosages are less than 5% by mass of cement and are added to the concrete at the time of batching/mixing. Examples of chemical admixtures are provided in Appendix B.1.

3.1.2. Production

Concrete production is the process of mixing together the various ingredients (water, aggregates, cement, and additives) to produce concrete. Concrete production is time-sensitive; once the ingredients are mixed, workers must put the concrete in place before it hardens.

The modern concrete is usually prepared as a viscous fluid, so that it may be poured into forms to give it a desired shape.

There is a wide variety of equipment for processing concrete, from hand tools to heavy industrial machineries. Whichever equipment builders use, however, the

objective is to produce the desired building material, thus ingredients must be properly mixed, placed, shaped, and retained within time constraints. Once the mixture is placed, the curing process must be controlled to ensure that the concrete attains the desired attributes. During the concrete preparation, various technical details may affect the quality and the nature of the product.

When initially mixed, Portland cement and water rapidly form a gel of tangled chains of interlocking crystals, and the components of the gel continue to react over time. Initially the gel is fluid, which improves workability and aids the placement of the material, but as the concrete sets, the chains of crystals join into a rigid structure, counteracting the fluidity of the gel and fixing the particles of aggregates in place. During the curing, the cement continues to react with the residual water in a process of hydration. In properly formulated concrete, once this curing process has terminated, the product has the desired physical and chemical properties. Among the qualities typically desired, there are mechanical strength, low moisture permeability, chemical and volumetric stability.

A thorough mixing is essential for the production of uniform, high-quality concrete. The mixing of cement and water into a paste before combining these materials with aggregates can increase the compressive strength of the resulting concrete.

In all the critical applications, care must be taken to properly cure concrete, to achieve the best strength and hardness. This happens after the concrete has been placed.

The cement requires a moist controlled environment to gain strength and harden fully. The cement paste hardens over time, becoming rigid though very weak and gaining strength in the following weeks. In around four weeks, typically over 90% of the final strength is reached, though strengthening may continue for decades.

The hydration and the hardening of concrete during the first three days is critical; abnormally fast drying and shrinkage due to factors such as evaporation and exposition to wind during placement may lead to increased tensile stresses at a time when it has not yet gained sufficient strength, resulting in cracking.

The early strength of the concrete can be increased if it is kept damp during the curing process; moreover, minimizing stress prior to curing minimizes the cracking.

During the curing process concrete must be kept under controlled temperature and humid atmosphere. In practice, this is achieved by spraying or wetting the

concrete surface with water, thereby protecting the concrete mass from ill effects of ambient conditions. Additional common curing methods include the usage of wet burlaps and/or plastic sheeting covering the concrete.
Properly curing concrete leads to increased strength and lower permeability and avoids cracking where the surface dries out prematurely. Care must also be taken to avoid freezing or overheating due to the exothermic settling of cement. Improper curing can cause scaling, reduced strength, poor abrasion resistance and cracking.

3.1.3. Properties

Concrete is strong in compression, as the aggregates efficiently carries the compression loads. However, it is weak in tension as the cement holding the aggregates in place can crack, allowing the structure to fail.
For this reason it is usually reinforced with materials that are strong in tension (often steel). The elasticity of concrete is relatively constant at low stress levels but starts to decrease at higher stress levels as matrix cracking develops. Concrete has a very low coefficient of thermal expansion and shrinks as it matures. All concrete structures crack to some extent, due to shrinkage and tension. Concrete that is subjected to long-duration forces is prone to creep.
In order to guarantee to the concrete structures the desired performances of durability, workability and mechanical resistance, designers are required to execute a detailed study, named “mix design”, regarding the quantity and the characteristics of the mixture components. The mix design depends on the type of structure being built, how the concrete is mixed and delivered, and how it is placed to form the structure. During this phase, several aspects must be taken in consideration, such as:

- The workability increases with the water quantity and depends on the aggregates characteristics (quality, type of surface and dimensions) and on the presence of additives.
- The mechanical resistance is a function of the water/cement ratio and of the quantity of cement utilized: it increases with the reduction of the water/cement ratio and with the enhancement of the cement quantity.
- The durability increases inversely with the water/cement ratio.

As might be expected, the principal parameter which must be considered in the concrete design is the water/cement ratio, as it influences significantly the concrete performances.
For instance, in order to increase the workability, without the usage of additives, it is possible to increase the quantity of water; but even the quantity of cement must be proportionally increased, to maintain the water/cement ratio constant, in order to not compromise the durability and the mechanical resistance.

3.1.4. Classification

There are several ways to classify the concrete. According to the current regulations, for a proper design and construction of the concrete structures, the material must be specified as regards the strength, the consistency, the exposure and the nominal aggregates size.

Classification according to the strength

The first classification of the concrete is made according to the compression strength, expressed as characteristic cubic strength, R_{ck}, or characteristic cylindrical strength, f_{ck}.
The characteristic cubic strength R_{ck} can be achieved by uniaxial compression tests on standard cubic specimens with side 150 mm and aged 28 days, while the characteristic cylindrical strength is obtained utilizing standard cylindrical specimens, with diameter 150 mm and height 300 mm, aged 28 days as well.

Figure 3.4. Example of compression test on a standard cubic concrete specimen.

Those two values are related by the following equation [11]:

$$f_{ck} = 0.83 \cdot R_{ck} \tag{3.1}$$

The difference between them basically depends on the different stress state which arises in the specimens as a result of the compression. This difference is due to the fact that the cubic specimens are squat, while the cylindrical ones are slender; therefore, the second ones are less affected by the confinement stresses caused by the friction which originates on the interface between the specimen and the machine.
The regulation [12], which has become legal regarding all the concrete and reinforced concrete structures, establishes the classification reported in Table 3.1 for the normal and the heavy concrete:

Table 3.1. Concrete classification according to the strength.

Category	Strength class
Non-structural	C8/10
	C12/15
NSC	C16/20
	C20/25
	C25/30
	C28/35
	C30/37
	C32/40
	C35/45
	C40/50
	C45/55
HPC	C50/60
	C55/67
	C60/75
HSC	C70/85
	C80/95
	C90/105
	C100/120

For each strength class, the first value represents f_{ck}, while the second one R_{ck}, both expressed in N/mm^2.

Whether in the mix design a certain percentage of blanks is expected (usually 4-6%), with the purpose of improve the concrete resistance to the freeze-thaw cycles, those values should be reduced by 20%.
According to the strength class, concretes can be divided in four categories:

- Non-structural concretes (C8/10 – C12/15)
- NSC – Normal strength concretes (C16/20 – C45/55)
- HPC – High performances concretes (C50/60 – C60/75)
- HSC – High strength concretes (C70/85 – C100/120)

Classification according to the exposure

The regulation [12] introduces six exposure classes and 17 subclasses according to the extent of degradation which the concrete is exposed to, and indicates the maximum water/cement ratio, the minimum quantity of cement and the minimum strength class necessary to guarantee the durability.

Table 3.2. Concrete classification according to the exposure.

Class	Subclass	Max w/c ratio	Min cement quantity [kg/m^3]	Min strength class
X0 – No risks of reinforcements corrosion				C12/15
Reinforcements corrosion induced by carbonation	XC1 – Dry or permanently wet	0.65	260	C20/25
	XC2 – Wet, rarely dry	0.60	280	C25/30
	XC3 – Moderate humidity	0.55	280	C30/37
	XC4 – Cyclically wet and dry	0.50	300	C30/37
Reinforcements corrosion induced by chlorides (not from sea water)	XD1 – Moderate humidity	0.55	300	C30/37
	XD2 – Wet, rarely dry	0.55	300	C32/40
	XD3 – Cyclically wet and dry	0.45	320	C35/45
Reinforcements corrosion induced by chlorides (from sea water)	XS1 – Exposed to salty but not in direct contact with the sea water	0.50	300	C30/37
	XS2 – Permanently submerged	0.45	340	C35/45
	XS3 – Exposed to splashes of water or tide	0.45	340	C35/45

Freeze-thaw cycles attack, with or without de-icing	XF1 – Moderate water saturation, no de-icing agent	0.55	300	C30/37
	XF2 – Moderate water saturation, with de-icing agent	0.55	300	C25/30
	XF3 – Elevated water saturation, no de-icing agent	0.50	320	C30/37
	XF4 – Elevated water saturation, with de-icing agent	0.45	340	C30/37
Chemical attack by water in the soil and flowing waters	XA1 – Weakly chemically aggressive environment	0.55	300	C30/37
	XA2 – Moderately chemically aggressive environment	0.50	320	C30/37
	XA3 – Highly chemically aggressive environment	0.45	360	C35/45

A further classification, according to the consistency, is described in Appendix B.2.

3.1.5. Mechanical characteristics

Concrete has a very complicated behavior, which cannot be easily represented by a simple equation, like the Hooke's law for metals.
Since the concrete behavior is poorly in conformity with the Hooke's law, its Young's modulus is not constant, as it is for metals. Moreover, since the deviation from the Hooke's law is higher in traction than in compression, the Young's moduli in traction and in compression are different from each other.
Concrete behavior can be approximated by the Hooke's law only when subjected to short duration compression stresses, less intense than 40% of its characteristic cylindrical strength f_{ck}, or to tensile stresses less intense than 70% of the its tensile strength.
The value of the Young's modulus for the concrete is influenced by several parameters such as:

- Strength class (E increases with the strength class)
- Components characteristics

- Water/cement ratio (E increases inversely with the water/cement ratio)
- Production and placement modalities
- Curing modalities

The σ-ε curve of a concrete specimen subjected to compression (see Figure 3.5) shows an initial linear part, until about the 40% of the value f_{ck}.
For higher values of the stress, the diagram becomes parabolic, until a deformation value named ε_{c1}, which corresponds to the stress f_{ck}.
The specimen failure is not instantaneous, since it is due to a micro-cracking process which quickly develops; hence, a descending part follows, which represent the softening behavior. The trend is curvilinear and it ends at the ultimate deformation, named ε_{cu}, to which corresponds a value of stress indicated with σ_{cu}, that is definitely lower than f_{ck}.
Only a very little percentage of the deformation can be restored with the unloading.
As evident, the material shows many relevant characteristics of non-linearity and plasticity, even starting from low values of stress.
Moreover, the deformation is strictly related to the rate whereby the load is applied and to the duration of the load application: the slower and the more lasting load is, the higher deformations are.
Since the concrete behavior cannot be correctly represented by the Young's modulus, like it is for the metals, two different parameters are used to characterize this material [11]:

- Instantaneous tangent modulus E_c
- Instantaneous secant modulus E_{cm}

E_c is taken at the origin of the σ-ε curve. It correctly represent the concrete behavior in compression and for low values of the stress (close to zero). It is instead meaningless (because too high) for higher values, since the curve shows a relevant slope decrease with increasing stress.
E_{cm} is the slope of the secant which goes from the origin to the point whose ordinate is 40% f_{ck}. This value well represents the elastic behavior of the concrete in the ordinary work zone.
Regarding the Poisson's ratio, it is usually comprised between 0.16 and 0.20.
The graphical representation of the concrete behavior shows three main different parts, which can be seen in Figure 3.5.

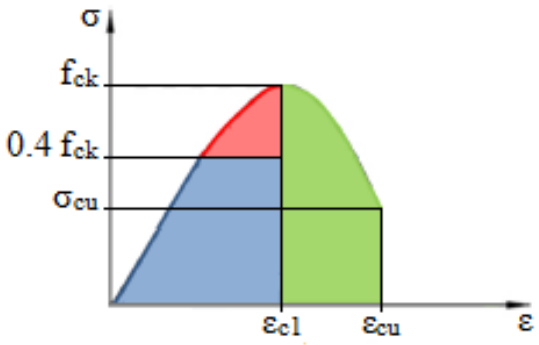

Figure 3.5. Concrete σ-ε typical curve.

The first part (blue) corresponds to the elastic behavior, which follows the Hooke's law:

$$\sigma = E_{cm} \cdot \varepsilon \tag{3.2}$$

The second part (red) corresponds to the plastic behavior, and its extension is related to the material stiffness.
The third part (green) represents the material damage; the stress in this part decrease from its peak to the ultimate value.
As previously told, the concrete is characterized by a compression strength much higher than the tensile strength, as Figure 3.6 shows.

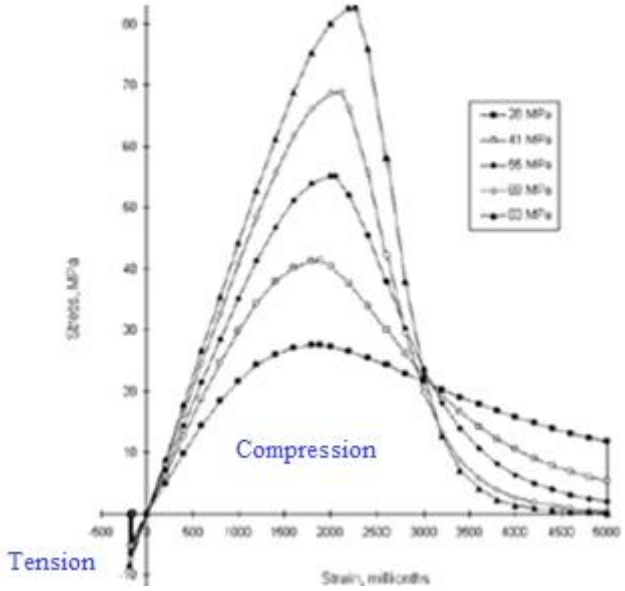

Figure 3.6. Difference between concrete strength in compression and in tension.

Three different simplified models are usually considered to represent the concrete behavior, which are shown in Figure 3.7.

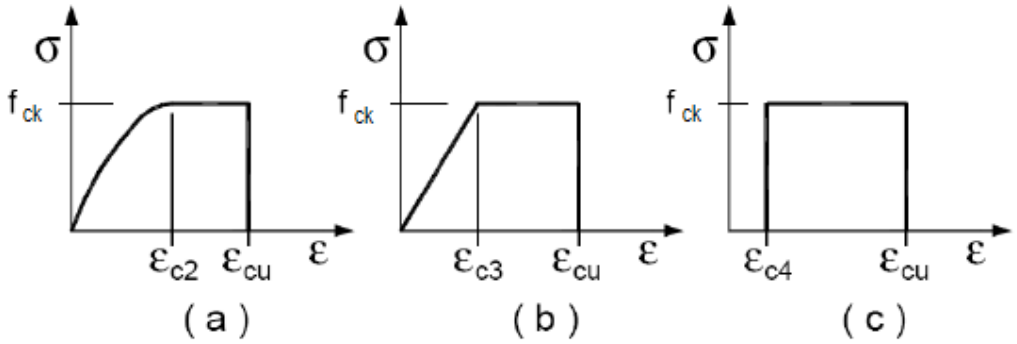

Figure 3.7. Simplified models of the concrete σ-ε curve.

These three model are named parabola-rectangle (a), triangle-rectangle (b) and stress block (c).
For concretes belonging to the classes from C8/10 to C50/60, it is usually assumed:

$\varepsilon_{c2} = 0.20\%$
$\varepsilon_{c3} = 0.175\%$
$\varepsilon_{c4} = 0.07\%$
$\varepsilon_{cu} = 0.35\%$

For concretes belonging to superiors classes:

$\varepsilon_{c2} = 0.20\% + 0.0085\% \cdot (f_{ck} - 50)^{0.53}$
$\varepsilon_{c3} = 0.175\% + 0.055\% \cdot \frac{f_{ck} - 50}{40}$
$\varepsilon_{c4} = 0.2 \cdot \varepsilon_{cu}$
$\varepsilon_{cu} = 0.26\% + 3.5\% \cdot (\frac{90 - f_{ck}}{100})^4$

Regarding the tensile strength it is determined by means of traction tests (Figure 3.8a), but must commonly it is achieved indirectly through other tests, such as the flexion test (Figure 3.8b) or the so called “Brazilian test” (Figure 3.8c); it consists of the application of a load on a concrete specimen along two lines diametrically opposite. This type of load generates an axial stress along the specimen axis.

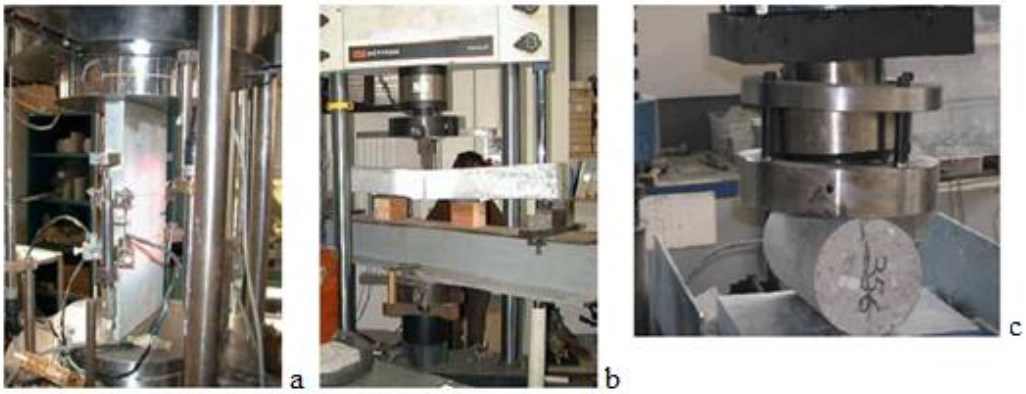

Figure 3.8. Examples of tests to determine the concrete tensile strength: traction test (a), flexion test (b) and Brazilian test (c).

3.2. Concrete numerical models

Concrete is a very common material in modern civil constructions, such as highways, bridges, skyscrapers, etc. The safety of these structures under blast, impact, and ballistic loads has been one of the primary concerns of designers in recent years. However, full-scale structural response tests are costly and difficult to obtain for these types of loads. As a consequence, responses predicted by physics-based numerical analyses have been important resources for both academics and structural engineers to determine the behavior of concrete structures under these loads. Consequently, practitioners are continuously looking for verified and validated numerical models, so that consistent sets of virtual response data can be generated and from which one can study structural behaviors, formulate simplified engineering models, and develop new structural and material designs to have improved resistance to these loads.

To realistically predict the behaviors of concrete structures under various types of loads, the concrete constitutive models should simulate known behaviors at smaller material specimen levels up to the full-scale structural level.

Advances in finite element (FE) methods and material constitutive models have made it feasible to support daily requirements of engineers in designs and assessments.

Among the readily available FE software, LS-Dyna® is widely applied in analyzing structural responses to shock and impact loads, and it provides a variety of concrete constitutive models, such as:

- *MAT_PSEUDO_TENSOR (MAT016)
- *MAT_GEOLOGIC_CAP_MODEL (MAT025)
- *MAT_CONCRETE_DAMAGE (MAT072)
- *MAT_SOIL_CONCRETE (MAT078)
- *MAT_WINFRITH_CONCRETE (MAT084)
- *MAT_BRITTLE_DAMAGE (MAT096)
- *MAT_JOHSON_HOLMQUIST_CONCRETE (MAT111)
- *MAT_CSCM_CONCRETE (MAT159)

Each of these models has its own advantages and disadvantages, therefore, FE analysts are actually facing a wide range of choices.
Concrete is a pressure dependent material, hence, the general form of the yield function can be written as:

$$Y(I_1, J_2, J_3) = 0 \tag{3.3}$$

where I_1 is the 1st invariant of the stress tensor, which represents the volumetric responses; J_2 and J_3 are the 2nd and 3rd invariants of the deviatoric stress tensor and they account for the deviatoric responses. In general, the primary difference between various concrete constitutive models is how the deviatoric and volumetric responses are characterized.

Continuous Surface Cap model

The CSC model is aimed at roadside safety analyses. It appears in LS-Dyna® in two versions, *MAT_CSCM_CONCRETE and *MAT_CSCM [13], [14], [15].
The "_CONCRTE" suffix indicates a short input format that utilizes default values for numerous variables, while the other name indicates a long input format for which the user must supply values for all the required input parameters. The short input format will work with default model parameters based only on the user supplied compression strength and maximum aggregates size.
The CSC model defines and combines two surfaces, the shear (failure) surface and the hardening compaction surface (cap), by using a multiplicative formulation, in order to achieve a smooth and continuous intersection between them. The smooth intersection eliminates the numerical complexity of treating a compressive "corner" region between failure surface and cap.

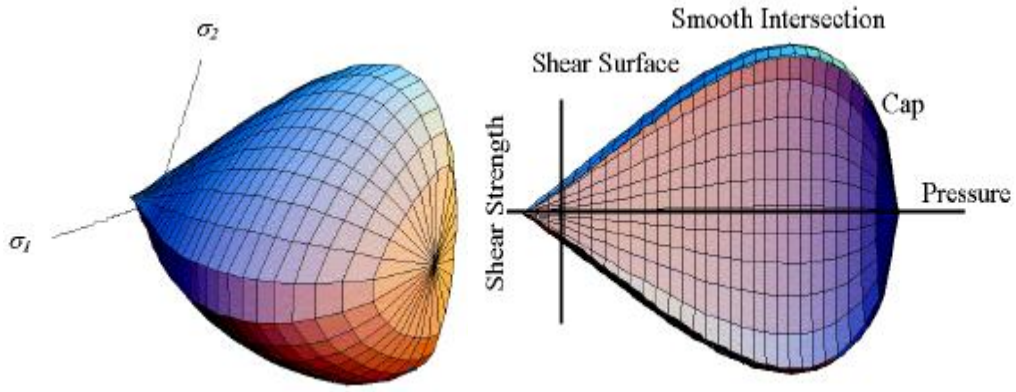

Figure 3.9. MAT159: combination of failure surface and hardening cap [15].

Failure surface

The failure surface represents all stress configurations (σ_1, σ_2, σ_3) in correspondence of which the concrete reaches its maximum strength and the damage begins. All the stress configurations characterized by a point inside this surface correspond to a non-damaged state.
This surface is centered on the hydrostatic pressure axis:

$$p = \frac{\sigma_{kk}}{3} = \frac{(\sigma_1 + \sigma_2 + \sigma_3)}{3} \tag{3.4}$$

with $\sigma_1 = \sigma_2 = \sigma_3$.

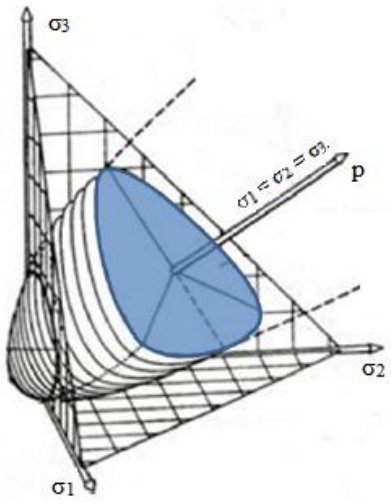

Figure 3.10. MAT159: development of the failure surface along the hydrostatic axis [14].

For negative values of p, which means for a triaxial extension with $\sigma_1 = \sigma_2 = \sigma_3$, the rupture occurs much more quickly, and the surface terminates on the correspondent point on the axis.
Instead, in case of triaxial compression with $\sigma_1 = \sigma_2 = \sigma_3$, the surface has no end, since the concrete rupture does not occur if the element is subjected to this stress state.
The failure surface is approximated by the software by means of three sets of meridians, which are curves outgoing from the origin:

- The meridians of compression
- The meridians of tension
- The meridians of torsion

The meridians of compression correspond to a stress state $\sigma_i = \sigma_j$ and σ_k = max. It is achieved by imposing a biaxial confinement while one of the principal stresses is increased until the rupture value.
There are three meridians of compression; each of them corresponds to the variation of one principal stress. In Figure 3.11, the three red points represent the intersection between those meridians and a generic deviatoric plane, hence a plane perpendicular to the hydrostatic pressure axis p.

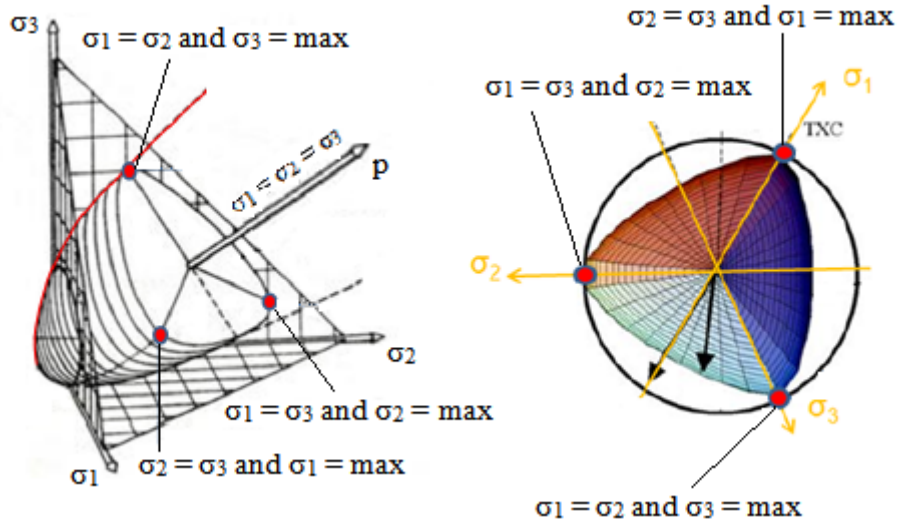

Figure 3.11. MAT159: meridians of compression [14].

The meridians of tension correspond to a stress state $\sigma_i = \sigma_j$ and σ_k = min. It is achieved by imposing a biaxial confinement while one of the principal stresses is decreased until the rupture value.
There are three meridians of tension; each of them corresponds to the variation of one principal stress. In Figure 3.12, the three red points represent the intersection between those meridians and a generic deviatoric plane.

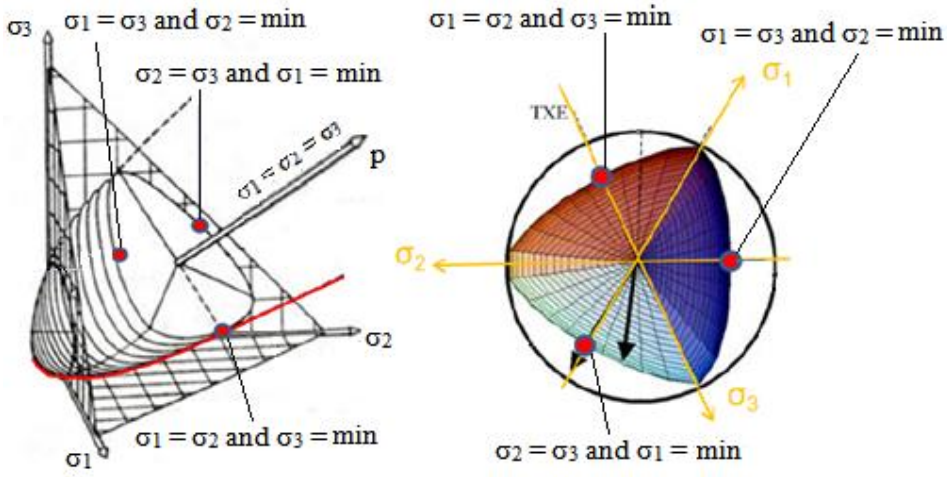

Figure 3.12. MAT159: meridians of tension [14].

The meridians of torsion are the curves correspondent to the intersection between the failure surface and the planes identified by the two straight lines $\sigma_1=\sigma_2=\sigma_3$ and $\sigma_i = -\sigma_j$, $\sigma_k = 0$.
In Figure 3.13, the six red points represent the intersection between those meridians and a generic deviatoric plane.

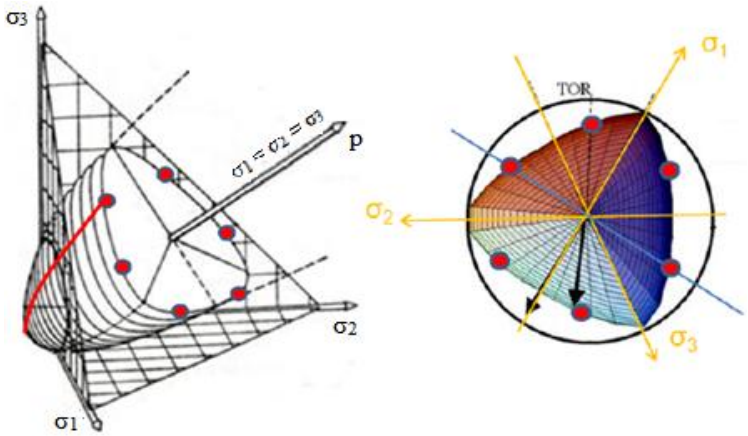

Figure 3.13. MAT159: meridians of torsion [14].

The determination of these meridians is made as low as the 1st invariant of the stress tensor **T** and the 2nd and 3rd invariants of the deviatoric stress tensor $\mathbf{T_d}$:

$$\mathbf{T} = \begin{bmatrix} \sigma_{11} & \sigma_{12} & \sigma_{13} \\ \sigma_{21} & \sigma_{22} & \sigma_{23} \\ \sigma_{31} & \sigma_{32} & \sigma_{33} \end{bmatrix} \tag{3.5}$$

$$\mathbf{T_d} = \begin{bmatrix} \sigma_{11} - p & \sigma_{12} & \sigma_{13} \\ \sigma_{21} & \sigma_{22} - p & \sigma_{23} \\ \sigma_{31} & \sigma_{32} & \sigma_{33} - p \end{bmatrix} \tag{3.6}$$

$$I_1 = \mathrm{tr}(\mathbf{T}) = \sigma_{11} + \sigma_{22} + \sigma_{33} \tag{3.7}$$

$$J_2 = \frac{1}{2} \cdot (s_{ij} \cdot s_{ij}) \tag{3.8}$$

$$J_3 = \det(\mathbf{T_d})$$

with

$$s_{ij} = \sigma_{ij} - p \cdot \delta_{ij} \tag{3.9}$$

where δ_{ij} is the Kronecker's delta.
The failure surface equation, considering firstly the meridians of compression, is the following:

$$f(I_1, J_2) = J_2 - F_f^2 = 0 \tag{3.10}$$

where

$$F_f = \alpha - \lambda \cdot e^{-\beta \cdot I_1} + \theta \cdot I_1 \tag{3.11}$$

Here the values of α, θ, λ, β are selected by fitting the model surface to strength measurements from triaxial compression tests conducted on plain concrete cylinders; they are respectively:

- α – Triaxial compression surface constant term
- θ – Triaxial compression surface linear term
- λ – Triaxial compression surface non-linear term
- β – Triaxial compression surface exponent

The meridians of tension and torsion are built starting from the function F_f, through two multiplicative coefficients.
For the torsion:

$$Q_1 = \alpha_1 - \lambda_1 \cdot e^{-\beta_1 \cdot I_1} + \theta_1 \cdot I_1 \tag{3.12}$$

where

- α_1 – Triaxial torsion surface constant term
- θ_1 – Triaxial torsion surface linear term
- λ_1 – Triaxial torsion surface non-linear term
- β_1 – Triaxial torsion surface exponent

For the tension:

$$Q_2 = \alpha_2 - \lambda_2 \cdot e^{-\beta_2 \cdot I_1} + \theta_2 \cdot I_1 \tag{3.13}$$

where

- α_2 – Triaxial tension surface constant term
- θ_2 – Triaxial tension surface linear term
- λ_2 – Triaxial tension surface non-linear term
- β_2 – Triaxial tension surface exponent

Q_1 represent the ratio between the torsion strength and the compression strength, while Q_2 is the ratio between the tension strength and the compression strength.

The failure surface as defined by equation (3.10) is characterized by a circular section. The Rubin's function $R(I_1,J_2,J_3)$ will be now introduced; it permits to achieve the final form of the failure surface.
The failure surface equation becomes:

$$f(I_1, J_2, J_3) = J_2 - R^2 \cdot F_f^2 = 0 \tag{3.14}$$

The Rubin's function is the following:

$$R = \frac{-b_1 + \sqrt{b_1^2 - 4 \cdot b_2 \cdot b_0}}{2 \cdot b_2} \tag{3.15}$$

The parameters present in Rubin's function can be calculated as low as the second and the third invariants J_2 and J_3. The function R equals:

- 1 in correspondence of the meridian of compression
- Q_1 in correspondence of to the meridian of torsion
- Q_2 in correspondence of the meridian of tension

Elasticity limit surface

As low as the failure surface above described, another surface has to be defined, which corresponds to the entrance of the material into the plastic field.
This second surface is placed inside the first one, which means that when the concrete reaches its elastic limit, it begins to deform plastically until the rupture.
The shape of the concerned surface is shown in Figure 3.14.

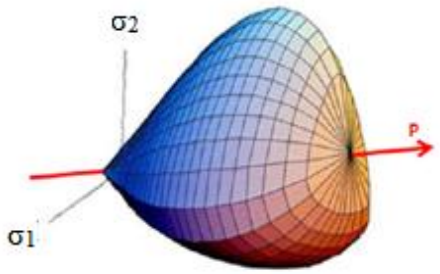

Figure 3.14. MAT159: elasticity limit surface [15].

It is comparable to the failure surface as far as concerns stress states due to negative pressure and low positive pressure, while in the case of higher pressures, moving forward along the axis $\sigma_1 = \sigma_2 = \sigma_3$, the surface narrows and terminates on a point on that axis.
The elasticity limit surface can be achieved in two steps:

- The first part of the surface (for negative and low positive pressures) is obtained from the function representing the failure surface, F_f, introducing two coefficients, N_H and C_H.
- The second part of the surface (for high positive pressures) is obtained defining a new function, F_C.

The first coefficient to be introduced is named N_H; its value is comprised between 0.7 and 1. The function F_f is multiplied by this new parameter in order to achieve a reduced surface.
Figure 3.15 shows a section of the two concerned surfaces.

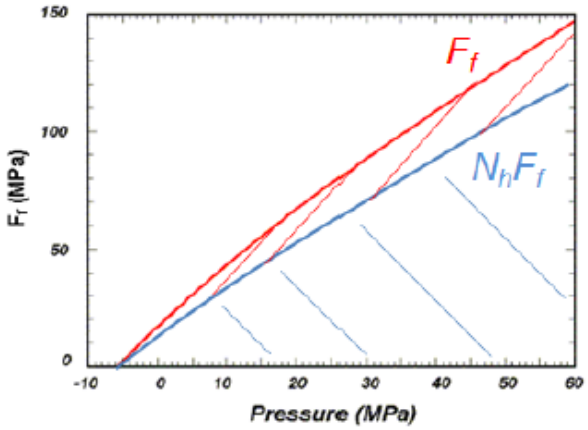

Figure 3.15. MAT159: achievement of the elasticity limit surface from the failure surface [14].

The equation of the new surface is

$$f(I_1, J_2, J_3) = J_2 - R^2 \cdot N_H^2 \cdot F_f^2 = 0 \qquad (3.16)$$

The value of the parameter N_H ($0.7 < N_H < 1$) influences the plastic behavior of the material; if $N_H = 1$, the plastic behavior is not considered at all.
The second required parameter is named C_H and it necessary to define the evolution of the stress in the plastic field.

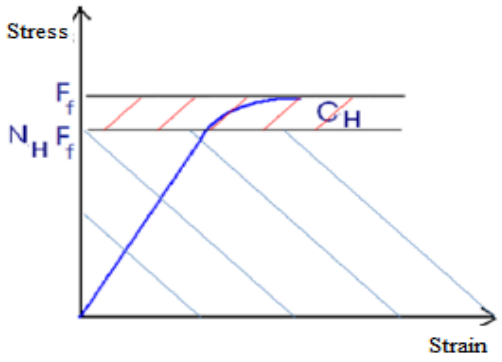

Figure 3.16. MAT159: role of the parameter C_H in the σ-ε curve [14].

The second step is to define the function F_C, which represents a surface called "hardening cap", by which the function F_f will be multiplied, in order to achieve a final closed surface, composed by two surfaces, smoothly and continuously combined, as shown in the Figure 3.17.

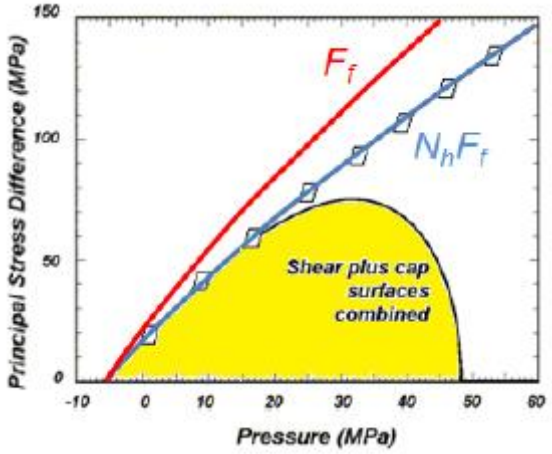

Figure 3.17. MAT159: section of the elasticity limit surface [14].

The function F_C is equal to 1 until a certain value of I_1, and decreases progressively over that value:

$$F_C(I_1, \kappa) = \begin{cases} 1 - \frac{(I_1 - \kappa)^2}{(X - \kappa)^2} & I_1 \geq \kappa \\ 1 & I_1 < \kappa \end{cases} \qquad (3.17)$$

Figure 3.18 shows the trend of the function F_C.

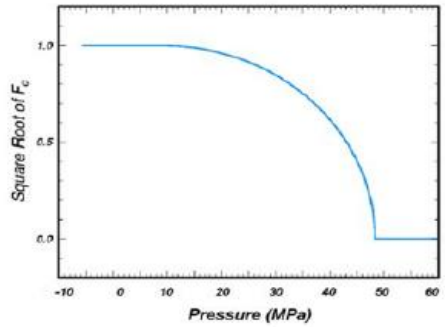

Figure 3.18. MAT159: function F_C [15].

κ is the value of I_1, hence of pressure, from which F_C begins to decrease. Thus, the intersection of the two surfaces is at $I_1 = \kappa$.
X(κ) is the value of I_1 in correspondence of which the surface F_C terminates, hence $F_C = 0$. The intersection of the surface F_C with the I_1 axis is at $I_1 = X(\kappa)$.

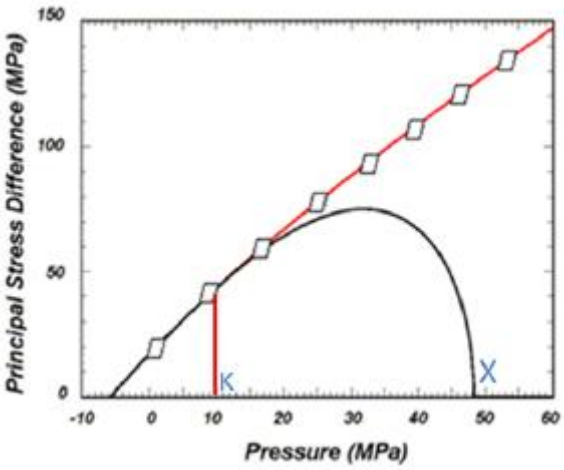

Figure 3.19. MAT159: parameters κ and X [15].

The function F_C is then multiplied by the function F_f in order to achieve a smooth and continuous matching of the two surfaces; the final formula representing the elasticity limit surface is the following:

$$f(I_1, J_2, J_3, \kappa) = J_2 - R^2 \cdot N_H^2 \cdot F_f^2 \cdot F_C = 0 \qquad (3.18)$$

Damage

As explained in Paragraph 3.1.5, after the elastic and the plastic fields, once the stress reaches its peak, the damage occurs and the stress begins to decrease; the third section of the σ-ε curve corresponds to the concrete damage, which is pointed out in Figure 3.20.

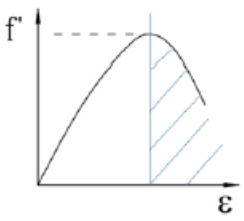

Figure 3.20. MAT159: damage area in the σ-ε curve [14].

Concrete exhibits softening (strength reduction) in the tensile and low to moderate compressive regimes; softening is modeled via a damage formulation. Without the damage formulation, the cap model predicts perfectly plastic behavior.
The damage formulation models both strain softening and modulus reduction. Strain softening is a decrease in strength during progressive straining after a peak strength value is reached. Modulus reduction is a decrease in the loading/unloading slopes typically observed in cyclic load/unload tests, shown in Figure 3.21.

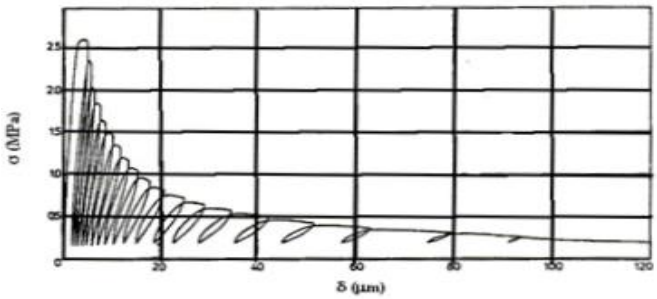

Figure 3.21. MAT159: modulus reduction typical of the cyclic load/unload tests [15].

The phenomenon of damage is modeled through the following equation:

$$\sigma_{ij}^{d} = (1 - d) \cdot \sigma_{ij}^{vp} \tag{3.19}$$

The equation is simpler in the case of uniaxial stress state:

$$\sigma^{d} = (1 - d) \cdot f' \tag{3.20}$$

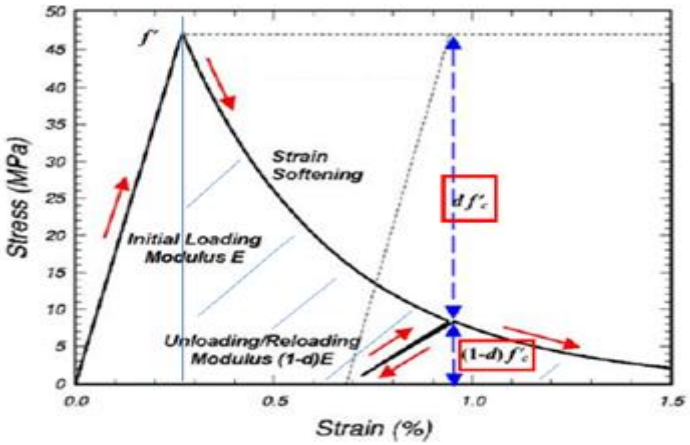

Figure 3.22. MAT159: damage, modulus reduction and strain softening in the σ-ε curve [15].

Here d is a scalar damage parameter that transforms the stress tensor without damage, denoted σ_{ij}^{vp}, into the stress tensor with damage, denoted σ_{ij}^{d}. The damage parameter d ranges from 0 for no damage to 1 for complete damage. Thus (1 – d) is a reduction factor whose value depends on the accumulation of damage. The effect of this factor is to reduce the bulk modulus and the shear modulus isotropically (simultaneously and proportionally).
Damage initiates and accumulates when strain-based energy terms exceed the damage threshold. Damage accumulation via the parameter d is based on two distinct formulations, called brittle damage and ductile damage.
Brittle damage accumulates when the pressure is tensile; it does not when the pressure is compressive.
Brittle damage accumulation depends on the maximum principal strain, ε_{max}, as follows:

$$\tau_b = \sqrt{E \cdot \varepsilon_{max}^2} \tag{3.21}$$

Here τ_b is an energy-type term that depends on the accumulation of total strain via ε_{max}. Brittle damage initiates when τ_b exceeds an initial threshold r_{0b}.
Ductile damage accumulates when the pressure is compressive; it does not when the pressure is tensile.
Ductile damage accumulation depends on the total strain components, ε_{ij}, as follows:

$$\tau_d = \sqrt{\frac{1}{2} \cdot \sigma_{ij} \cdot \varepsilon_{ij}} \tag{3.22}$$

Here τ_d is an energy-type term. σ_{ij} are the stress components calculated before the application of damage.
Ductile damage initiates when τ_d exceeds an initial threshold r_{0d}.
The initial damage threshold is expressed as:

$$r_0 = \left(1 + \frac{\sqrt{E} \cdot \dot{\varepsilon} \cdot \eta}{r^s}\right) \cdot r^s \tag{3.23}$$

where

$$\eta = \frac{\eta_0}{\dot{\varepsilon}^N} \tag{3.24}$$

r^s and r_0 are respectively the static and dynamic energy thresholds, which means without and with the influence of the viscoplasticity, from which the damage begins. The parameters η_0 and N are needed to take in account the strain rate $\dot{\varepsilon}$.

As damage accumulates, the parameter d increases from an initial value of zero, towards a maximum value of 1. Damage accumulates with τ according to the following functions.
In case of brittle damage:

$$d(\tau_b) = \frac{d_{max}}{D} \cdot \left[\frac{1 + D}{1 + D \cdot e^{-C \cdot (\tau_b - r_{0b})}} - 1\right] \tag{3.25}$$

In case of ductile damage:

$$d(\tau_b) = \frac{d_{max}}{B} \cdot \left[\frac{1 + B}{1 + B \cdot e^{-A \cdot (\tau_d - r_{0d})}} - 1\right] \tag{3.26}$$

The parameters A and B or C and D set the shape of the softening curve plotted as stress-displacement or stress-strain. The parameter d_{max} is the maximum damage level that can be attained. It is set equal to approximately 1 in the tensile and low confining pressure regimes.

4. Tests on concrete specimens

The Department of Civil Engineering of the University of Liège (ULg) performed several experimental tests on concrete standard specimens, in order to characterize this material. Afterwards, those tests have been reproduced in LS-Dyna® and a numerical-experimental correlation procedure has been fulfilled in order to calibrate the concrete model.
This chapter presents the experimental tests description and results and the numerical-experimental correlation of the correspondent developed models.

4.1. Experimental tests description

Specimens production

The standard [12] regulates the production of concrete specimens.
As explained in Paragraph 3.1.1, the three main components of the concrete are:

- Water
- Cement
- Aggregates

Three concrete types have been produced, which differ to each other for the water/cement ratio and the cement used.

Table 4.1. Types of concrete produced.

Concrete	W/C ratio	Cement
MC(0.45) – CEM I 52.2	0.45	Portland CEM I 52.5
MC(0.50) – CEM I 52.2	0.50	Portland CEM I 52.5
MC(0.45) – CEM I 42.2	0.45	Portland CEM I 42.5

The composition of the aggregates of quartz used is defined in Table 4.2.

Table 4.2. Composition of the aggregates.

Diameter [mm]	Percentage [%]	Mass [Kg]
0.1 – 0.5	25	33.02
0.5 – 1	12	15.85
1 – 2	15	19.81

2 – 3	10	13.21
3 – 5	18	23.78
5 – 8	20	26.42
Total	**100**	**132.09**

Table 4.3 lists the densities of the components:

Table 4.3. Densities of the components.

Component	Density [Kg/m^3]
Cement	3100
Water	1000
Aggregates	2650

The total volume of concrete produced is 1 m^3.
The production of the concrete specimens consists of the following phases:

- Phase 1 – The internal walls of the mixing machine are humidified.
- Phase 2 – All the aggregates are put into the mixing machine.
- Phase 3 – The machine is activate and the aggregates are mixed for about 1 min.
- Phase 4 – 50% of water and the entire quantity of cement are put into the mixing machine.
- Phase 4 – The machine mixes the components for about 2 min.
- Phase 5 – The remaining part of water is put into the mixing machine.
- Phase 6 – The machine mixes for about 2 min.
- Phase 7 – The mixture achieved is poured into a transportable container.
- Phase 8 – The internal walls of the molds are sprinkled with oil, to facilitate the following extraction of the specimens.
- Phase 9 – Half the molds are filled.
- Phase 10 – The molds are placed on a vibrating table for about 10-15 sec, to homogenize the mixture.
- Phase 11 – The molds are filled until the top.
- Phase 12 – The molds are again placed on the vibrating table.

Figure 4.1 shows some steps of the procedure: the mixing machine filled with the aggregates, the vibrating table, the molds filled with the mixture (the yellow ones contain the mixture already vibrated, the white ones the mixture not yet vibrated).

Figure 4.1. Three steps of the concrete production: the mixing machine (on the left), the vibrating table (in the middle) and the molds filled with the mixture (on the right).

The specimens must remain into the molds for a period comprised between 16 hours and 3 days, at a temperature of 20 °C; during this phase they must be protected by any possible impact and by an excessive drying, which may be caused by the exposition to the sun or the wind.
Afterwards, they must be extracted from the molds and immersed in water or placed in a particular room where temperature and humidity are strictly controlled: the temperature must be 20 °C and the air relative humidity must be not less than 95%. This phase lasts 28 days; afterwards, the specimens are ready to be tested.

Tests description

The following tests have been performed:

- Uniaxial compression test on cubic specimens
- Uniaxial compression test on cylindrical specimens
- Hydrostatic compression test on cylindrical specimens
- Triaxial compression test on cylindrical specimens
- Triaxial extension test on cylindrical specimens
- Uniaxial strain test on cylindrical specimens

For statistical reasons, several tests of each type have been performed, in order to have accurate values.
The specimens have been tested by applying axial and lateral loads (stresses) and recording the corresponding axial and lateral displacements (strains) [16].
In Figure 4.2, σ_1 and $\sigma_3 = \sigma_2$ represent the principal stress components applied to the specimen.

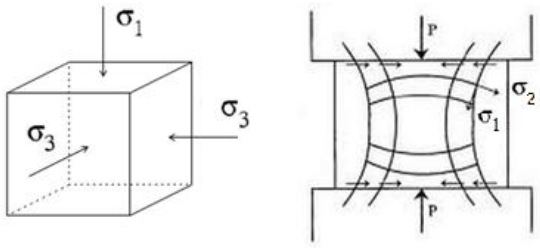

Figure 4.2. Schematization of principal stresses acting on a concrete cubic specimen during a compression test.

Hydrostatic compression test (HSC)

In this test the axial and lateral stresses are equal:

$$\sigma_1 = \sigma_3 = \sigma \tag{4.1}$$

The specimen is in a state of hydrostatic compression with a pressure

$$p = \frac{\sigma_{kk}}{3} = \frac{(\sigma_1 + 2 \cdot \sigma_3)}{3} = \sigma \tag{4.2}$$

The corresponding measured axial and lateral strain components provide the volumetric strain:

$$\varepsilon_v = \varepsilon_{kk} = \varepsilon_1 + 2 \cdot \varepsilon_3 \tag{4.3}$$

The corresponding pressure vs. volumetric strain response describes the compaction behavior of the material.
The first phase of this curve is the initial elastic response and the slope of this segment is the bulk modulus K, which is the main purpose of this test.

Triaxial tests

In these tests the axial and lateral stresses are not equal. Hence, the cylindrical specimen is subjected to a shear stress, which is characterized by the stress difference between the axial and lateral stresses:

$$SD = \sigma_1 - \sigma_3 \tag{4.4}$$

The triaxial tests must be performed in two steps:

1. The specimen is loaded in hydrostatic compression to a predetermined pressure.

2. Either the lateral stress is held constant while the axial stress is increased (triaxial compression test – TXC), or the axial stress is held constant and the lateral stress is increased (triaxial extension test – TXE).

Uniaxial compression test (UCT)

This is a special case of the triaxial test, in which the lateral (confining) stress is zero, i.e. $\sigma_3 = 0$.
The corresponding value of the axial stress, when the specimen fails, is the unconfined compression strength, which is the purpose of this test.

Uniaxial strain test (UXE)

In this test the lateral confinement is continuously adjusted to maintain to zero the circumferential strain while the axial load is increased.
Alternatively, the specimen is placed in a rigid cylinder which prevents lateral displacement.
From this test, the shear modulus G can be achieved:

$$SD = \frac{2 \cdot G}{K} \cdot p \tag{4.5}$$

where K is bulk modulus, achieved from the HSC, and

$$p = \frac{\sigma_{kk}}{3} = \frac{(\sigma_1 + 2 \cdot \sigma_3)}{3} \tag{4.6}$$

$$SD = \sigma_1 - \sigma_3 \tag{4.7}$$

4.2. Tests results and experimental-numerical correlation

The numerical-experimental correlation has been carried out only for the first two tests performed:

- Uniaxial compression test on cubic specimens
- Uniaxial compression test on cylindrical specimens

Uniaxial compression test on cubic specimens

This test has been performed on five cubic specimens for each of the three concrete types listed in Table 4.1.

The results of these tests are shown in Tables 4.4, 4.5 and 4.6.

Table 4.4. Results of the tests on cubic specimens made of MC(0.45) – CEM I 52.2.

MC(0.45) – CEM I 52.2					
Specimen	**Mass [Kg]**	**Dimension [mm]**	**Density [Kg/m^3]**	**Failure load [kN]**	**Failure stress [MPa]**
1	7.85	150x150x150	2330	1500	66.7
2	7.85	150x150x150	2330	1415	62.9
3	7.80	150x150x150	2310	1455	64.7
4	7.85	150x150x150	2330	1500	66.7
5	8.10	153x150x150	2350	1515	66.0
Average failure stress: R_{ck} = 65.4 MPa					

Table 4.5. Results of the tests on cubic specimens made of MC(0.50) – CEM I 52.2.

MC(0.50) – CEM I 52.2					
Specimen	**Mass [Kg]**	**Dimension [mm]**	**Density [Kg/m^3]**	**Failure load [kN]**	**Failure stress [MPa]**
1	7.60	147x150x150	2300	1250	56.7
2	7.85	150x150x150	2330	1330	59.1
3	7.65	148x150x150	2300	1225	55.2
4	7.60	147x150x150	2300	1260	57.1
5	7.80	150x150x150	2310	1300	57.8
Average failure stress: R_{ck} = 57.2 MPa					

Table 4.6. Results of the tests on cubic specimens made of MC(0.45) – CEM I 42.2.

MC(0.45) – CEM I 42.2					
Specimen	**Mass [Kg]**	**Dimension [mm]**	**Density [Kg/m^3]**	**Failure load [kN]**	**Failure stress [MPa]**
1	7.75	150x150x150	2300	1180	52.4
2	7.70	150x150x150	2290	1190	52.9
3	7.80	150x150x150	2310	1160	51.6
4	7.70	150x150x150	2280	1150	51.1
5	7.75	150x150x150	2300	1170	52.0
Average failure stress: R_{ck} = 52.0 MPa					

Figure 4.3 shows the data dispersion for these tests.

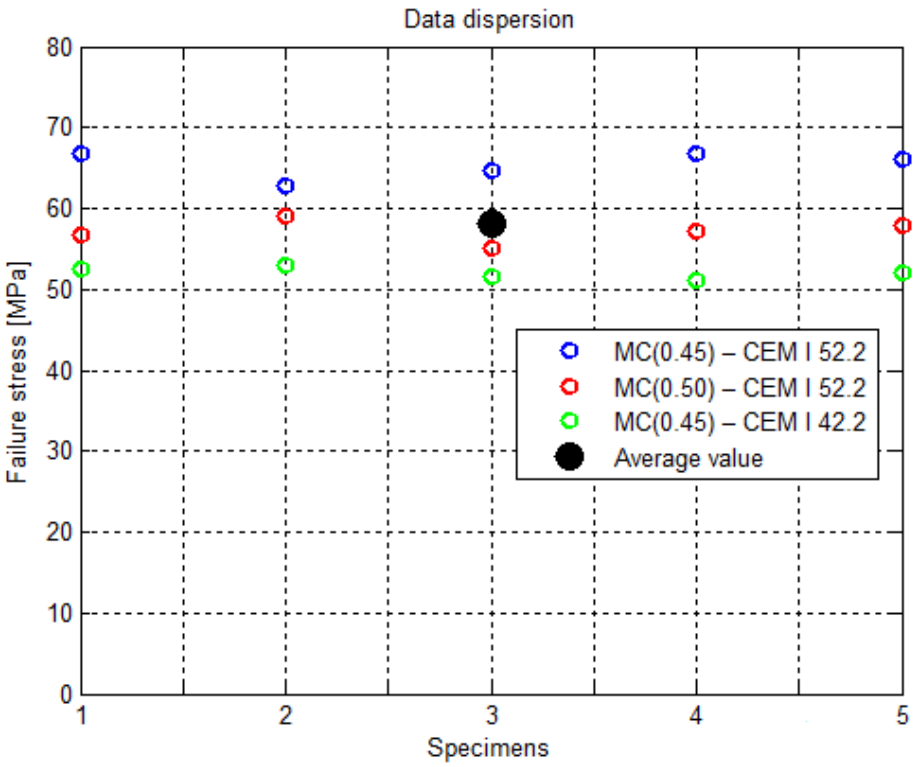

Figure 4.3. Data dispersion for the uniaxial compression test on cubic specimens.

As notable, the concrete strength is much higher than the expected level; theoretically, indeed, this concrete, which belongs to the class C30/37, should show an ultimate cubic compression strength of 37 MPa. The reason why the value achieved experimentally is higher is the very good quality of the concrete produced: the components have been mixed in the perfect quantity, strictly following the production norms and letting the samples rest in water at the right temperature for 28 days; instead, concrete structures built in an open yard, where follow perfectly the norms is more difficult and the concrete is subjected to the weather agents instead of resting in water, may show a lower strength.
The value of 37 MPa is just the minimum guaranteed strength, but often, like in these cases, that value is higher, as happens for the metals.
The only information achieved from these tests concern the ultimate compression strength and the failure shape, which is always hourglass; in some cases (see Figure 4.5) the hourglass shape is very enhanced, in other cases just a thin surface detaches from the lateral sides of the specimen.
The test has been numerically reproduced; the model is shown in Figure 4.4.

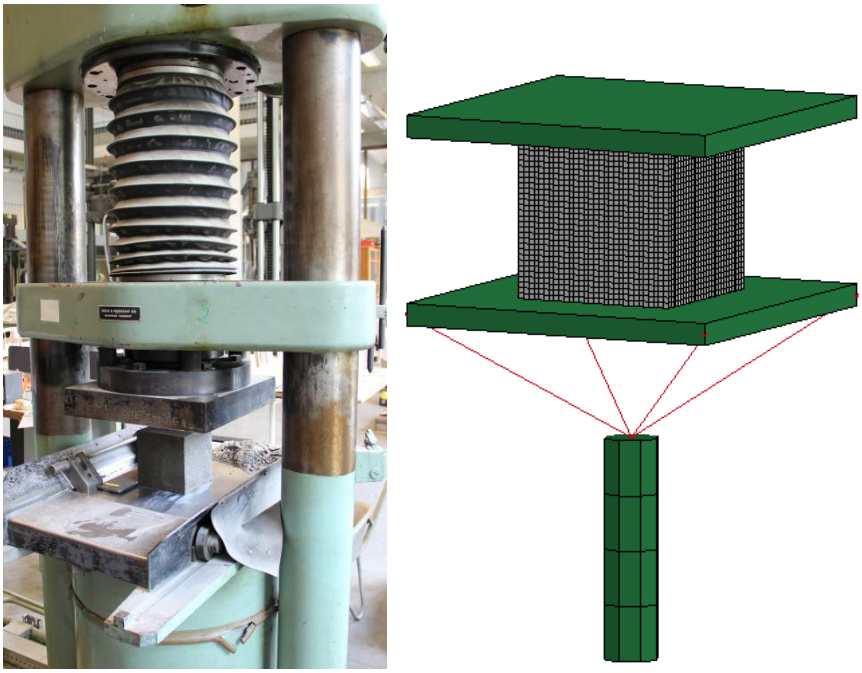

Figure 4.4. Comparison between the experimental and the numerical compression tests on cubic specimens.

Figure 4.5 shows a comparison between the failure shapes in the two cases, experimental and numerical.

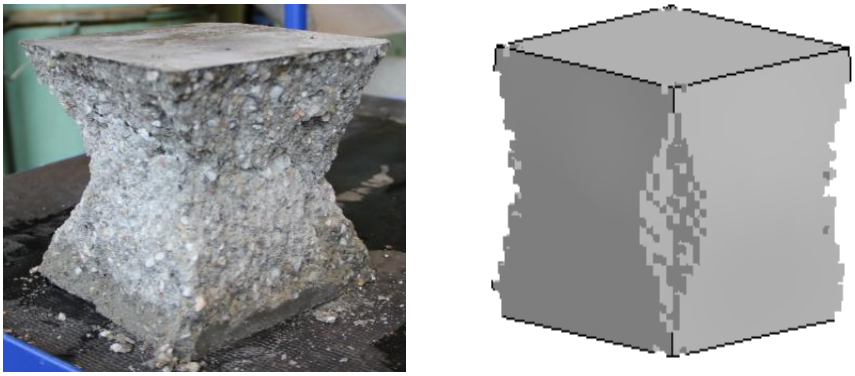

Figure 4.5. Comparison between the experimental and the numerical failure shapes for the compression test on cubic specimens.

The ultimate compression strength numerically achieved is 36.88 MPa, very close to the theory. Table 4.7 shows a comparison between the three ultimate compression strengths: theoretical, numerical and experimental (average).

Table 4.7. Theoretical, numerical and experimental values of R_{ck}.

	Theory	Numerical simulation	Experimental test
R_{ck} [MPa]	37	36.88	58.2

Uniaxial compression test on cylindrical specimens

This second test has been performed on cylindrical specimens made of the concrete type MC(0.45) – CEM I 42.2.
The information achieved from these tests are:

- Axial stress vs. axial strain curves (σ_1-ε_1)
- Axial stress vs. transversal strain curves (σ_1-ε_3)
- Failure shapes
- Ultimate cylindrical compression strengths

The ultimate strengths achieved are shown in Table 4.8.

Table 4.8. Results of the tests on cylindrical specimens.

Specimen	Mass [g]	Diameter [mm]	Height [mm]	Density [Kg/m^3]	Failure stress [MPa]
1	424.44	5.05	9.448	2243	31.90
2	450.85	5.05	9.909	2272	27.80
3	451.88	5.05	10.06	2242	26.40
4	55.72	2.38	5.599	2237	31.60
5	55.54	2.38	5.66	2206	21.90
6	55.49	2.383	5.603	2221	31.10
7	55.81	2.38	5.519	2273	23.72
Average failure stress: f_{ck} = 27.77 MPa					

Figure 4.6 shows the data dispersion for this test.

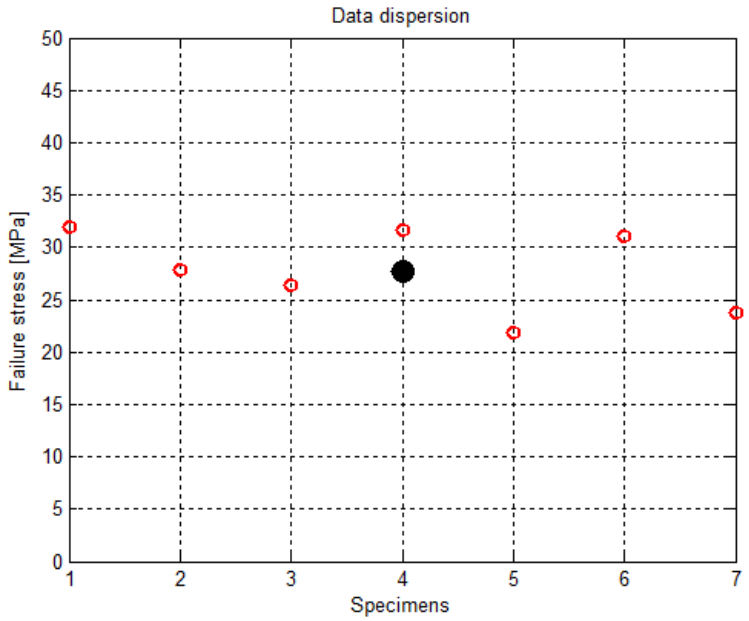

Figure 4.6. Data dispersion for the uniaxial compression test on cylindrical specimens.

Figure 4.7 shows a comparison between the numerical model and the experimental tests, after the specimen failure.

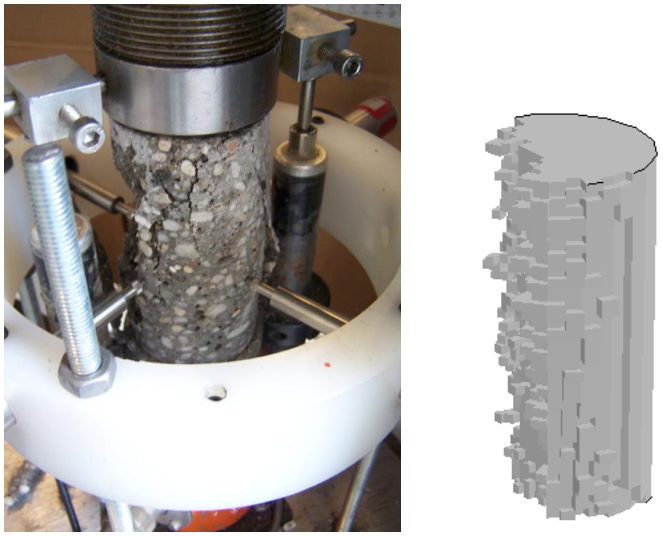

Figure 4.7. Comparison between the experimental and the numerical failure shapes for the compression test on cylindrical specimens.

Figures 4.8 and 4.9 show a numerical-experimental comparison between the trend of the curves σ_1-ε_1 and σ_1-ε_3.

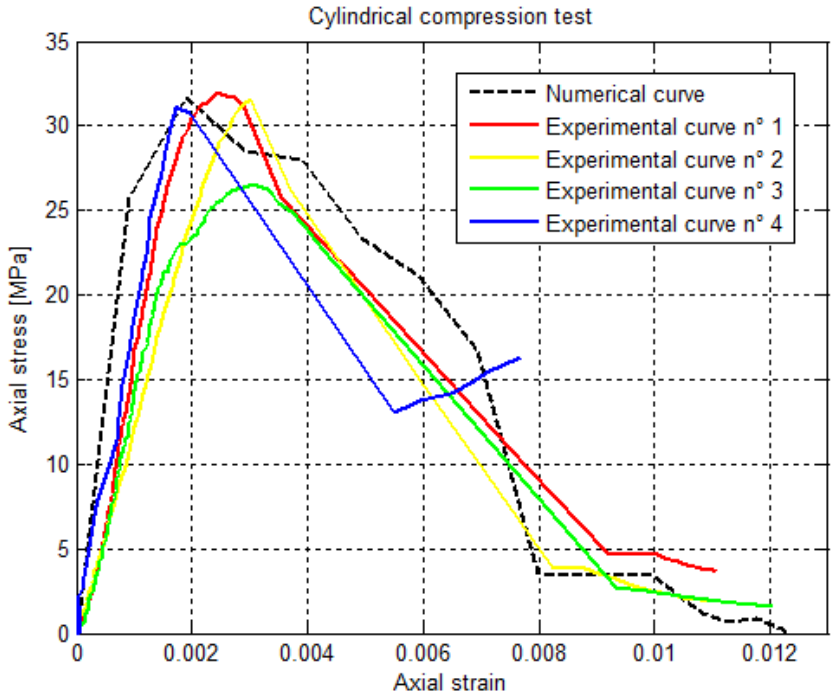

Figure 4.8. Experimental-numerical comparison of the σ_1-ε_1 curve.

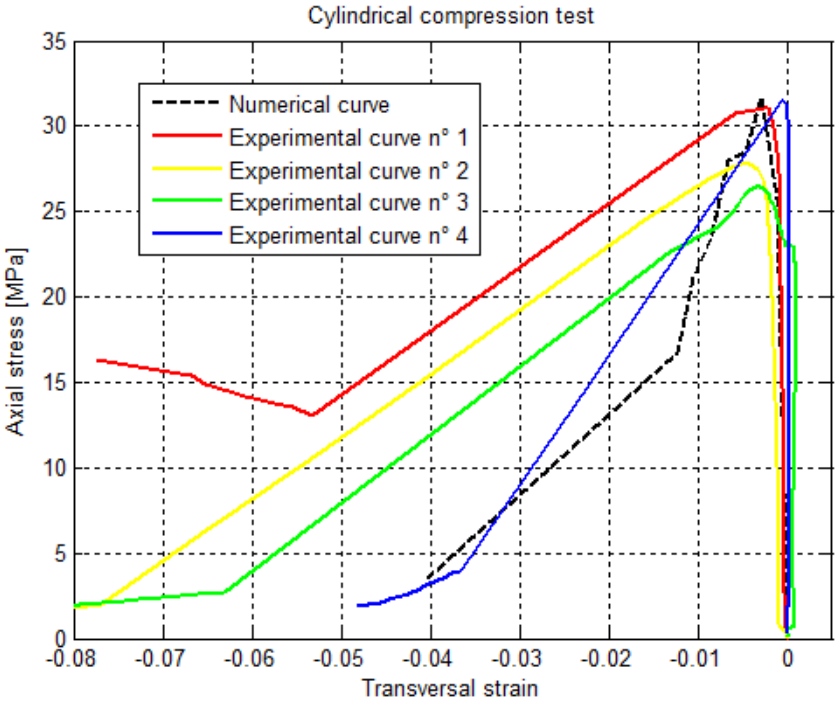

Figure 4.9. Experimental-numerical comparison of the σ_1-ε_3 curve.

Table 4.9 shows a comparison between the three ultimate compression strengths: theoretical, numerical and experimental (average).

Table 4.9. Theoretical, numerical and experimental values of f_{ck}.

	Theory	Numerical simulation	Experimental test
f_{ck} [MPa]	30	31.63	27.77

In this case it can be noted that the experimental ultimate strength is closer to the theoretical value. The reason why this value is lower than in the previous case is that the confinement stress due to the friction between the concrete and the machine is much higher for the cubic specimens, which are squat, while the cylindrical ones, slimmer, are less subjected to this lateral stress; this results in a lower strength.
In some cases the experimental tests performed on the cylindrical specimens provided an ultimate compression strength lower than the minimum guaranteed value; the reason could have been a micro-damage suffered during the coring procedure.

The experimental values reported in Tables 4.7 and 4.9 are the average strengths achieved from these tests. The norms establish that in the design phases the concrete strength to be considered should be evaluated by means of a criterion which takes into account the data dispersion. The concrete strength according to this criterion is calculated as [11]

$$R_{ck} = R_{cm} - k \cdot S \tag{4.8}$$

where R_{cm} is the average value achieved from N tests and S is the mean square deviation:

$$R_{cm} = \frac{\sum_{i=1}^{N} R_{ci}}{N} \tag{4.9}$$

$$S = \sqrt{\frac{\sum_{i=1}^{N} (R_{ci} - R_{cm})^2}{N - 1}} \tag{4.10}$$

The norms define k=1.645 for a sufficiently high number of tests (N≥30).

5. Experimental-numerical correlation of full-scale tests

In this chapter, three full-scale experimental tests and their results will be firstly presented; afterwards, the development of the correspondent numerical models and their calibration procedure will be explained.

5.1. Experimental tests results

Two posts, characterized by different shapes and anchor bolts, have been subjected to push tests; the first post to be tested is identified by the code C125, while the second one is identified by HEA120.
A further test has been performed, which consists of a contemporary axial traction of two anchor bolts glued into a drilled concrete slab.

5.1.1. Experimental tests results: post C125

As indicated by the code, this post has a section characterized by a C shape, 125 mm width; others geometric parameters are hidden for confidentiality issues.

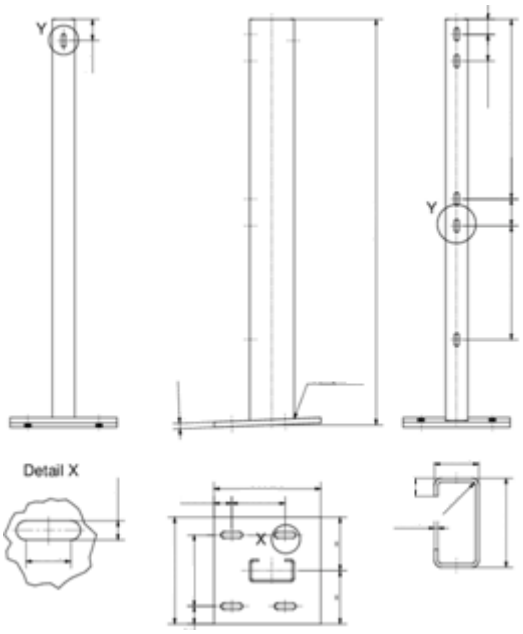

Figure 5.1. Technical drawing of the post C125.

It is constrained to the concrete slab by means of four anchor bolts M18 belonging to the class 8.8. The torque applied to them is 50 Nm.
The post is made of a steel S235, while the slab is made of a concrete belonging to the class C30/37. The slab surface has been painted in order to make the cracks more visible.
Four tests have been performed on this post, three pushing from an height of 1000 mm and one from 500 mm.

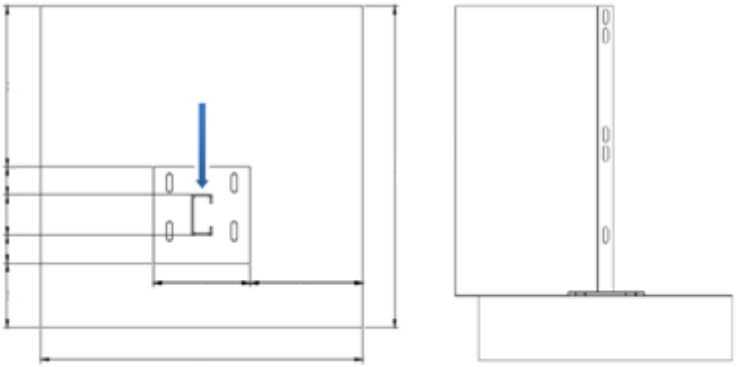

Figure 5.2. Graphical representation of push test on the post C125.

The measuring instrumentation utilized is the following:

- 1 force transducer placed on the pushing machine.
- 1 displacement transducer placed on the pushing machine.
- 4 force transducers, one placed on each anchor bolt.

The force transducers have a capacity of 75 kN and a maximum linear error of 0.25%.
The frequency of data acquisition is 10 Hz; an initial setting to zero of those transducers was required.

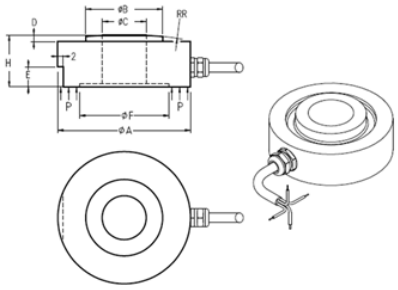

Figure 5.3. Technical drawing of the force transducers.

The concrete slab has been constrained to the soil in order to avoid displacements or lifts during the test. The machine has been placed in front of the slab and likewise constrained to avoid movements during the test.
The post has been pushed by means of a system characterized by an horizontal pin, whose height may change during the movement; it supports a plate which lays on the post. Thanks to such a system, the post deformation is in no way limited; it will be noticed in fact that the post section is completely free to rotate around each axis, maintaining approximately its C shape.
The front side of the plate is slightly lifted, event which can be observed in all the four tests.

Figure 5.4. Post C125 and pushing system.

Test 1

Here are the graphics which show the trend of the forces on the four anchors bolts and of the force imposed by the machine as a function of the applied displacement.

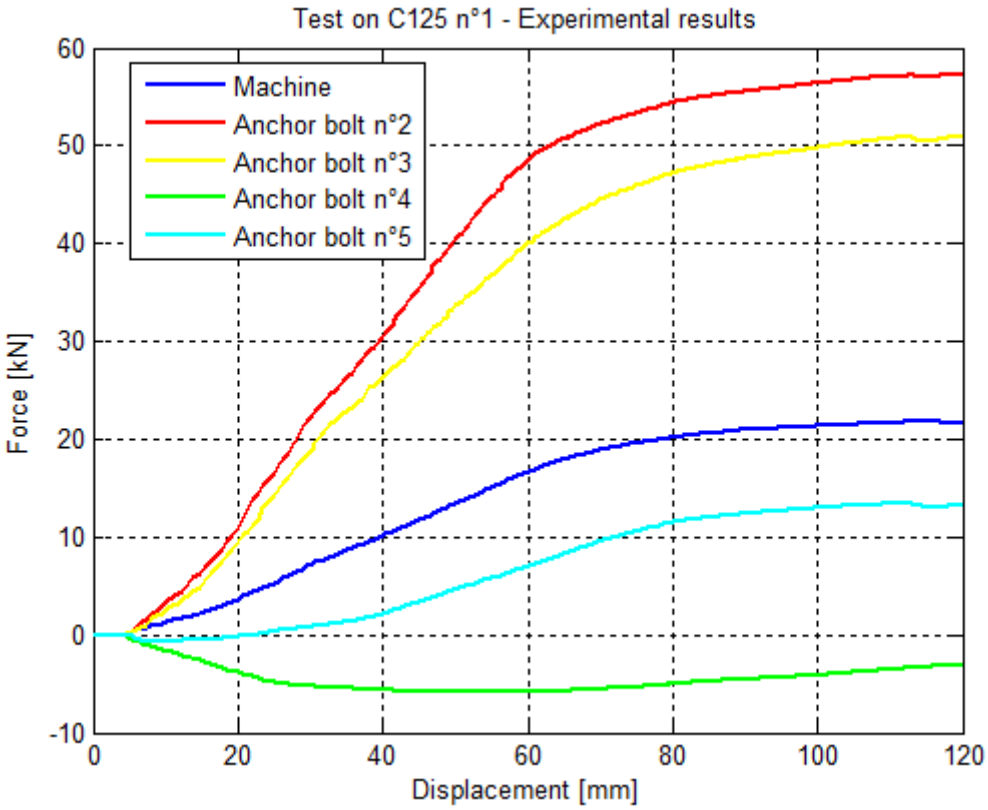

Figure 5.5. Experimental results of the test n°1 on the post C125: force imposed by the pushing machine and axial forces acting on the anchor bolts.

It is possible to notice the initial null forces, simply due to the initial distance between the pushing system and the post.
The difference between the forces measured by the transducers n°4 and n°5, placed behind the post with respect to the pushing machine, can be justified by the fact that the transducer n°4 is placed next to the open side of the post, which is subjected to a lower load. The same can be said about the anchor bolts n°2 and n°3, which show to be differently solicited.

Test 2

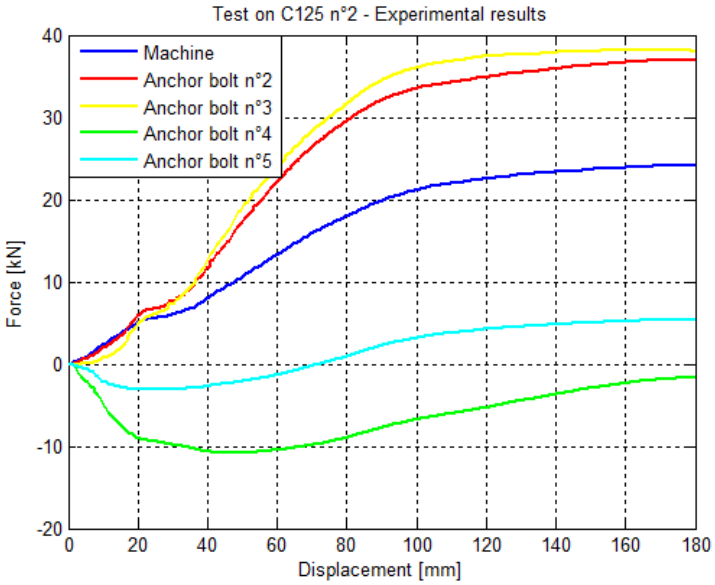

Figure 5.6. Experimental results of the test n°2 on the post C125: force imposed by the pushing machine and axial forces acting on the anchor bolts.

Test 3

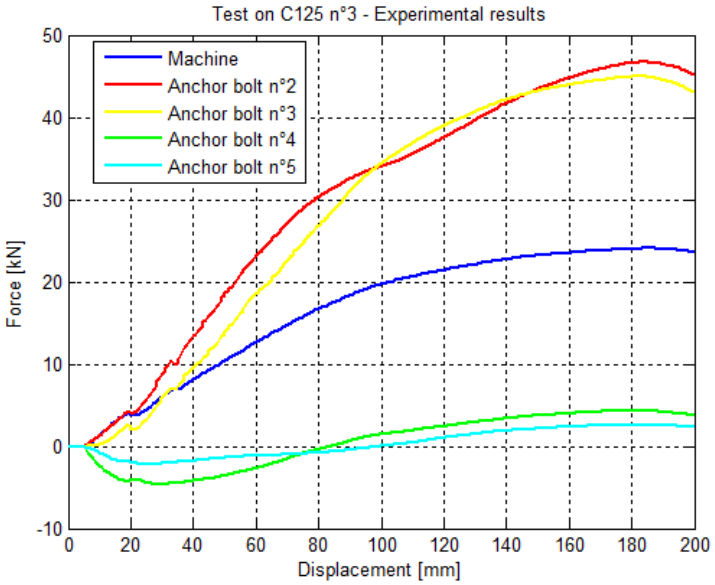

Figure 5.7. Experimental results of the test n°3 on the post C125: force imposed by the pushing machine and axial forces acting on the anchor bolts.

Test 4

In this last test the thrust has been applied form a height of 500 mm, starting from the top surface of the concrete slab. What is expected is a higher level of the force imposed by the machine, due to the shorter lever arm.
Regarding the reaction forces acting on the anchor bolts, it is important to notice that they are lower than what they were in the previous cases. This is due to the fact that the lower pushing height causes the shear contribute to become more significant, while in the previous tests the axial load was definitely dominant.

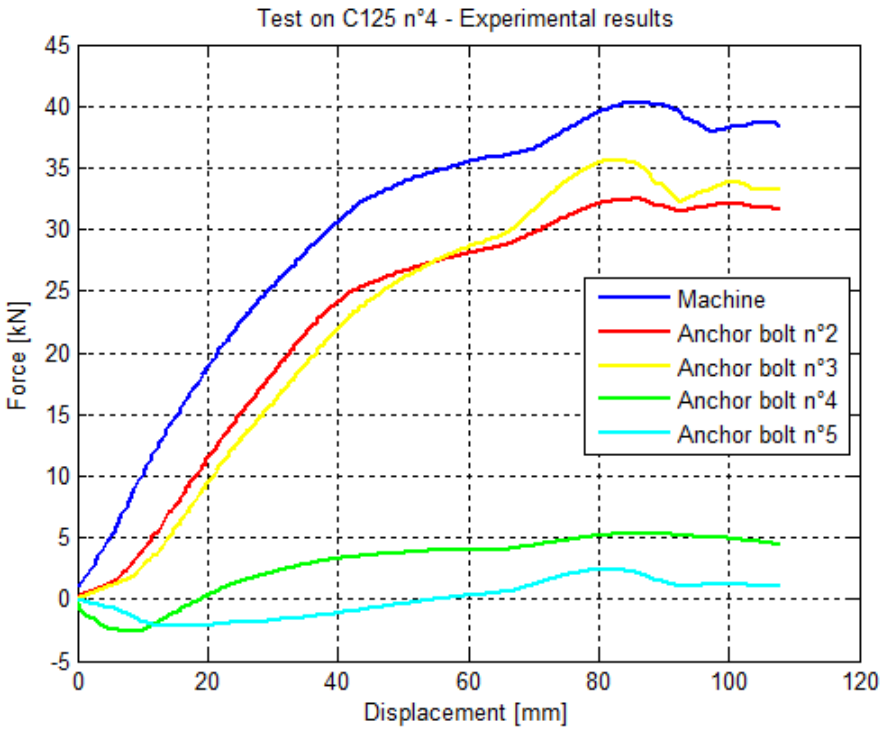

Figure 5.8. Experimental results of the test n°4 on the post C125: force imposed by the pushing machine and axial forces acting on the anchor bolts.

Failure mode

In all the four performed tests it has been observed that neither the concrete failure nor the bonding resin failure occurs. The concrete slab surface does not suffer cracking and the interface between the anchor bolts and the surrounding concrete remain perfectly joined.

No signs of damages appear on the anchor bolts; on the other hand, some washers suffer a slight deformation.
In all these four tests the post failure occurs with a rotation of the section.

Figure 5.9. Failure mode of the post C125.

Remarks

It must be take in consideration that the washer behavior should be investigated more accurately. In these tests certainly the influence of the transducers placed on the anchor bolts is relevant. In fact, since the contact surface with the plate is definitely larger than the washers, the behavior of the plate is altered.
The possible improvements which can be developed concerning these tests are:

- Study the influence of the transducers on the plate behavior.
- Study the washer behavior and deformation.

- Perform at least five tests in order to check the data dispersion and achieve a more representative correlation.
- Carry some modifications to the way of constraining the machine and the concrete slab, with the goal of eliminate unwanted displacements.

5.1.2. Experimental tests results: post HEA120

As indicated by the code, this post has a H section, 120 mm width.
Different types of anchor bolts have been used to constrain the plate to the concrete slab: two tests have been performed on a post anchored by means of four M14 8.8 and two tests using four M18 8.8.
The materials are again a steel S235 for the post and a concrete C30/37 for the slab.
The four posts have been pushed from a height of 1000 mm, starting from the concrete slab top surface.

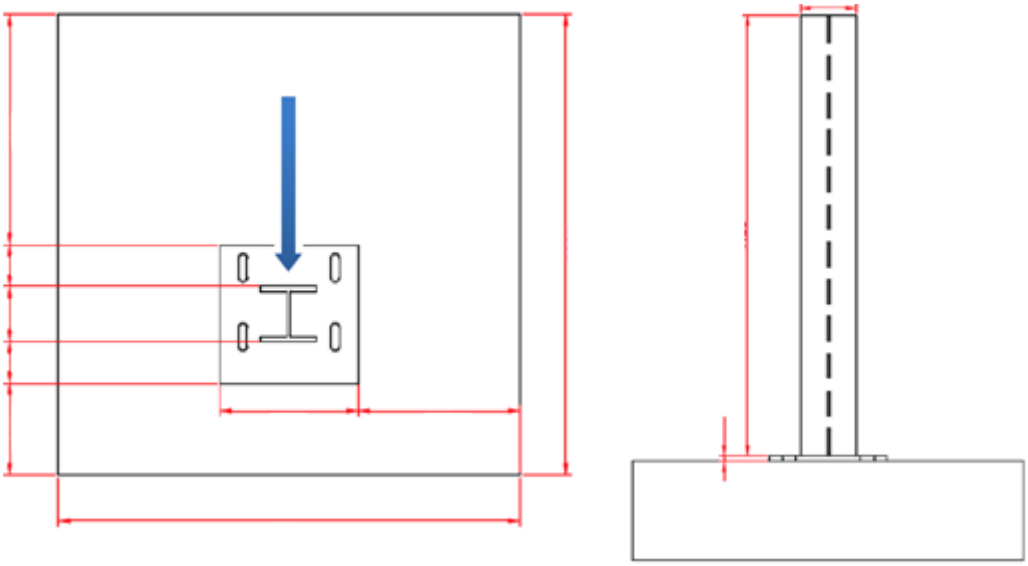

Figure 5.10. Graphical representation of push test on the post HEA120.

The same measurement instrumentation used for the C125 has been applied to this post. Only the forces on the four anchor bolts were available, because of a problem occurred to the measurement system placed on the machine.

Figure 5.11. Force transducers placed on the anchor bolts of the post HEA120.

The concrete slab has been constrained to the soil in order to avoid displacements or lifts during the test. The machine has been placed in front of the slab and likewise constrained to avoid movements during the test.

This post has been pushed by means of a system similar to the one used for the post C125, but unlike the previous case, the horizontal pin supports a plate which is bolted to a flange. Hence, the section cannot rotate around the post axis and the post movement is symmetric with respect to a vertical plane parallel to the pushing direction.

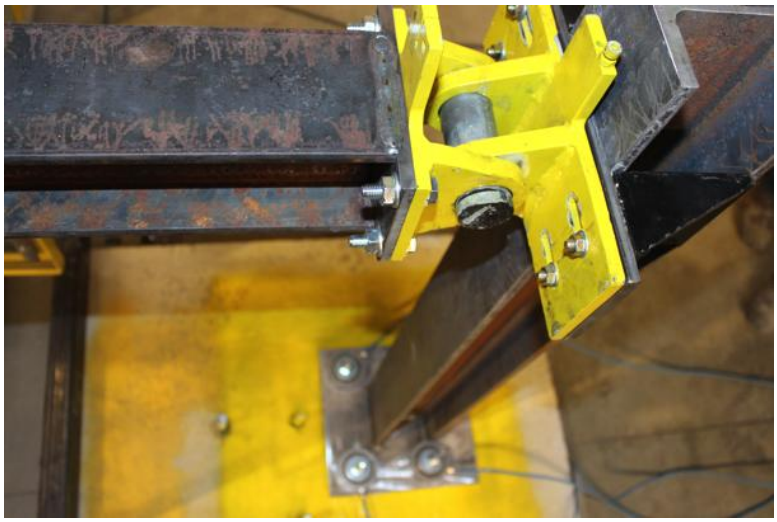

Figure 5.12. Post HEA120 and pushing system.

Test 1

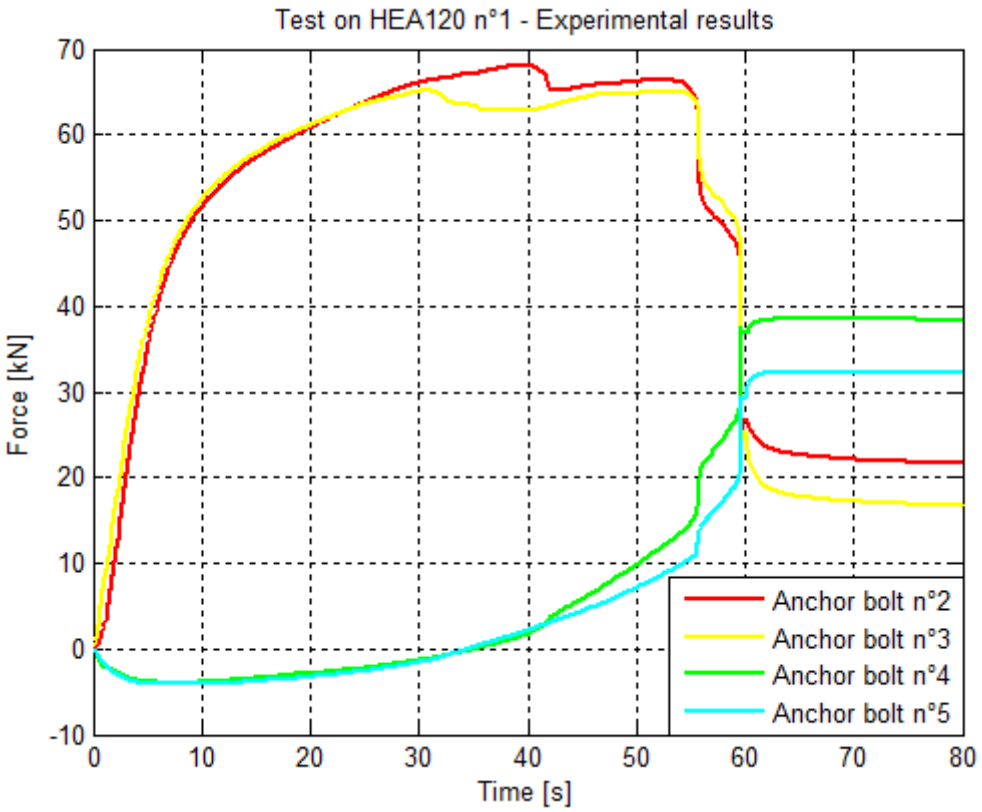

Figure 5.13. Experimental results of the test n°1 on the post HEA120: axial forces acting on the anchor bolts.

Unlike the previous cases, these tests are characterized by the concrete rupture, which always occurs in the area near the front anchor bolts (n°2 and n°3). This phenomenon is highlighted in the graphic through an irregular trend of the curves, more evident as far as concerns the bolts n°2 and the n°3. It starts at t = 30-35 sec, when the concrete begins to crack, and continues with undulations of the curve, until 60 sec, which is the instant when a significant part of concrete breaks. After that, the rupture continues and the anchor bolts return to work.

Test 2

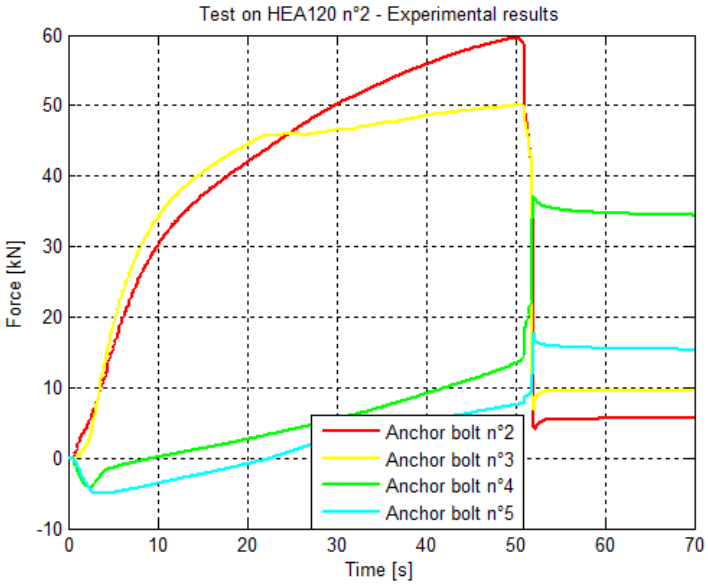

Figure 5.14. Experimental results of the test n°2 on the post HEA120: axial forces acting on the anchor bolts.

Test 3

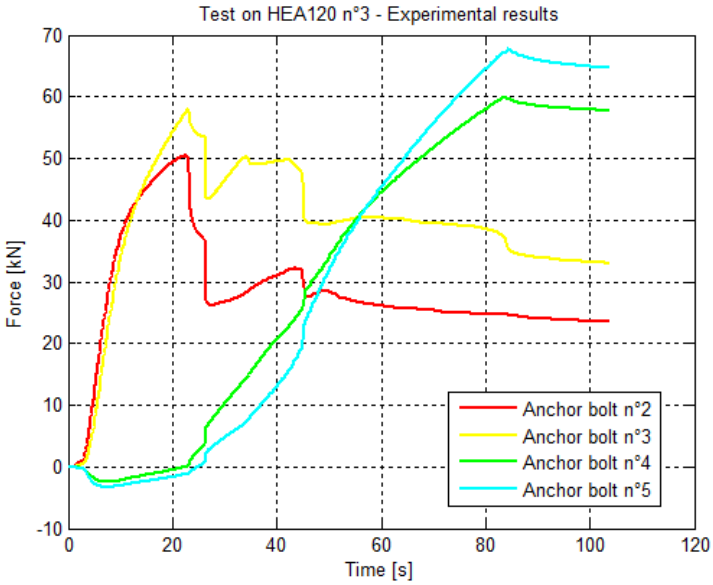

Figure 5.15. Experimental results of the test n°3 on the post HEA120: axial forces acting on the anchor bolts.

Test 4

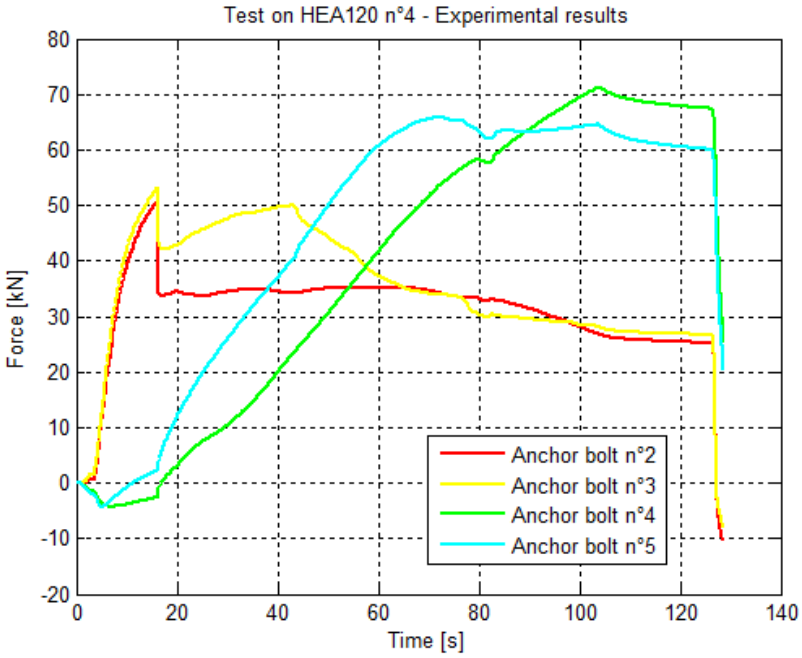

Figure 5.16. Experimental results of the test n°4 on the post HEA120: axial forces acting on the anchor bolts.

In these last two tests the machine has been stopped in order to avoid to damage the transducers n°4 and n°5, whose admitted limit load is almost reached.
The results of these tests are relatively consistent, with values and curves shape quite similar to each other.
In the second test the graphic shows a more relevant difference between the load on the anchors, especially between n°2 e n°3. This can be justified by the rotation of the plate, due to a non-simultaneous failure of the concrete in the areas around the rear anchorages, which causes a higher load on the anchor bolt n°2.

Failure mode

In all the four tests on HEA120 the concrete failure has been observed. The failure occurs in the areas around the front anchor bolts (n°2 and n°3), which are located on the pushing side and more solicited.

Figure 5.17. Failure mode of the post HEA120.

The appearance of cracks happens approximately in the same way in all the four tests. It can be observed that firstly the cracks originate near the front side of the plate and then a more violent rupture occurs very quickly and fissure the concrete slab along a line which extends between the two rear anchors and that continues slightly backward over the lateral sides of the plate.
It has been found out that the concrete damage extends approximately for a length comprised between 50% and 70% of the slab thickness.
Table 5.1 shows the depth of the cones formed around the anchor bolts.

Table 5.1. Depth of the cones formed around the anchor bolts.

	Anchor bolt n°2	**Anchor bolt n°3**	**Anchor bolt n°4**	**Anchor bolt n°5**
Test 1	45 mm	35 mm	-	-
Test 2	50 mm	30 mm	-	-
Test 3	25 mm	45 mm	-	-
Test 4	25 mm	40 mm	-	-

Remarks

Since the anchor bolts have been placed close to some already existent holes, the cracks orientation in the concrete might have been influenced by their presence.
As well as what happened in the previous case, the transducers area, which is much larger than the washers, may influence the behavior of all the components.
The possible improvements which can be developed concerning these tests are:

- Study the influence of the transducers on the plate behavior.
- Make use of new concrete slabs.

- Perform at least five tests in order to check the data dispersion and achieve a more representative correlation.
- Carry some modifications to the way of constraining the machine and the concrete slab, with the goal of eliminate unwanted displacements.
- See if a roller could turn out to be more appropriate as pushing system, since it could leave the post completely free to deform.

5.1.3. Experimental tests results: anchor bolts M18 8.8

Three traction tests on two anchor bolts have been eventually performed. In these tests, two anchor bolts M18 8.8, glued into a drilled concrete slab, have been concurrently pulled in the axial direction by means of the system shown in Figure 5.18.

Figure 5.18. Traction test on two anchor bolts.

The slab is made of a concrete belonging to the resistance class C30/37.
A transducer has been applied to the machine in order to measure the pulling force during these tests. No information about the displacements was available.

The anchors have been bolted to a bar placed horizontally on the concrete slab surface, in turn welded to a vertical bar which transmits the axial load. A torque has been applied to avoid any possible backlash.
Three pull tests, whose results are shown in Figure 5.19, have been performed.

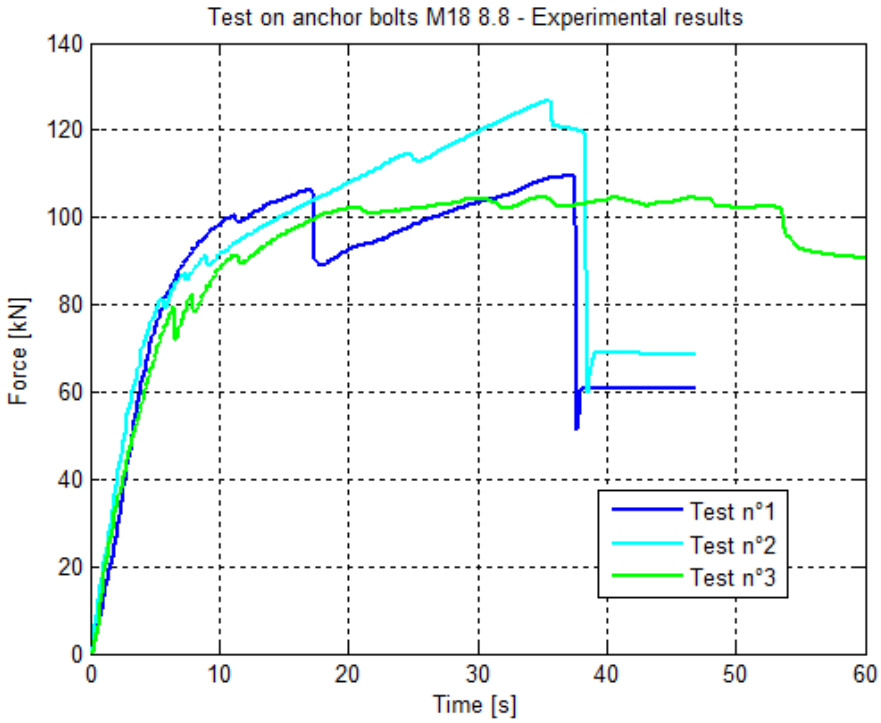

Figure 5.19. Experimental results of the tests on the anchor bolts: axial force imposed by the machine.

It can be observed that the three curves show a relatively similar slope until the force of 80 kN, when the concrete slab begins to crack. From this point the curves are characterized by slight fluctuations with mild variation of load, followed by stabilization.
In the tests n°1 and n°2 a sudden fragile rupture occurs, in both cases at about t=40 s, with a bursting of the concrete.
The third test differs because of the fact that the curve is almost flat and a bursting of the concrete doesn't happen. Instead, a less fragile rupture occurs. This can be due to the fact that the non-simultaneous failure of the concrete around the anchors causes a deformation of the support.

Failure mode

It has been noticed that this system shows a quite similar behavior in all the three cases: after an initial progressive increase of the load on both the anchors, the concrete begins to crack and one of the anchors fails shortly before the other. The fact that the anchor bolts fail one at a time is probably due to these reasons:

- An installation depth which differs for a few tenths of a millimeter.
- A slightly different quantity of bonding resin.
- Air bubbles in the concrete.
- A combination of these phenomena.

As previously explained, the failure mode consists of an initial cracking followed by a sudden fragile bursting of the concrete in the areas around the holes. Neither the bolts nor the bonding resin have been damaged. It can be seen that no vertical displacements of the bolts have occurred and that the thread shape in the concrete has remained untouched, which means that the bonding resin kept on working for the whole time of the tests.

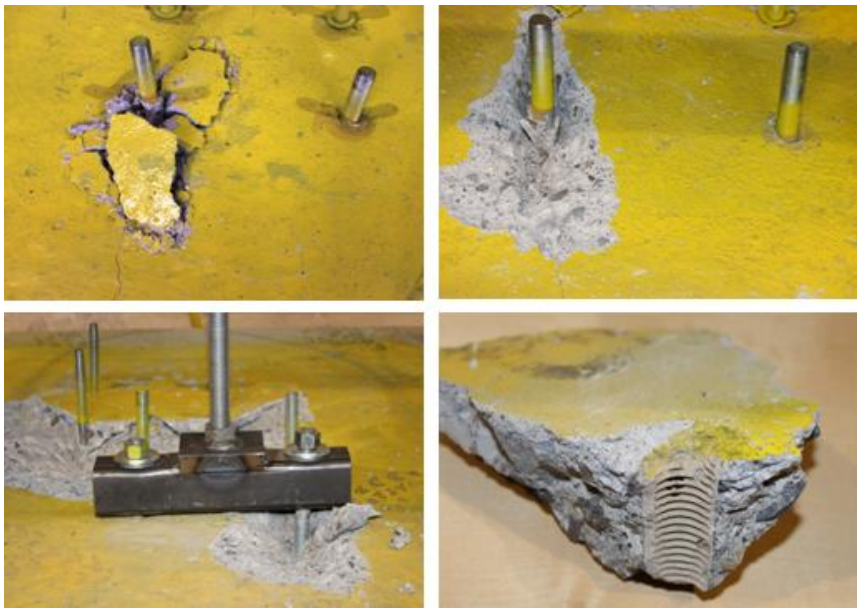

Figure 5.20. Failure mode of the anchor bolts.

Remarks

The anchor bolts have been already utilized for the tests on the posts C125, therefore they could have suffered micro-cracking. Moreover, each concrete slab has previously been used in other tests, thus, although the pull tests on the anchor bolts have been performed in non-cracked areas, the state of the concrete was uncertain.
The possible improvements which can be developed concerning these tests are:

- Make use of new concrete slabs.
- Perform the tests using deeper slabs and perhaps try to figure out if the slab depth influences the cracking mode.
- Perform tests on one single anchor bolt.
- Achieve a better control of the depth and of the quantity of resin.
- Perform tests on other anchor bolts (different lengths, types of resin, diameters, types of bolts,…).

5.2. Numerical models

The numerical models of the three systems above described have been developed by means of the software LS-Dyna®.
In order to have accurate data about the materials, the best approach would have been to cut a piece of each post, from the central part of them, since it is the largest and the less thick. Then, from those pieces, two standard specimens would have been cut and used to perform standard traction tests in order to achieve the σ-ε curves of the actual materials which the two posts are made of.
Since it has not been possible to cut the posts, an already existent σ-ε curve of the steel S235 has been used. Three σ-ε curves were available: minimum, average and maximum. Several tests have been performed to choose which among these curves is the most suitable to reproduce the posts actual behavior.

The numerical models have been developed exploiting the features described in Paragraph 2.2: the *CONTACT_TIED_SURFACE_TO_SURFACE_FAILURE, to model the interaction between the anchors bolts and the surrounding concrete considering the possible failure of the link between these two parts, and the introduction of the bolts preload through an imposed lowering of temperature.

Since information about the tensile and the shear stresses at failure of the bonding resin utilized was not available, they have been approximately calculated from the experimental tests performed on the two anchor bolts M18 8.8.
From these tests, in fact, whereas the bonding failure doesn't occur, it is possible to assert that the resin endures the load at least until F = 120 kN. Assuming that this load is equally distributed on the two anchor bolts, each of them is subjected to an axial force of 60 kN; this means, considering that the radius of the bolts core is r = 7.466 mm, that the axial stress acting on the bolts is approximately

$$\sigma = \frac{F/2}{\pi \cdot r^2} = 343 \frac{N}{mm^2} \tag{5.1}$$

Hence, since it is known that the bonding resin withstands at least until this value of stress, it has been assumed as input parameter in the models.

5.2.1. Numerical model: post C125

The numerical model of the post C125 is shown in Figure 5.21.

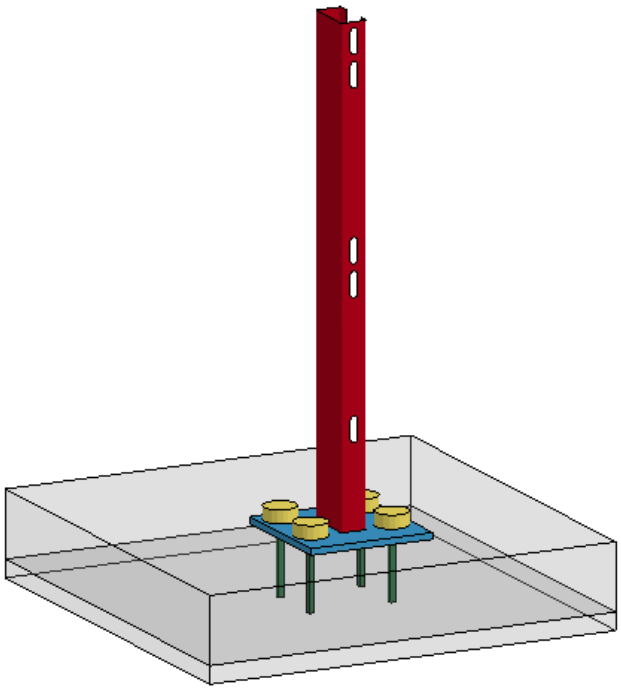

Figure 5.21. Post C125 numerical model.

Materials

The post has been modeled using shell elements. It is welded to a plate which is drilled in four points, where the anchor bolts are placed. The plate has been modeled using solid elements.
These elements are made of the steel S235, which has been reproduced in LS-Dyna® through the card *MAT_PIECEWISE_LINEAR_PLASTICITY.
This material allows the user to introduce the σ-ε curve corresponding to the plastic range, besides the density, the Young's modulus, the Poisson's ratio and several others parameters. The σ-ε average curve has been chosen to represent the plastic range.
The welding constraint between the post and the plate has been imposed by merging the nodes on the base of the post to a set of suitably placed nodes belonging to the plate.
The anchoring system consists of four bolts M18 belonging to the steel class 8.8. Even this material has been represented by means of the LS-Dyna® feature *MAT_PIECEWISE_LINEAR_PLASTICITY. Since the whole σ-ε curve of this material was not available, a bilinear behavior has been chosen for it. The needed values have been achieved from the information about the steel class:

- Density: $\rho = 7.8 \cdot 10^{-9}$ ton/mm^3
- Young's modulus: $E = 2.1 \cdot 10^5$ N/mm^2
- Poisson's ratio: $\upsilon = 0.3$
- Yield stress: $\sigma_y = 640$ N/mm^2
- Rupture stress: $\sigma_r = 800$ N/mm^2
- Rupture strain: $\varepsilon_r = 0.12$

This material has been used both for the shank and the head of the bolts. As previously discussed, in the experimental tests four transducers have been placed on the anchor bolts and since they are much wider than the washers, they greatly influence the behavior of the plate and the post. In order to consider this influence, the head of the bolts has been modeled as a squat cylinder with the actual dimensions of the transducers.
Both the head and the shank of the anchor bolts have been modeled through solid elements. An alternative choice to model the shanks could be using beam elements. It would have been simpler from the computational side but unsuitable to the type of contact which has been chosen to represent the bonding between the bolts and the concrete.

The head and the shank of the bolts are constrained to each other by means of merged nodes.
Regarding the concrete, it has been represented in LS-Dyna® by means of the feature *MAT_CSCM_CONCRETE.
Since the concrete class is C30/37, the input parameter f'_c has been set to 30 N/mm^2; the default maximum aggregates size (Dagg) has been chosen, as the actual value was unknown.

Boundary conditions and constraints

The pushing system has been realized by means of a beam and a plate, as shown in Figure 5.22.

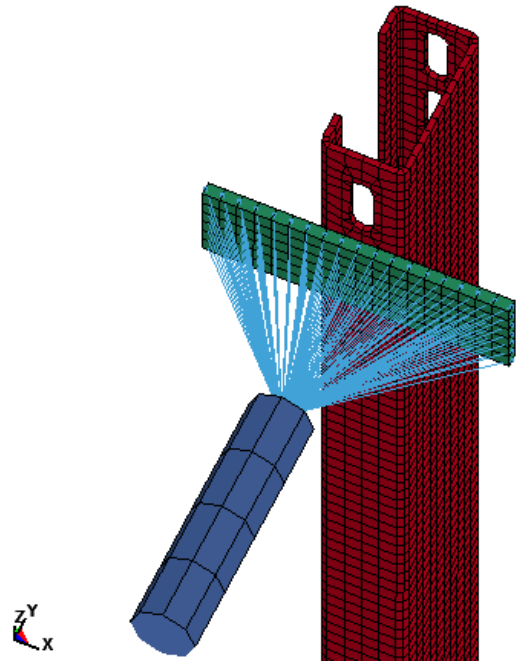

Figure 5.22. Modeling of the pushing system for the test on post C125.

In order to correctly represent the interaction between the pushing system and the post, a special joint has been imposed between the beam and the plate, by means of the LS-Dyna® feature *CONSTRAINED_JOINT_SPHERICAL, which requires as input parameters the identification numbers of two coincident nodes. Each of these nodes must belong to a different rigid body; in this way,

the two concerned rigid bodies can rotate respect to one another, around the coincident nodes.
Therefore, two rigid bodies have been defined, through the card *CONSTRAINED_NODAL_RIGID_BODY. The first includes all the nodes of the plate plus one of the two coincident nodes of the spherical joint (rigid body A in Figure 5.23); the second (rigid body B in Figure 5.23) includes the two extreme nodes of the last element of the beam (one of them is the second node belonging to the spherical joint).

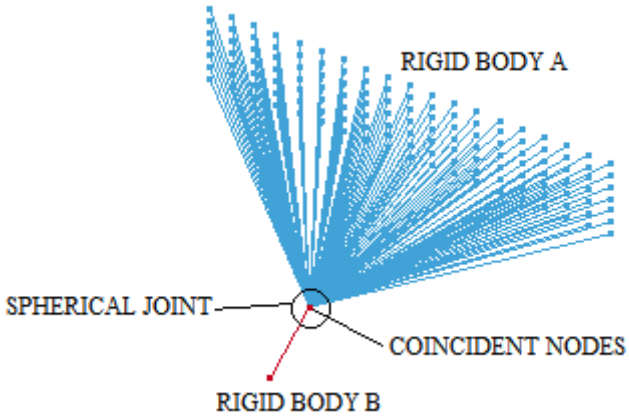

Figure 5.23. Detailed view of the pushing system for the test on post C125.

Thanks to such a system, no momentum is transmitted between the pushing system and the post. Moreover, thanks to the plate, which just leans on the post without constraining it, the section of the post is completely free to rotate around each axis.
Eventually, to correctly represent the horizontal pin, not all the rotations and displacements have been let free: through the card *SPC_NODE, applied to the node belonging to the rigid body A placed on the spherical joint, the displacement along the axis x and the rotations around the axes y and z have been constrained. In this way, the concerned node, hence the whole plate, is free to move only along the axes y and z and to rotate only around the axis x, which is what happens in the reality.
On the opposite side of the beam, a parabolic displacement, which goes until 150 mm, has been imposed by means of the card *BOUNDARY_PRESCRIBED_MOTION_NODE.

The beam is free to move along the axial and the vertical directions, as it was in the experimental tests; this has been achieved through a *BOUNDARY_SPC_SET, which constrains all the movements of the beam nodes, but the axial and the vertical displacements.
The model is constrained to the ground by means of another *BOUNDARY_SPC_SET, applied to the nodes on the bottom surface of the concrete slab; all the displacements and rotations of these nodes are hindered.

Contacts

As previously told, the interaction between the anchor bolts and the surrounding concrete has been modeled by means of the LS-Dyna® feature named *CONTACT_TIED_SURFACE_TO_SURFACE_FAILURE. The stress values at failure have been set to 343 N/mm^2, as explained at the beginning of the Paragraph 5.2.
A second type of contact was necessary in the model, the *CONTACT_AUTOMATIC_SINGLE_SURFACE. This contact prevents the interpenetration of the parts to each other.
Since the holes in the plate are wider than the anchor bolts, push the post would have made the plate slip on the concrete surface; in order to avoid it, friction has been imposed. This has been done by setting the parameter FS in the card *CONTACT_AUTOMATIC_SINGLE_SURFACE, which is the static coefficient of friction, whose value for the contact between steel and concrete is $\mu = 0.6$.
It has been seen that without the friction the plate slips on the concrete, but with the friction it does not.

Preload

As explained in Paragraph 2.2, the preload acting on the shanks, due to the torque applied, has been imposed exploiting the thermal contraction typical of the metals. The idea is to shrink the bolts by cooling them. As bolts contract during this phase, preload is induced. The temperature variation ΔT (or the coefficient of thermal expansion α) to produce a target stress σ_{pr} can be estimated as

$$\sigma_{pr} = E \cdot \alpha \cdot \Delta T \qquad (5.2)$$

where E is the Young's modulus.
The stress σ_{pr} due to the imposed torque, whose value is T = 50 Nm, can be calculated as follows:

$$\sigma_{pr} = \sqrt{\sigma^2 + 3 \cdot \tau^2} \tag{5.3}$$

τ is the shear stress acting on the shank, which can be achieved by

$$\tau = \frac{T \cdot d}{2 \cdot J} \tag{5.4}$$

where T is the torque, d is the diameter of the core and J is the moment of inertia of the section, whose value is calculated as

$$J = \frac{\pi \cdot r^4}{2} \tag{5.5}$$

where r is the radius of the core.

σ is the axial stress acting on the shank; it can be obtained as

$$\sigma = \frac{F}{A_{res}} \tag{5.6}$$

where A_{res} is the area of the resistant section and F is the value of the axial force acting on the shank. The value of F can be calculated from the applied torque knowing the characteristics of the thread, as follows:

$$F = \frac{T}{r \cdot tg(\gamma + \beta)} \tag{5.7}$$

where r is the radius of the core, β is the angle of friction and γ is the angle of inclination of the thread. The values of β and γ can be estimated as follows:

$$\beta = \tan^{-1}(\mu) \tag{5.8}$$

$$\gamma = \tan^{-1}\left(\frac{p}{\pi \cdot d_n}\right) \tag{5.9}$$

where μ is the value of the static friction, while p and d_n are respectively the pitch and the nominal diameter of the thread; the nominal diameter and the diameter of the core are related by the following equation:

$$d = d_n - 2 \cdot h \tag{5.10}$$

where h is the height of the thread.

In this case, since the characteristics of the thread were not known, standard values have been utilized. It has been found that, for a bolt M18 (d_n = 18 mm), the pitch and the height of the thread and the area of the resistant section have the following values:

$$p = 2.5 \text{ mm}$$
$$h = 1.534 \text{ mm}$$
$$A_{res} = 192 \text{ mm}^2$$

The static coefficient of friction between steel and concrete is μ = 0.6. Hence:

$$\beta = \tan^{-1}(\mu) = 30.96° \tag{5.11}$$

$$\gamma = \tan^{-1}\left(\frac{p}{\pi \cdot d_n}\right) = 2.53° \tag{5.12}$$

$$r = \frac{d_n - 2 \cdot h}{2} = 7.466 \text{ mm} \tag{5.13}$$

$$F = \frac{T}{r \cdot tg(\gamma + \beta)} = 10121.94 \text{ N} \tag{5.14}$$

$$\sigma = \frac{F}{A_{res}} = 52.72 \frac{N}{mm^2} \tag{5.15}$$

$$J = \frac{\pi \cdot r^4}{2} = 4880.58 \text{ mm}^4 \tag{5.16}$$

$$d = 2 \cdot r = 14.932 \text{ mm} \tag{5.17}$$

$$\tau = \frac{T \cdot d}{2 \cdot J} = 76.49 \ \frac{N}{mm^2} \tag{5.18}$$

$$\sigma_{pr} = \sqrt{\sigma^2 + 3 \cdot \tau^2} = 142.59 \ \frac{N}{mm^2} \tag{5.19}$$

Since the boundary conditions strongly influence the stress distribution, equation (5.2) is not very suitable to predict the necessary temperature to impose the desired value of stress; therefore, several tests have been performed in order to figure out which is the correct value of ΔT that allows to obtain a stress of σ_{pr} = 142.59 N/mm^2.
The value of the coefficient of thermal expansion for the steel is $\alpha = 1.7 \cdot 10^{-5}$ K^{-1}.
After several tests, it has been found that the suitable value of the temperature variation is ΔT = -49.2 K.
As explained in Appendix A.3, in order to achieve the thermal contraction of the anchor bolts, these cards are required:

- *MAT_ADD_THERMAL_EXPANSION, to assign the coefficient of thermal expansion to the steel which the bolts are made of.
- *LOAD_THERMAL_LOAD_CURVE, to impose a thermal load to that material.
- *DEFINE_CURVE, to define two curves, one ramped from zero to T = -49.2 K and then constant, to prescribe the thermal load during the dynamic relaxation phase, and one constant, to maintain the thermal load during the transient phase.

Outputs

The purpose of this calibration procedure was principally to achieve the trend of the forces acting on the four anchor bolts and of the force imposed by the machine, as functions of the applied displacement.
In order to obtain the force applied by the machine, it has been required to plot the trend of the axial force vs. time acting on an element of the beam, chosen arbitrarily; this has been done by means of the card *DATABASE_HISTORY_BEAM.

To achieve information about the forces acting on the anchor bolts, four planes have been traced, through the card *DATABASE_CROSS_SECTION_PLANE. Those planes cross the bolts in correspondence of the transducers; each plane is related to an anchor bolt, which can be defined by means of the aforementioned card. In this way, the trend of the forces vs. time, acting on the point where the bolts cross the corresponding planes, is plotted by the software.
Therefore, five force vs. time graphics have been achieved; then, the values of the forces have been transferred in force vs. displacement graphics and compared with the experimental results.

5.2.2. Numerical model: post HEA120

The numerical model of the post HEA120 is shown in Figure 5.24.

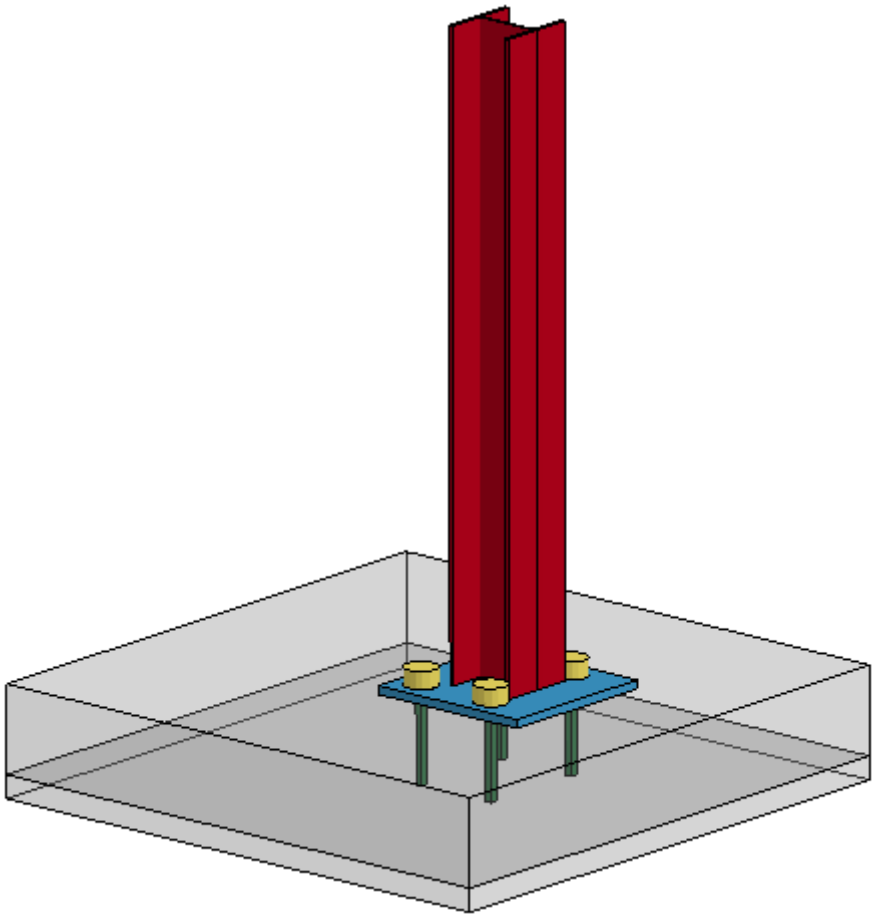

Figure 5.24. Post HEA120 numerical model.

Materials

This post has been modeled similarly to the previous one. Shell elements have been used for the post and solid elements for the plate, the concrete, the anchor bolts and the transducers.
The material is again the S235 for the post and the plate and a steel belonging to the class 8.8 for the anchor bolts; they both have been modeled by means of the feature *MAT_PIECEWISE_LINEAR_PLASTICITY. The minimum curve has been chosen for the material S235.
The feature *MAT_CSCM_CONCRETE has been used to model the concrete, with the input parameters f'_c = 30 N/mm^2 and Dagg = 19 mm.
An additional failure criterion based on the maximum pressure acting on the concrete has been added to the model, setting the value to 20 MPa; it has been introduced through the card *MAT_ADD_EROSION.

Boundary conditions and constraints

The pushing system is similar to the one used in the previous model; it is shown in Figure 5.25.

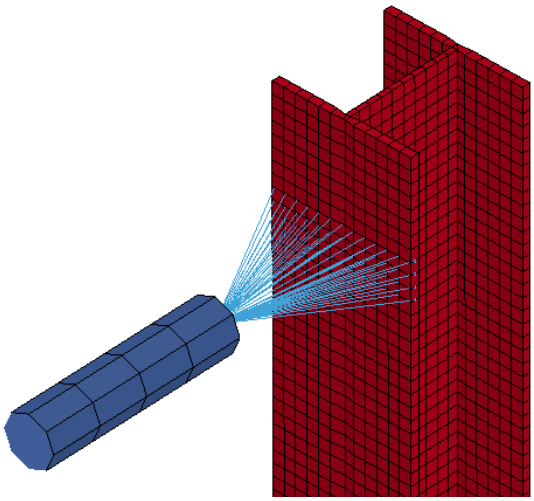

Figure 5.25. Modeling of the pushing system for the test on post HEA120.

The LS-Dyna® features *CONSTRAINED_JOINT_SPHERICAL, *CONSTRAINED_NODAL_RIGID_BODY and *SPC_NODE have been used to model the pushing system, in the same way explained for the post C125.

The only difference is that in this case one of the rigid bodies includes a group of nodes belonging to a flange of the post, avoiding the usage of a plate.
The plate was necessary in the previous model because the section of that post should be allowed to rotate during the movement; in this case, instead, the movement of the post is symmetric and the flange remains perpendicular to the pushing direction.
This system well reproduces the experimental test, in which the flange of the post is bolted to a plate, which can rotate only around an horizontal axis, and not around a vertical one.
On the opposite side of the beam, a parabolic displacement has been imposed by means of the card *BOUNDARY_PRESCRIBED_MOTION_NODE.
Like in the previous case, two *BOUNDARY_SPC_SET cards have been defined: the first to constrain all the movements of the beam nodes but the axial and the vertical displacements; the second to constrain the bottom surface of the concrete slab to the ground.

Contacts

The contacts used in this model are exactly the same which have been used in the previous one.
Hence, the interaction between the anchor bolts and the surrounding concrete has been modeled through the feature *CONTACT_TIED_SURFACE_TO_SURFACE_FAILURE. The stress values at failure have been set to 343 N/mm^2, as explained in Paragraph 5.2.
The *CONTACT_AUTOMATIC_SINGLE_SURFACE, with $\mu = 0.6$ (static coefficient of friction), has been used to avoid the interpenetration of the parts to each other.

Preload

Two models of the post HEA120 have been developed, which differ in the anchor bolts size; this means that the preload is also different.
The first model has anchor bolts M18 8.8, thus the preload value is exactly the same calculated for the post C125; it is achieved by imposing a temperature variation $\Delta T = -49.2$ K.
The second model has anchor bolts M14 8.8; the preload to apply has been achieved in the same way, of course with different parameters:

d_n = 14 mm
p = 2 mm
h = 1.227 mm
A_{res} = 115 mm^2

The static coefficient of friction between steel and concrete is μ = 0.6. Hence:

$$\beta = \tan^{-1}(\mu) = 30.96° \tag{5.20}$$

$$\gamma = \tan^{-1}\left(\frac{p}{\pi \cdot d_n}\right) = 2.60° \tag{5.21}$$

$$r = \frac{d_n - 2 \cdot h}{2} = 5.773 \text{ mm} \tag{5.22}$$

$$F = \frac{T}{r \cdot tg(\gamma + \beta)} = 13055.63 \text{ N} \tag{5.23}$$

$$\sigma = \frac{F}{A_{res}} = 113.53 \frac{N}{mm^2} \tag{5.24}$$

$$J = \frac{\pi \cdot r^4}{2} = 1744.72 \text{ mm}^4 \tag{5.25}$$

$$d = 2 \cdot r = 11.546 \text{ mm} \tag{5.26}$$

$$\tau = \frac{T \cdot d}{2 \cdot J} = 165.44 \frac{N}{mm^2} \tag{5.27}$$

$$\sigma_{pr} = \sqrt{\sigma^2 + 3 \cdot \tau^2} = 308.22 \frac{N}{mm^2} \tag{5.28}$$

The value of the coefficient of thermal expansion for the steel is $\alpha = 1.7 \cdot 10^{-5}$ K^{-1}. After several tests, it has been found that the suitable value of the temperature variation is ΔT = -94 K.

Outputs

The outputs required from this model are the forces acting on the anchor bolts; the force imposed by the machine has been calculated as well, but since the experimental values were not available it has not been compared.
The forces acting on the anchor bolts and on the beam used to push the post have been achieved by means of the cards *DATABASE_HISTORY_BEAM and *DATABASE_CROSS_SECTION_PLANE, as explained in Paragraph 5.2.1.

5.2.3. Numerical model: anchor bolts M18 8.8

The numerical reproduction of the test on the anchor bolts M18 8.8 is shown in Figure 5.26.

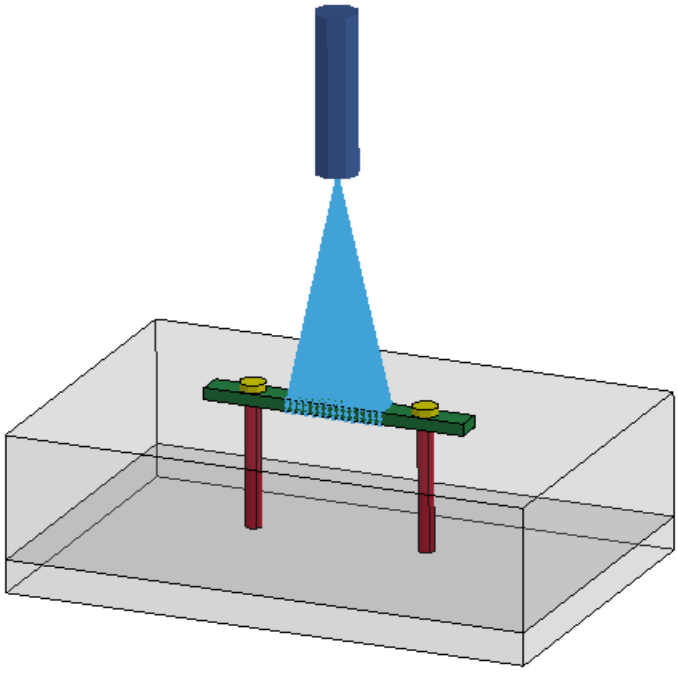

Figure 5.26. Modeling of the traction test on the anchor bolts.

With the exception of the beam used to pull the bolts, this model has been completely realized using solid elements.
The shanks, the nuts and the horizontal bar to which the anchors are bolted, have all been modeled through the *MAT_PIECEWISE_LINEAR_PLASTICITY,

using the bilinear model of the steel 8.8 for the shanks and the nuts and the steel S235 with the average σ-ε plastic curve for the bar.
The concrete has exactly the same characteristics of the one used for the post HEA120. Hence, it has been realized by means of the features *MAT_CSCM_CONCRETE and *MAT_ADD_EROSION, with the input parameters f'_c = 30 N/mm^2, Dagg = 19 mm and MXPRES = 19 N/mm^2. Even in this case the card *MAT_ADD_EROSION has been important in order to correctly model the concrete failure which occurs around the anchor bolts.
The pulling system is similar to the one used for the post HEA120, with the only exception that in this case it pulls the bar which the anchors are bolted to. One of the two rigid bodies includes a group of nodes belonging to that bar. The beam is free to move only in the vertical direction.
The concrete slab is constrained on the bottom surface.
Contacts and preload are modeled like it has been done in the previous cases. The preload stress to apply is σ_{pr} = 142.59 N/mm^2 and the temperature variation which allows to reach that stress is ΔT = -58 K.
The only output required in order to perform the experimental-numerical comparison is the axial force acting on the beam, achieved through the card *DATABASE_HISTORY_BEAM.

5.3. Calibration and results comparison

During the calibration process of these models, two features have been subjected to modifications in order to reach the best results:

- The σ-ε curve of the steel S235
- The pressure value corresponding to the concrete failure

The three σ-ε available curves of the steel S235 have been all tested and the best one has been chosen for each model; as guessed by the previous description of the numerical models, there is not a unique curve that fits to all the models. This means that the material which a post is made of may be characterized by an its own particular σ-ε curve, and that the post behavior is strongly dependent on the material curve used. Therefore, as previously told, the actual curve of the material should be achieved performing a standard traction test on a steel specimen directly taken from the tested post or one of the same batch.

The second parameter which has been calibrated is the pressure value in the card *MAT_ADD_EROSION. This card is important in the numerical models of the post HEA120 and of the anchor bolts M18 8.8, since in these two cases the concrete failure occurs.
The parameter MXPRES, in this card, establishes the value of pressure acting on a concrete element, at which the element must be considered broken and be deleted.
This card provides many failure criteria among which the user can choose, based for instance on the principal stresses, or the shear strain, or the volumetric strain, etc.; many criteria have been tested and the one based on the maximum pressure turned out to be the most suitable to represent the concrete damage in these models.
Several tests have been performed varying the parameter MXPRES, in order to make the concrete rupture happen at the desired level of the imposed force.

The following figures show a comparison between the failure modes and the forces trends in the two cases, experimental and numerical.

5.3.1. Experimental-numerical results comparison: post C125

During the calibration of this model the concrete has not been modified, since its rupture does not occur in the experimental tests and didn't occur in the numerical one either, since the first trial.
What have been subjected to modification are the post material and the pushing system.
The three available σ-ε curves of the steel S235 have been all tried in the model and the average one turned out to be the best.
The pushing system has been at first modeled by means of a plate characterized by a C shape, as it actually is, but since it has been noted that the lateral flanges hindered the free movement of the post, generating a forces peak corresponding to the moment at which the post leaned against them, they have been removed, and a simple flat plate has been used, as shown in Figure 5.22.

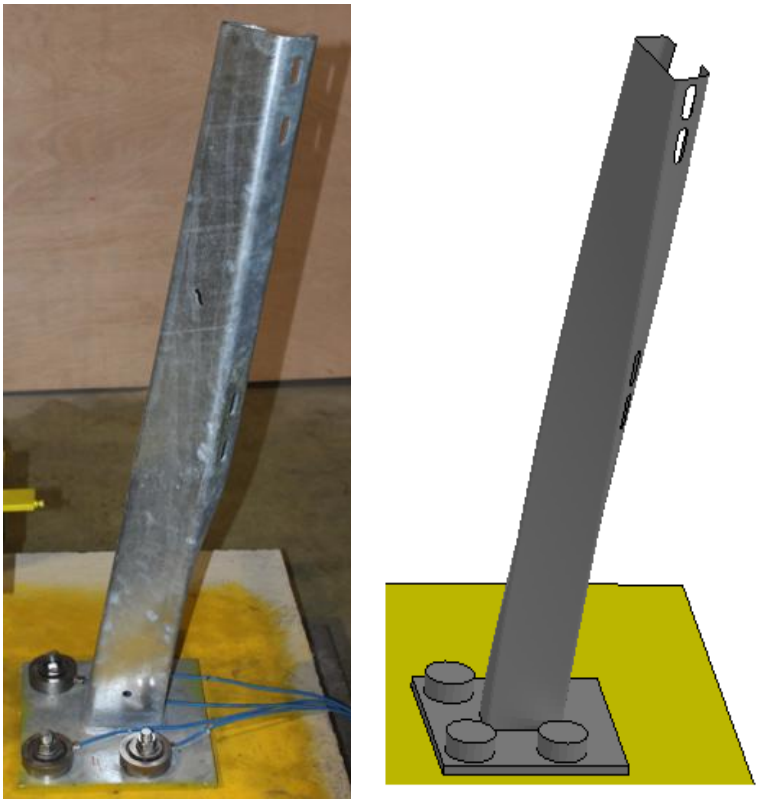

Figure 5.27. Experimental-numerical comparison of the failure mode of the post C125.

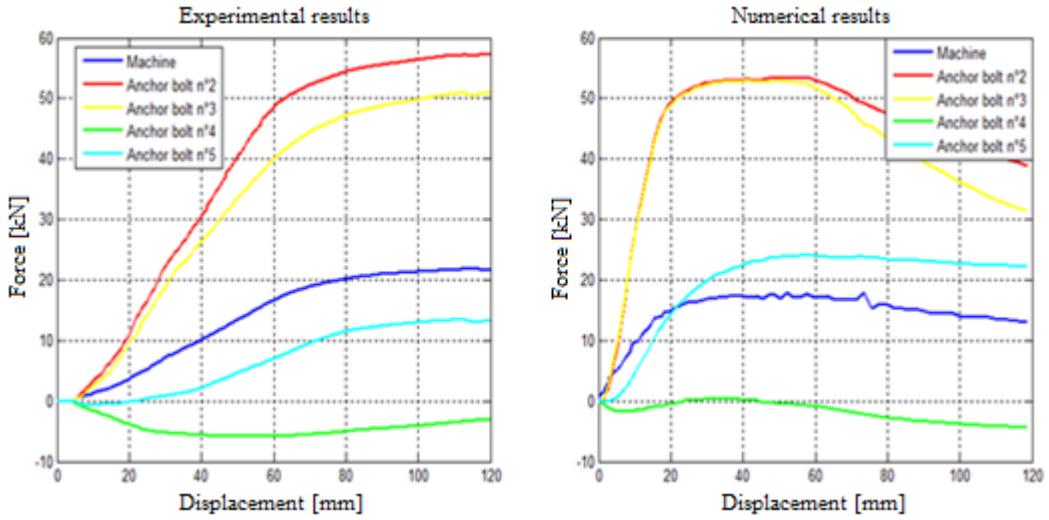

Figure 5.28. Experimental-numerical comparison of the forces measured during the test on the post C125: force imposed by the machine and axial forces acting on the anchor bolts.

5.3.2. Experimental-numerical results comparison: post HEA120

Even the calibration of this model has been made modifying the post material, hence varying the σ-ε curve in the card *DEFINE_CURVE, which allows to introduce the plastic field of the material, and the value of the yield stress, required in the card *MAT_PIECEWISE_LINEAR_PLASTICITY.
Plus, the card *MAT_ADD_EROSION has been modified many times in order to achieve the concrete failure and to make it occur in the desired way and at the right level of forces.
Many parameters present in that card have been tested and MXPRES turned out to be the best to achieve those two goals concurrently.
Figure 5.29 compares the rupture as it occurred during the experimental tests with the numerical model, in which the blue elements are the ones eroded.

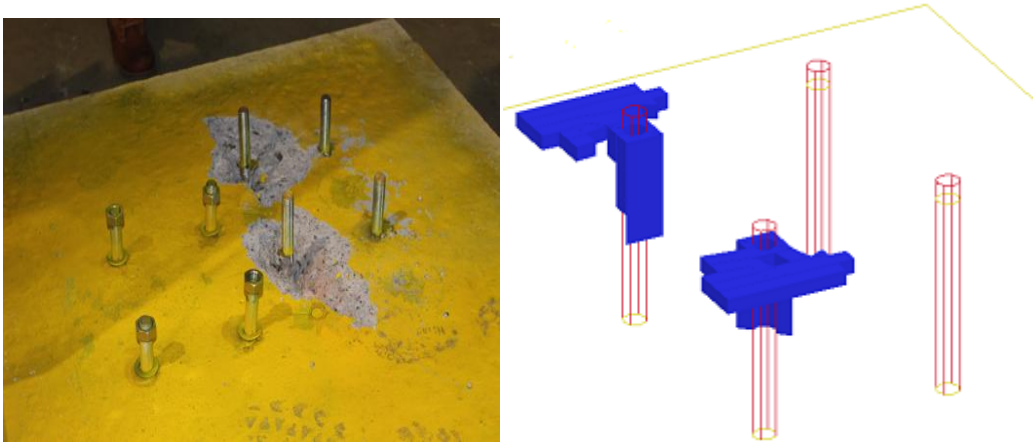

Figure 5.29. Experimental-numerical comparison of the failure mode of the post HEA120.

The graphics in Figure 5.30 show instead the experimental-numerical comparison of the forces acting on the anchor bolts during the tests.

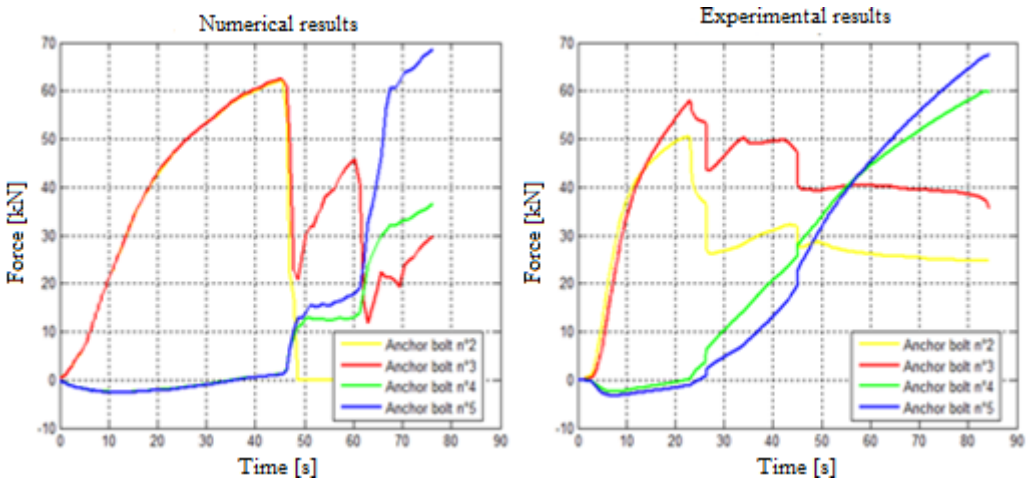

Figure 5.30. Experimental-numerical comparison of the forces measured during the test on the post HEA120: axial forces acting on the anchor bolts.

5.3.3. Experimental-numerical results comparison: anchor bolts M18 8.8

The calibration of this model has been principally made by modifying the concrete erosion way.

Several tests have been performed in order to make the concrete rupture occur in correspondence of an imposed force of about 120 kN.

It is possible to see that in the experimental tests there is a residual strength whose value is comprised between 60 and 70 kN. The choice of the right erosion value has been made considering this aspect, as well.

Moreover, it has been noted that the material which the bar is made of strongly influence the behavior of the entire system. Thus, since it was known that the bar is made of a steel S235, the three σ-ε curves have been tried and the average one provided the best results.

Figure 5.31 compares the rupture as it occurred during the experimental tests with the numerical model, in which the blue elements are the ones eroded.

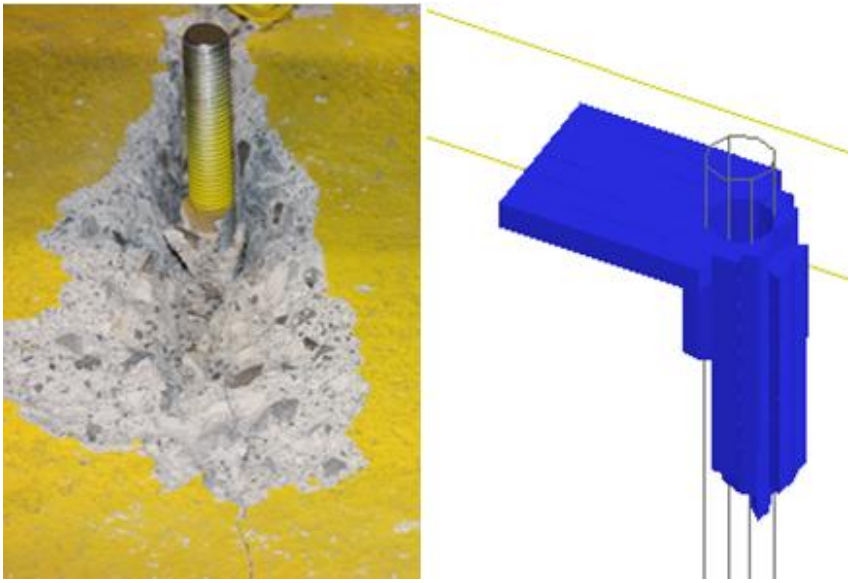

Figure 5.31. Experimental-numerical comparison of the failure mode of the anchor bolts.

The graphic in Figure 5.32 compares the trend of the force achieved from the numerical model with the ones obtained during the first two experimental tests, since the third one is not much comparable.

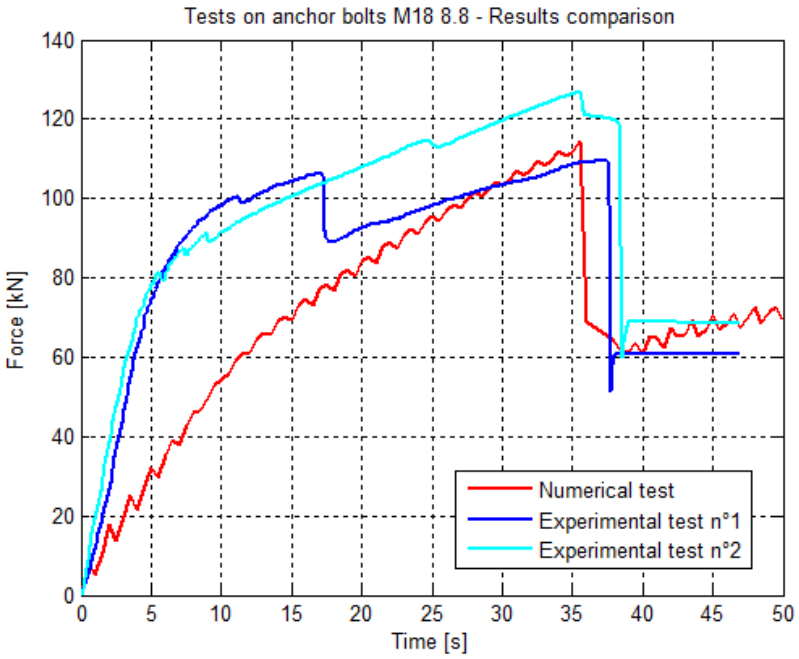

Figure 5.32. Experimental-numerical comparison of the forces measured during the test on the anchor bolts: axial force imposed by the machine.

6. Full-scale crash tests on a commercial bridge safety barrier

The last part of this work consists of the fulfillment of two full-scale crash test simulations, performed on a commercial bridge safety barrier, already built and tested.
Firstly, a general overview regarding road safety barriers, particularly focused on bridge safety barriers, will be presented; the parameters defined by the standards and commonly computed during a crash test will be introduced in the first paragraph.
Afterwards, the barrier numerical model developed during this work will be described.
Lastly, the crash tests numerical results achieved will be shown and compared with the experimental ones.

6.1. Road safety barriers general features

Road safety barriers can be divided in three main categories:

- Metallic barriers (guardrails)
- Concrete barriers (New Jersey)
- Wood and steel made barriers

Figures 6.1, 6.2 and 6.3 show these three types of barrier. The first one is the most commonly used on bridges.

Figure 6.1. Example of metallic barrier.

Figure 6.2. Example of concrete barrier.

Figure 6.3. Example of wood and steel made barrier.

Since metallic barriers are the most utilized on bridges and whereas the crash tests have been performed on a barrier belonging to this category, the attention will be here focused on them.

The main components of a metallic barrier are [17]:

- Principal rail: a longitudinal element which has the function of acting like a belt and create a containment line for the errant vehicles and redirect them back to the carriageway. Thanks to its capability to deform, it can absorb a great quantity of the vehicle kinetic energy during the impact; when the vehicle impacts against it, its deformation results in a homogeneous distribution of the stresses on the posts, which afterwards transmit to the ground the forces generated during the impact. If correctly designed, its axis must remain at the same height with respect to the ground during the impact. Several shapes and configuration are available, depending on its use.

- Posts: beams placed perpendicularly to the ground or slightly inclined with respect to it; their main function is to support the rails and to transmit to the ground the forces that they receive from an impacting vehicle. They may be characterized by different geometries; the most common section shapes are C and H. The choose about the distance between the posts is a designer task and may vary depending on the barrier type.
- Spacers: elements placed between the posts and the rails, with the function of increase the quantity of absorbed energy through the large deformation which they are subjected to during an impact. The shapes could be very different to each other, depending on barrier destination and design.
- Bolted connections: their function is to create a link between posts and spacers and between spacers and rails; in some cases the bolts can be substituted by a welded connection. The bolting is a very difficult element to design, since it must satisfy different requests. It must be able to guarantee a resistant link between two parts, but it should be even able to permit the main function of the rail, that is create a continuous containment belt for the errant vehicle; this means that over a certain level of the post flexion, the bolts must break and permit the detachment of the post from the rail, in order to prevent the post to drag the rail down, since it would cause the overcoming of the barrier by the vehicle.
  Figure 6.4 show the correct and the wrong behaviors of a road safety barrier. In the example on the left, the posts subjected to a too high flexion detach from the rail, that can rightly accomplish its task; in the example on the right, the concerned bolts don't break and the posts drag down the rail, which is then overcame by the vehicle.

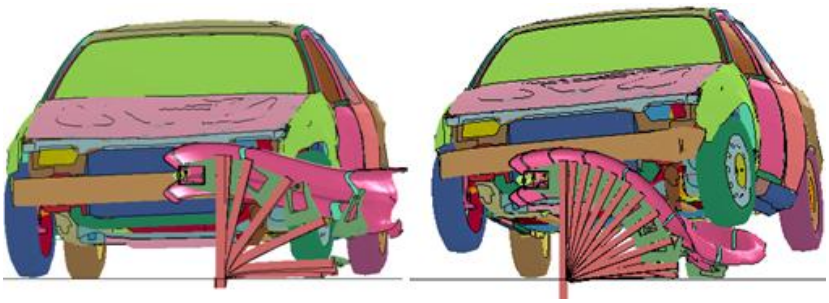

Figure 6.4. Examples of correct and wrong behaviors of a road safety barrier [17].

The components here described characterize all the metallic road safety barriers, but there may be several further elements which can be added; the barriers, in fact, may strongly differ to each other, depending on their purposes and destinations.

Bridge safety barriers differ from the ones commonly placed along the roadsides because of the particular technique with which they are installed on the structure of the bridge.
Usually, the common safety barriers are installed along the roadsides embedding a certain length of the posts into the soil, as shown in Figure 6.5. This solution does not require any further particular anchoring system.

Figure 6.5. Installation technique of a common road safety barrier.

On the other hand, the safety barriers designed to be installed along the sides of a bridge, need a particular auxiliary structure like the one shown in Figure 6.6.

Figure 6.6. Installation technique of a bridge safety barrier.

The concerned structure is a concrete curb, whose function is to encompass the anchor bolts used to constrain the barrier to the bridge. The curb dimensions are therefore related to the anchor bolts length. Usually the curb height is 4/3 of the bolts length, but this is only a common assumption and not a standard. Define the correct dimensions of the curb or, more commonly, the correct length of the bolts to be placed into an existent curb, is a designer task.

Frequently, in fact, designers face the issue of installing barriers on bridges whose curbs are different with respect to the ones used during the experimental crash tests performed.
In those cases, the barrier behavior is not supported by any experimental evidence.
It is therefore necessary to understand if it is possible to install a bridge safety barrier on a curb whose height is different from the one of the curb utilized during the experimental tests accomplished on that barrier.
In order to verify the device correct functioning, when used in the actual operating conditions, the best solution is constituted by the numerical simulations.

Road safety barriers should be able to satisfy the following aims [18], verified by means of numerical simulations and certified through crash tests performed by authorized laboratories:

- Barrier structural adequacy, without components detachment.
- Vehicle containment, without overturning or overcoming.
- Safety of vehicle occupants.
- No penetration of the vehicle by any component of the barrier.
- Detour angle less than 1/3 of the impact angle.
- Total transverse displacement of the barrier to be evaluated according to its destination.

Numerical simulations consist of the calculation of the dynamics of the mechanical system constituted by the vehicle, the barrier, the road, possibly the curb, including all the possible interactions, deformations and breakages.
A good calculation must be able to adequately consider:

- Vehicle dynamics before, during and after the collision.
- Suspensions deformation or breakage during and after the collision.
- Interaction between the tires and the pavement, the curb and all the parts of the barrier.
- Deformations of all the parts of the barrier.
- Possibility of bolts failure.
- Inelastic behaviors and failures.
- All the possible contacts.
- Inertia of all the moving parts.

This can only be achieved through the usage of very detailed models, as close to the physical reality as possible. Typically finite elements or multi-body models are used.
Crash tests, instead, are real scale trials, whose implementation is defined in Italy by the Ministerial Decree 223/92 and in Europe by the European technical regulations EN 1317.
The standard [19] provides the indications about the vehicles to be utilized to perform the crash tests.

Table 6.1. Vehicles weight indications for a crash test.

	Car	Car	Car	Rigid Truck	Bus	Rigid Truck	Rigid Truck	Articulated Truck
Vehicle [kg]	825 ± 40	1300 ± 65	1500 ± 75	10000 ± 300	13000 ± 400	16000 ± 500	30000 ± 900	38000 ± 1100
Max ballast included [kg]	100	160	180					
Dummy [kg]	75							
Test total mass [kg]	900 ± 40	1300 ± 65	1500 ± 75	10000 ± 300	13000 ± 400	16000 ± 500	30000 ± 900	38000 ± 1100

The standard establishes also the measurement instrumentation which must be installed inside and outside the vehicle during the crash tests.

Figure 6.7. Example of crash test.

Safety barriers have to sustain impacts of different types of vehicle (from cars to trucks) under different impact conditions regarding the vehicle velocity, the impact angle and the state of the road. In case of a lower-weight vehicle (car) impact, the restraint system should possess the ability to deform, so that the kinetic energy of the impact is absorbed mostly by the barrier and vehicle deformations. This significantly reduces deceleration levels experienced by vehicle occupants and increases their safety.

However, in a case of higher-weight vehicles (truck, bus) impact, the system should contain and redirect the vehicle back on the road without complete failure of the main longitudinal elements of the system.

Thus, safety barrier design is a compromise between its deformability (stiffness) and its strength.

According to the standard EN 1317, road safety barriers have to fulfill the following criteria [2], [17], [18]:

- Level of containment (L_c): it represents the vehicle kinetic energy, calculated considering the velocity component perpendicular to the barrier; the standard defines four major classes of containment levels, which are further subdivided.

$$L_c = \frac{1}{2} \cdot M \cdot (V \cdot \sin \theta)^2 \tag{6.1}$$

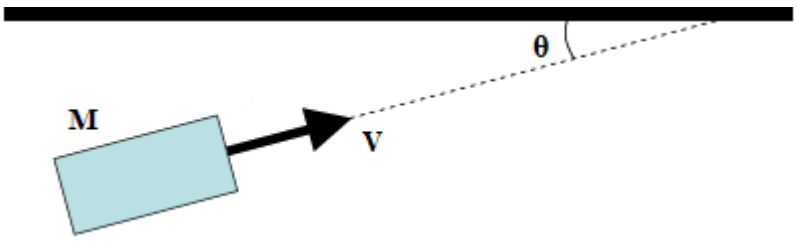

Figure 6.8. Explanatory scheme of the calculation of the level of containment.

M is the vehicle mass, V is the vehicle velocity upon impact and θ is the impact angle.

According to the level of containment, road safety barriers are classified as shown in Table 6.2.

Table 6.2. Levels of containment and acceptance tests.

Barrier class	L_c [kJ]	Acceptance tests
T1	6	TB21
T2	21	TB22
T3	37	TB41 – TB21
N1	44	TB31
N2	82	TB32 – TB11
H1	127	TB42 – TB11
H2	288	TB51 – TB11
H3	463	TB61 – TB11
H4a	572	TB71 – TB11
H4b	724	TB81 – TB11
L1	127	TB42 – TB32 – TB11
L2	288	TB51 – TB32 – TB11
L3	463	TB61 – TB32 – TB11
L4a	572	TB71 – TB32 – TB11
L4b	724	TB81 – TB32 – TB11

The classes identified by L have been recently introduced; the barriers belonging to the classes L differ from the ones belonging to the classes H because they passed even the test TB32; the reason why this test has been introduced in the European standard is that some barriers, even if able to withstand high energies, showed unexpected behaviors if subjected to intermediate energies.
The levels of containment are verified by means of crash tests, utilizing different vehicles, as indicated in Table 6.3.

Table 6.3. Characteristics of the acceptance tests.

European code	Vehicle	Mass [ton]	Velocity [km/h]	Impact angle [°]
TB11	Car	0.9	100	20
TB21	Car	1.3	80	8
TB22	Car	1.3	80	15
TB31	Car	1.5	80	20
TB32	Car	1.5	110	20
TB41	Rigid truck	10	70	8
TB42	Rigid truck	10	70	15
TB51	Bus	13	70	20
TB61	Rigid truck	16	80	20
TB71	Rigid truck	30	65	20
TB81	Articulated truck	38	65	20

- Impact severity: it is a measure of the impact consequences for the vehicle occupants. The most important measure utilized is the ASI (Acceleration Severity Index). ASI is a measure of vehicle accelerations during the impact, which is evaluated over a moving interval of 50 ms and normalized with allowable accelerations in the three longitudinal vehicle axes. If maximum ASI exceeds the admitted values, then it is considered that the impact consequences for the passengers are dangerous or even lethal.
  The index ASI has been subjected to several debates in the field of the international technical regulations; in fact, it showed some difficulties, both in the accelerations data acquisition, since the on-board instrumentation is delicate and very sensitive to the different possible positions, and in the interpretation of those data, since a complex event like the impact of a vehicle is simplified into a single parameter. For this reasons, the technical standard EN 1317 completes the evaluation of the impact severity by considering further additional parameters. Therefore, the parameters utilized in order to evaluate the impact severity are:

  - ASI – Acceleration severity index

$$\mathrm{ASI} = \sqrt{\left(\frac{a_x}{\hat{a}_x}\right)^2 + \left(\frac{a_y}{\hat{a}_y}\right)^2 + \left(\frac{a_z}{\hat{a}_z}\right)^2} \qquad (6.2)$$

    a_x, a_y and a_z are the average (evaluated on an interval of 0.05 s) values of the longitudinal, transversal and vertical components of the vehicle acceleration, measured on its center of gravity.
    $\hat{a}_x$, $\hat{a}_y$ and $\hat{a}_z$ are the limit accelerations, interpreted as the values below which the risk of damages for the occupants is very low (at worst slight injuries); for occupants who wear the safety belts their values are:

    $\hat{a}_x$ = 12 g
    $\hat{a}_y$ = 9 g
    $\hat{a}_z$ = 10 g

    ASI is determined, for all the barriers except the ones belonging to the class N1, by means of a crash test TB11.

  - THIV – Theoretical Head Impact Velocity

$$\mathrm{THIV} = \sqrt{v_x(t)^2 + v_y(t)^2} \qquad (6.3)$$

The concept of Theoretical Head Impact Velocity has been developed in order to evaluate the impact severity on the vehicle occupant; the occupant, in particular his head, is considered as an object which moves freely and, when the vehicle changes its velocity during the impact, the occupant head keeps on moving until it hit an internal surface of the vehicle. It is assumed that the head remains in contact with that surface during the rest of the impact.
v_x and v_y are the components of the head velocity related to the local coordinate system of the vehicle. THIV must be less than 33 km/h.

- PHD – Post-impact Head Deceleration

$$PHD = \sqrt{a_x(t)^2 + a_y(t)^2} \tag{6.4}$$

This parameter describes the head deceleration after an impact and must be less than 20 g. It has been recently eliminated because considered too strongly dependent on the type of vehicle.

These parameters are used to define three levels of the impact severity, reported in Table 6.4.

Table 6.4. Impact severity levels.

Impact severity level	Indexes		
	ASI	**THIV**	**PHD**
A	≤ 1.0	≤ 33 km/h	≤ 20 g
B	≤ 1.4	≤ 33 km/h	≤ 20 g
C	≤ 1.9	≤ 33 km/h	≤ 20 g

- Deformation of the barrier, quantified by three parameters:

  - The Working Width (W), which is the distance between the side of the guardrail facing the traffic before the impact and the maximum lateral position of any major part of the barrier during the impact; if a point of the vehicle overcomes the barrier, so that the barrier cannot be considered in the measurement of the working width, it must be used alternatively the maximum lateral position of any part of the vehicle.
    This parameter allows the designers to choose which type of barrier to install in a particular point, according to the available space on the side of the road.

- The Dynamic Deflection (D), which is the maximum lateral dynamic displacement of the face of the restraint system nearest to the traffic during impact.
- Vehicle Intrusion (VI), which is the vehicle maximum dynamic lateral displacement from the side of the guardrail facing the traffic before the impact. It is evaluated by means of pictures and high-speed videos taken during the impact. No more than one wheel can overcome the barrier.

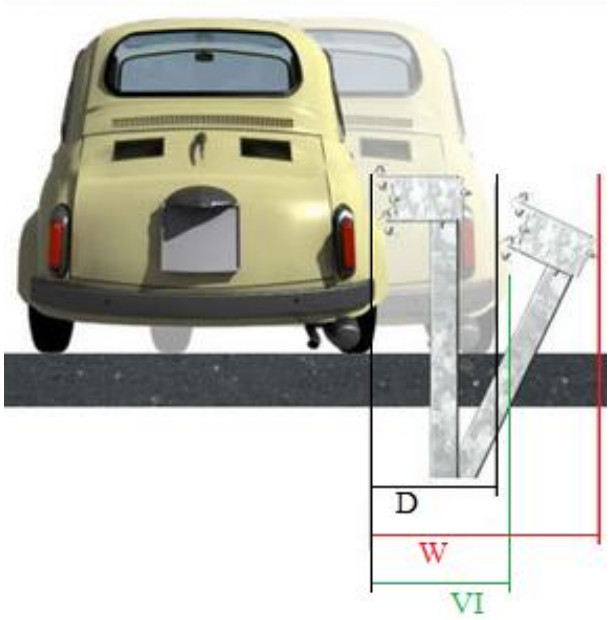

Figure 6.9. Explanatory scheme of the parameters Working Width, Dynamic Deflection and Vehicle Intrusion.

According to the Working Width and the Vehicle Intrusion, the classes listed respectively in Tables 6.5 and 6.6 are defined.

Table 6.5. Barriers classification according to the Working Width.

Class	Working width [m]
W1	$W \leq 0.6$
W2	$W \leq 0.8$
W3	$W \leq 1.0$
W4	$W \leq 1.3$
W5	$W \leq 1.7$
W6	$W \leq 2.1$
W7	$W \leq 2.5$
W8	$W \leq 3.5$

Table 6.6. Barriers classification according to the Vehicle Intrusion.

Class	Vehicle intrusion [m]
VI1	VI ≤ 0.6
VI2	VI ≤ 0.8
VI3	VI ≤ 1.0
VI4	VI ≤ 1.3
VI5	VI ≤ 1.7
VI6	VI ≤ 2.1
VI7	VI ≤ 2.5
VI8	VI ≤ 3.5
VI9	VI > 3.5

These values are important during the design phase, since it is always necessary to guarantee a suitable space behind the barrier, in order to allow it to deform correctly. A limited deformation of the barrier with respect to what it is supposed to be may result in a not correct absorption of energy and consequent severe damages to the vehicle occupants.

The technical legislation does not define precisely the criteria which must be utilized in the selection of a barrier. It only provides a summary that indicates the minimum containment class which has to be considered in different cases. This summary takes in account:

- The road type
- The traffic type
- The general purpose of the barrier

Table 6.7. Minimum containment class for road safety barriers.

Road type	Traffic type	Barrier purpose		
		Traffic island	Lateral edge	Bridge side
Motorways and main suburban roads	I II III	H2 H3 H3 – H4	H1 H2 H2 – H3	H2 H3 H3 – H4
Secondary suburban roads and urban fast roads	I II III	H1 H2 H2	N2 H1 H2	H2 H2 H3
Neighborhood roads and local roads	I II III	N2 H1 H1	N1 N2 H1	H2 H2 H2

The meaning of the traffic typology codes is:

- Traffic typology I: DAT ≤ 1000 or DAT > 1000 + heavy vehicles ≤ 5%
- Traffic typology II: DAT > 1000 + heavy vehicles > 5% and ≤ 15%
- Traffic typology III: DAT > 1000 + heavy vehicles >15%

where DAT is the daily average traffic. DAT corresponds to 1/365 of the annual traffic, which is calculated through a standard procedure, measuring the traffic during certain hours on 16 specific days of the year (2 Saturdays, 2 Sundays, 1 Monday, 1 Friday and 2 midweek days both during the winter period and the summer period). A vehicle is identified as "heavy" when its mass is equal or more than 3.5 tons.

In summary, a road safety barrier must absolve concurrently these three tasks:

- Absorb part of the impact energy transmitted by the vehicle.
- Limit the impact effects on the vehicle occupants.
- Properly redirect the errant vehicle along a certain direction so as to prevent it to become a danger for other incoming vehicles.

This targets are always very difficult to be reached simultaneously. The standards provide indication about the type of barrier which is required for a certain road, according to the traffic characteristics; this should result in the barrier capability of restrain the heaviest vehicles which travel along the concerned road, but the accidents involving that type of vehicles are much less than the ones involving lightweight vehicles.
According to a study [20] performed about 25000 accidents occurred along the Italian motorways, many extremely resistant barriers are very often bumped by cars (80% of the cases), and just rarely by heavy vehicles; thus, the occupants of the cars may be seriously injured because of the high robustness of the barrier itself, which may cause too elevated decelerations; human brain is permanently injured if subjected to a deceleration superior to 80 g for more than 3 ms, while heart and lungs cannot withstand a deceleration higher than 60 g.
This study showed that the 50% of the accidents are characterized by an energy lower than 26.35 kJ, and the 90% by an energy lower than 254.62 kJ; this means that a barrier belonging to the class H2, hence able to withstand 288 kJ, would be resistant enough for the Italian highways.

Most of the barriers used in Italy are instead characterized by too high containment energies, since they have been developed according to old regulations. Even if the current standards require much lower energies, there are still many barriers whose containment energy is 2-3 times higher with respect to the barriers used in the rest of the world. Those barriers may withstands impact energies higher than the ones generated by an actual accident, but this results in more serious potential damages to people.
Regardless of the road and the traffic, a barrier should be as more resistant as more harmful are the consequences arising from the breakthrough or the overcoming of the barrier itself; an explanatory example are the bridge safety barriers: this is in fact the reason why a bridge safety barrier can be designed admitting an ASI until 1.4 and in certain cases until 1.9, while usually it must be less than 1.

6.2. Verification of the compatibility between barrier and bridge

An important task which designers of bridge safety barriers have to absolve is the verification of the compatibility between the resistance of the structure and the loads that the barrier transmits to it.
The set of measurements nowadays acquired during a common crash test does not usually include detections with dynamometers and accelerometers placed on the posts or on the anchor bolts, although the recent research is trying to improve the achievement of information about the stress distribution on the structure during the impact.
Currently, only estimations about the global force transmitted by the vehicle to the barrier are available; the European standard EN 1317 provides three different criteria to estimate the average force due to an impact: the last one, for instance, calculates the average traversal force as a function of the impact energy and the maximum Dynamic Deflection detected.
The recent Italian Technical Norms for the Constructions define the following general characteristics of the impact force due to an errant vehicle [9]:

- Intensity not less than F = 100 kN
- Horizontal
- Traversal with respect to the barrier rail direction
- Distributed on a length of 0.5 m

- Applied at an height h measured from the road level; h is the lower length between h_1 and h_2, where:
  - h_1 is the barrier height minus 0.1 m
  - h_2 = 1 m

In order to define the section of the structure which is supposed to endure the momentum related to that force, it must be noted that this momentum exceeds the value which causes the yielding of a single post, and that from the crash tests performed it is evident that the metallic rail distribute the load on several posts.
A preliminary criterion consists of the estimation of the momentum transmitted to the structure according to the force defined by the norm and the characteristics of the post.
In particular, it is assumed that the number of posts involved in the impact is equal to the ratio

$$n = \frac{F \cdot h}{M_p} \tag{6.5}$$

where F and h are the values previously defined by the norm and M_p is the plasticizing momentum of the single post.
Each of those posts hence suffers a traversal load

$$F_p = \frac{F}{n} \tag{6.6}$$

Multiplying to each other the values of F_p and of the lever arm h above defined it is possible to calculate the momentum transmitted to the structure by a single post.
The critical section of the structure, solicited by this momentum, is defined assuming a stresses propagation according to an angle of 45° centered on the concerned post.

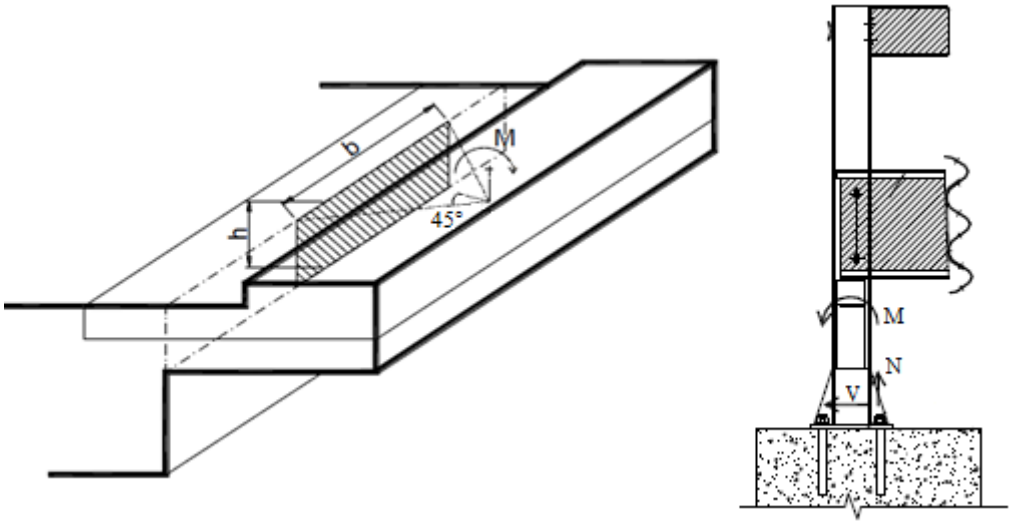

Figure 6.10. Bridge critical section due to an impact on the safety barrier [9].

The structure is besides solicited by the vehicle weight; in order to consider even this load, it is assumed that during the impact the vehicle leans only on its outer side wheels. Hence, the vertical load due to the weight is applied on a point corresponding to the outer wheel belonging to the more solicited axle; the stresses distribution is the same.
The verifications with respect to those two types of load can be carried separately, since although they both occur during the impact, it is reasonable to assume that one prevails over the other at different phases during the impact.

Lastly, an important aspect which designers have to take in account, is the barrier placement with respect to other elements like acoustic barriers, parapets for pedestrian paths, nets, windbreak barriers, etc. In general, those elements should be placed outside the barrier Working Width.
The problem is even more relevant in the case of cable-stayed bridges; if the barrier is placed at an inappropriate distance from the structural supporting elements, such as towers and cables, serious problems may occur: firstly, an inadequate behavior of the barrier; secondly, and even worse, the possibility of impact between a heavy vehicle and a structural element, which may result in the damage of that element and the impairment of the structure stability and functionality.
Figure 6.11 shows the possible interaction between a bridge safety barrier and the structural cables.

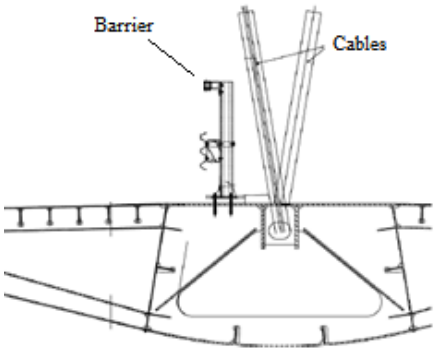

Figure 6.11. Possible interaction between safety barrier and structural cables on a bridge [9].

6.3. Bridge safety barrier numerical model

The concerned barrier, belonging to the class H4b, is constituted by the following elements:

- Posts
- Triangular reinforcements
- Plates
- Anchor bolts
- Spacers
- Tubes
- Connecting elements between the tubes sections
- Bolting

The materials which these elements are made of are listed in Table 6.8.

Table 6.8. Elements and materials of the bridge safety barrier.

Element	Material
Posts	S355-MC
Triangular reinforcements	S355-MC
Plates	S355-MC
Anchor bolts	Steel class 8.8
Spacers	S355-MC
Tubes	S355-JRH
Connecting elements (lower tubes)	S235-JRH
Connecting elements (upper tube)	S335-JRH
Bolting	Steel class 8.8

Four different steels are present in this barrier.
The tubes and the upper connecting elements are made of a steel identified by the code S355-JRH, while the posts, the triangular reinforcements, the plates and the spacers are made of the steel S355-MC. These two steels have the same mechanical characteristics, as far as concerns the Young's modulus and the Poisson's ratio. The difference between them concerns other characteristics, which will be here shortly explained.
Steels are identified through codes such as those above mentioned. The first letter indicates the primary use of the steel, that can be, for instance:

- S – Steels for structural use
- P – Steels to be used in under pressure conditions
- L – Steels for pipelines
- E – Steels for mechanical constructions

The number that follows indicates the minimum yield stress. The last letters point out different properties, which in these cases are:

- JRH – The value of the steel resilience is not less than 27 J/m^2 at 20°C.
- MC – The material has been subjected to a thermo-mechanical lamination process (letter M) and it is suitable to the cold forming (letter C).

The bolting is composed as indicated in Table 6.9.

Table 6.9. Bolting elements present in the barrier.

Bolted elements	Dimensions	Torque [Nm]
Posts – Lower spacers	M16	90
Posts – Upper spacers	M20	90
Lower tubes – Connecting elements	M16	90
Upper tube – Connecting elements	M16	90
Anchor bolts	M24	180

Post model

The first to be developed has been the numerical model of the post, which can be seen in Figure 6.12.

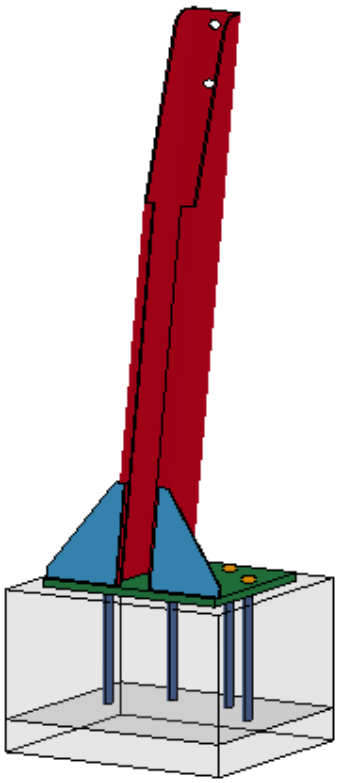

Figure 6.12. Post numerical model.

The post and the triangular reinforcements have been modeled using shell elements.
They are welded to a plate which is drilled in four points, where the anchor bolts are placed. The plate has been modeled using solid elements.
All these elements are made of the steel S355-MC, which has been reproduced through the LS-Dyna® feature *MAT_PIECEWISE_LINEAR_PLASTICITY.
Since no further information was available, the σ-ε minimum curve of the steel S355-MC has been chosen to represent the plastic range.
The welding constraint between the post and the plate has been imposed by merging the nodes on the base of the post to a set of suitably placed nodes belonging to the plate. The same has been done to represent the welding between the plate and the triangular reinforcements.
Since it would have been impossible to do the same between the post and the reinforcements, because of the shell thickness, the LS-Dyna® feature *CONTACT_TIED_SHELL_EDGE_TO_SURFACE_OFFSET has been used to represent the welding between those two elements. This contact allows to constrain two parts to each other and transmit forces and moments. The

"OFFSET" option has been necessary because of the distance between the post surface and the reinforcements surface.
The anchoring system consists of four bolts M24 belonging to the steel class 8.8. Even this material has been represented by means of the *MAT_PIECEWISE_LINEAR_PLASTICITY. Since the whole σ-ε curve of this material was not available, a bilinear behavior has been chosen for it. The needed values have been achieved from the information about the steel class:

- Density: $\rho = 7.8 \cdot 10^{-9}$ ton/mm^3
- Young's modulus: $E = 2.1 \cdot 10^5$ N/mm^2
- Poisson's ratio: $\upsilon = 0.3$
- Yield stress: $\sigma_y = 640$ N/mm^2
- Rupture stress: $\sigma_r = 800$ N/mm^2
- Rupture strain: $\varepsilon_r = 0.12$

This material has been used both for the shank and the head of the bolts. The head has been modeled by means of shell elements, while the shank has been modeled with solid elements. The head and the shank of the bolts are constrained to each other by means of merged nodes.
Regarding the concrete, which belongs to the class C50/60 it has been represented in LS-Dyna® by means of the feature *MAT_CSCM_CONCRETE with an ultimate compression strength of $f'_c = 50$ N/mm^2 and a maximum aggregates size of Dagg = 25 mm.
The interaction between the anchor bolts and the concrete has been modeled by means of the *CONTACT_TIED_SURFACE_TO_SURFACE_FAILURE, as made for the tests in Chapter 5.
Assuming that the bonding resin utilized is the same used for the posts push tests described in Chapter 5, the stress values at failure have been set to 343 N/mm^2.
The anchor bolts preload has been calculated, as previously made, in the following way:

$$d_n = 24 \text{ mm}$$
$$p = 3 \text{ mm}$$
$$h = 1.84 \text{ mm}$$
$$A_{res} = 353 \text{ mm}^2$$

The static coefficient of friction between steel and concrete is $\mu = 0.6$. Hence:

$$\beta = \tan^{-1}(\mu) = 30.96° \tag{6.7}$$

$$\gamma = \tan^{-1}\left(\frac{p}{\pi \cdot d_n}\right) = 2.28° \tag{6.8}$$

It is known, from the crash test report, that the value of the torque applied on the anchor bolts is T = 180 Nm. Hence:

$$r = \frac{d_n - 2 \cdot h}{2} = 10.16 \text{ mm} \tag{6.9}$$

$$F = \frac{T}{r \cdot tg(\gamma + \beta)} = 27032.49 \text{ N} \tag{6.10}$$

$$\sigma = \frac{F}{A_{res}} = 76.58 \ \frac{N}{mm^2} \tag{6.11}$$

$$J = \frac{\pi \cdot r^4}{2} = 16737.66 \text{ mm}^4 \tag{6.12}$$

$$d = 2 \cdot r = 20.32 \text{ mm} \tag{6.13}$$

$$\tau = \frac{T \cdot d}{2 \cdot J} = 109.26 \ \frac{N}{mm^2} \tag{6.14}$$

$$\sigma_{pr} = \sqrt{\sigma^2 + 3 \cdot \tau^2} = 204.15 \ \frac{N}{mm^2} \tag{6.15}$$

The value of the coefficient of thermal expansion for the steel is $\alpha = 1.7 \cdot 10^{-5}$ K^{-1}. After several tests, it has been found that the suitable value of the temperature variation to impose a stress of $\sigma_{pr} = 204.15$ N/mm^2 is $\Delta T = -67.3$ K.

As explained in Appendix A.3, the preload has been introduced in the model through the cards *MAT_ADD_THRMAL_EXPANSION, to assign the coefficient of thermal expansion to the steel which the bolts are made of, and *LOAD_THERMAL_LOAD_CURVE, to impose a thermal load to that material.

Barrier model

Afterwards, the numerical model of the complete barrier has been realized.
In order to reduce the computational cost of this numerical model, only the posts assumed to be directly interested by impact or major deformation have been modeled including all the details previously described. All the other posts do not include the anchor bolts, the nuts and the concrete slab; those posts have been constrained to the ground through a *BOUNDARY_SPC_SET, including the nodes on the bottom surface of each plate. It has been checked that these posts are not interested by the impact or a significant deformation, hence it can be assumed that the approximation does not compromise the reliability of the model.

This barrier is characterized by three cylindrical tubes, with different thicknesses and diameters, supported by means of two spacers.
Tubes and spacers are connected to each other by means of a welding, while the spacers are bolted to the posts.

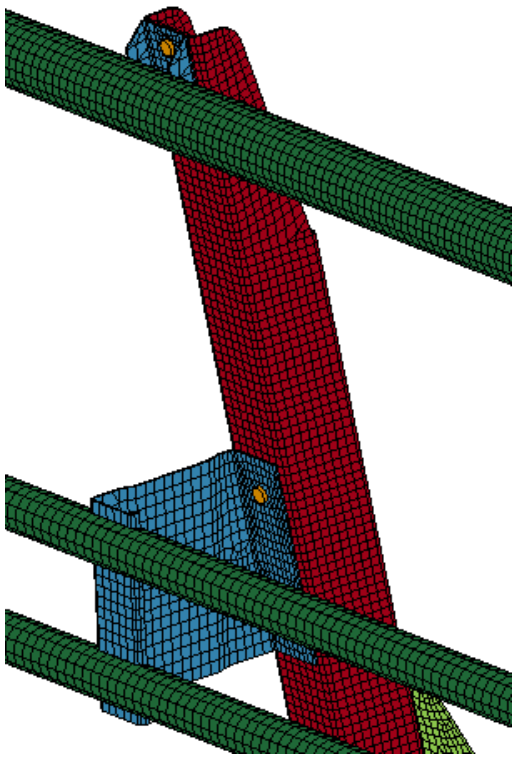

Figure 6.13. Detailed view of some barrier elements: post, triangular reinforcements, spacers, tubes, bolting.

The welding between the tubes and the spacers has been realized via three cards named *CONTACT_TIED_NODES_TO_SURFACE_OFFSET; in each of them, a set of nodes belonging to the spacers has been tied to the surface of the corresponding tube.
Regarding the bolting, each spacer is connected to a post by means of two bolts; the bolts which link the lower spacers are M16, while the bolts which link the upper ones are M20.
All the bolts used to connect the spacers to the posts are made, like the anchor bolts, of a steel belonging to the class 8.8.
Two different features have been used to model the material which the bolts are made of.
For the heads and the nuts, the card *MAT_PIECEWISE_LINEAR_PLASTICITY has been used, defining a bilinear σ-ε curve, as made for the anchor bolts.
For the shanks, instead, the feature *MAT_SPOTWELD_DAMAGE_FAILURE has been chosen. This card allows to introduce the maximum axial and shear stresses at failure, which can be achieved from the steel class (8.8):

- $\sigma_r = 8 \cdot 100 = 800$ N/mm^2
- $\tau_r = \frac{\sigma_r}{\sqrt{2}} = 566$ N/mm^2

The preload on these bolts has been imposed, as explained in details in Appendix A.3, through the feature *INITIAL_AXIAL_FORCE_BEAM, which allows the user to introduce an axial force on the bolts shank, if constituted by a beam element.
Since it is known from the crash test report that the torque applied is T = 90 Nm, the axial force acting on the shank can be achieved from the information about the thread, as previously made for the calculation of the preload to impose on the anchor bolts.
For bolts M16:

$$d_n = 16 \text{ mm}$$
$$p = 2 \text{ mm}$$
$$h = 1.227 \text{ mm}$$

In this case the static coefficient of friction to consider is the one between two components made of steel, which is $\mu = 0.4$. Hence:

$$\beta = \tan^{-1}(\mu) = 21.80° \tag{6.16}$$

$$\gamma = \tan^{-1}\left(\frac{p}{\pi \cdot d_n}\right) = 2.28° \tag{6.17}$$

$$r = \frac{d_n - 2 \cdot h}{2} = 6.773 \text{ mm} \tag{6.18}$$

$$F = \frac{T}{r \cdot tg(\gamma + \beta)} = 29733.66 \text{ N} \tag{6.19}$$

For bolts M20:

d_n = 20 mm
p = 2.5 mm
h = 1.534 mm

$$\beta = \tan^{-1}(\mu) = 21.80° \tag{6.20}$$

$$\gamma = \tan^{-1}\left(\frac{p}{\pi \cdot d_n}\right) = 2.28° \tag{6.21}$$

$$r = \frac{d_n - 2 \cdot h}{2} = 8.466 \text{ mm} \tag{6.22}$$

$$F = \frac{T}{r \cdot tg(\gamma + \beta)} = 23787.63 \text{ N} \tag{6.23}$$

Shell elements have been used to realize the spacers, the tubes, the heads and the nuts of the bolts, while the shanks have been modeled with beam elements. Because of that, a special contact was needed; in fact, since the software does not consider the beams surfaces, the feature already used *CONTACT_AUTOMATIC_SINGLE_SURFACE does not prevent the interpenetration of two parts if one of them is made by a beam element.
In order to solve this problem, these auxiliary elements have been created:

- A “null beam” coincident with the shank of the bolt, with the same diameter of the actual shank.

- A set of “null beams” placed on the boundary of the holes, both on the post and on the spacer; these beams must have an arbitrary small diameter, such as 1 mm.

These beams must be realized through the feature *MAT_NULL, which is a special material that does not influence the stiffness and the behavior of the model.
All the above defined “null beams” must be included in a set of parts to which it must be assigned the *CONTACT_AUTOMATIC_GENERAL, which works similarly to the *CONTACT_AUTOMATIC_SINGLE_SURFACE, but is suitable for the contact between beam elements.
Figure 6.14 shows the elements used to model a bolt and the contact between its shank and the holes in which it is inserted. It is possible to see the head and the nut, modeled through shell elements, the shank, modeled through a beam element, and the two rings of “null beams”, one placed on the boundary of the hole on the post, the other placed on the boundary of the hole on the spacer; the “null beam” on the shank is not visible because it coincides with the actual shank.

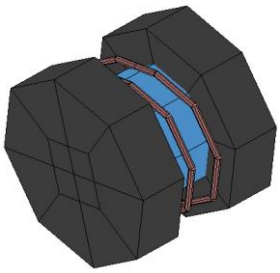

Figure 6.14. Model of a bolt connecting the posts and the spacers.

The tubes sections are connected to each other by means of cylindrical elements, shown in Figure 6.15.

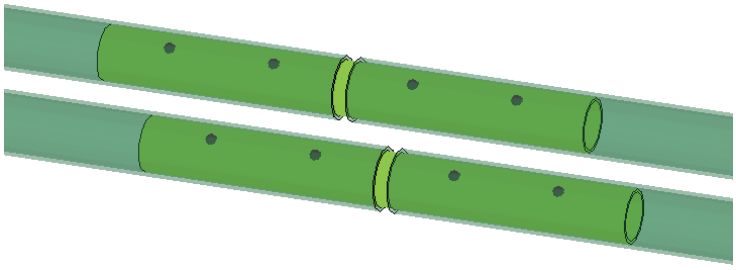

Figure 6.15. Cylindrical elements connecting the tubes sections.

Each connecting element is linked to two tubes sections by means of eight bolts M16.
In this case the bolting has been modeled in a simpler way, i.e. though spotweld elements. Spotwelds are defined as circular section beams whose tips are tied to the surfaces to be jointed.
The material has been modeled through the card *MAT_SPOTWELD, which allows to introduce the axial and the shear forces at failure, achievable from the steel class (8.8) and the radius of the bolts core (r = 6.773 mm):

- $\sigma_r = 8 \cdot 100 = 800$ N/mm^2 → $N_F = \sigma_r \cdot (\pi \cdot r^2) = 115292.75$ N
- $\tau_r = \frac{\sigma_r}{\sqrt{2}} = 566$ N/mm^2 → $R_F = \tau_r \cdot (\pi \cdot r^2) = 81569.62$ N

The preload, previously calculated for the bolting between the spacers and the posts, has been introduced through the card *INITIAL_AXIAL_FORCE_BEAM, since the spotwelds act like beam elements.

Eventually, a set of parts including the entire barrier has been defined; it has been afterwards used to impose the contact between the vehicles and the barrier, through the feature *CONTACT_AUTOMATIC_SURFACE_TO_SURFACE. In this card, the two sets of parts which must not interpenetrate to each other must be introduced; the first set includes all the elements of the barrier, while the second includes all the elements of the vehicle.
A “rigid-wall” has been lastly placed in correspondence of the upper surface of the concrete slabs, in order to simulate the presence of the ground, which cannot be crossed by any part of the barrier and of the vehicle.

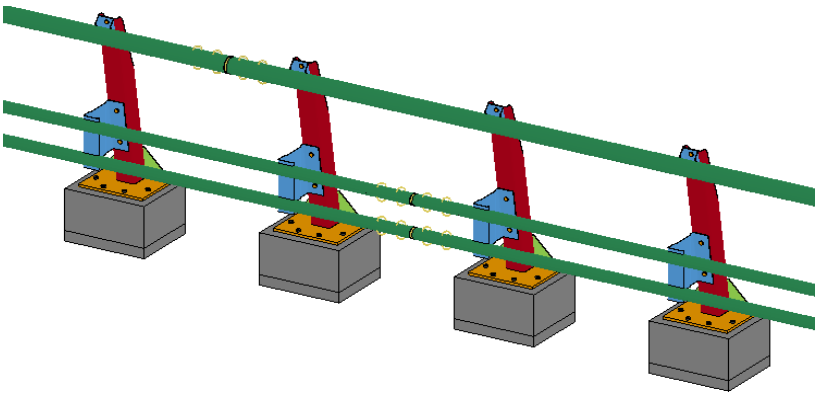

Figure 6.16. Barrier complete numerical model.

6.4. Vehicles models

The vehicles numerical models utilized to perform the two full-scale crash tests on the bridge safety barrier are:

- A lightweight car
- An articulated truck

They both will be here shortly described.

The first model, used for the test TB11, is a lightweight car, with the characteristics reported in Table 6.10.

Table 6.10. Characteristics of the car numerical model.

Weight [ton]	Length [m]	Width [m]	Height [m]
0.9	3.74	1.58	1.44

The finite elements model is made approximately by 30000 shell elements and 800 solid elements.
The card used to define the materials characteristics is based on an isotropic elastic-plastic model, whose properties have been already described in Paragraph 5.2.1, while the suspension assembly has been realized through viscous and elastic discrete elements.
In order to achieve the data needed to calculate the crash test parameters such as the ASI, an accelerometer has been placed on the vehicle center of gravity; the software is hence able to provide displacements, velocities and accelerations of that node along the three directions of the vehicle local reference frame.
The car model is shown in Figure 6.17.

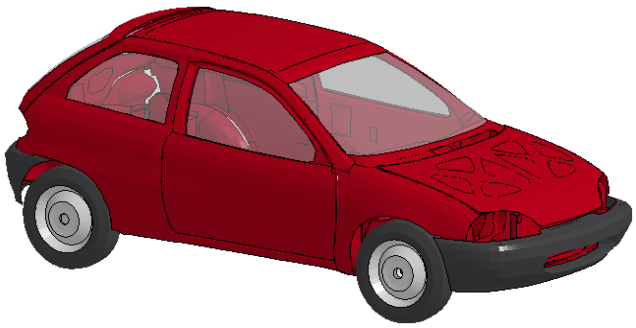

Figure 6.17. Car numerical model.

The second model, used for a test TB81, is an articulated truck, with the characteristics reported in Table 6.11.

Table 6.11. Characteristics of the articulated truck numerical model.

Weight [ton]	Length [m]	Width [m]	Height [m]
38	14.74	2.62	3.61

The finite elements model is made approximately by 2500 solid elements and 105000 shell elements.
The same can be said about the materials used to model the main parts of the truck and the suspension assembly.
Even in this model, in order to achieve the data needed for the calculation of the crash test parameters, an accelerometer has been placed on the tractor.
The truck model is shown in Figure 6.18.

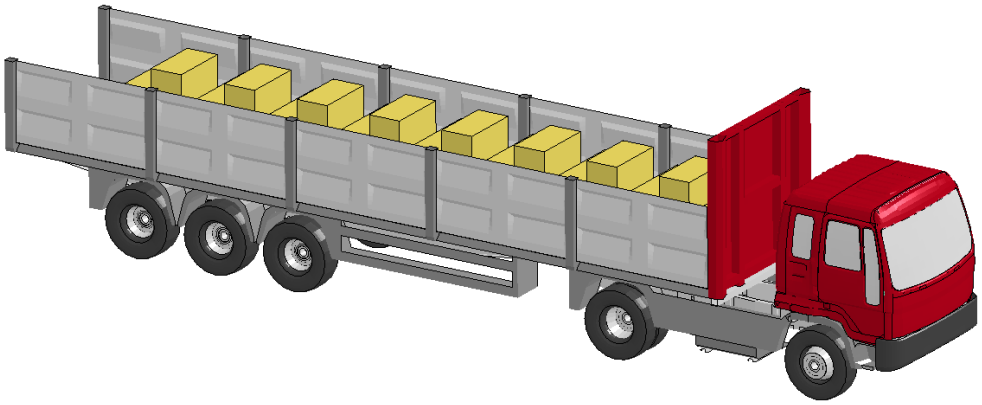

Figure 6.18. Articulated truck numerical model.

6.5. Tests results

The concerned barrier belongs to the class H4b; hence, the validation tests performed are a TB11 and a TB81.
Previously, a push test on a single post has been performed and numerically reproduced.

Test on the post

Figure 6.19 show a comparison between the experimental and the numerical tests.

In both cases it is possible to note the maximum deformation of the post concentrated just above the triangular reinforcements.
The central figure refers to the Von Mises stress, while the one on the right shows the plastic strain.

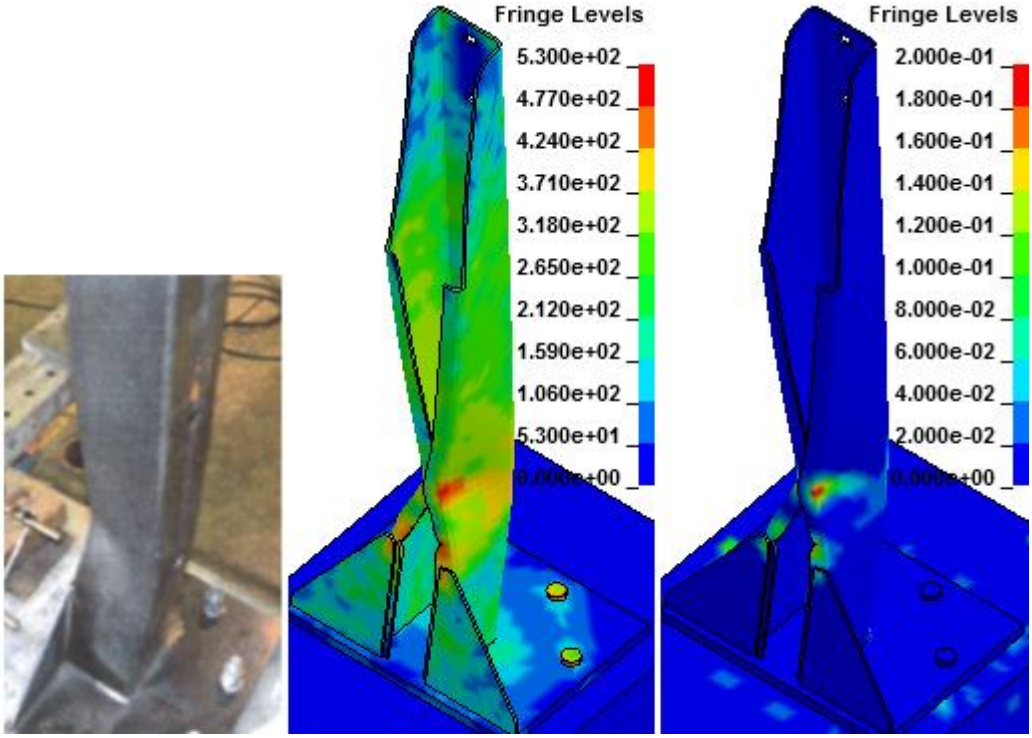

Figure 6.19. Post push test: failure modes; experimental case (on the left), Von Mises stress (in the middle) and plastic strain (on the right).

The graphics in Figure 6.20 represent the force applied by the pushing machine as a function of the imposed displacement, both in the experimental test (on the left) and in the numerical model (on the right).

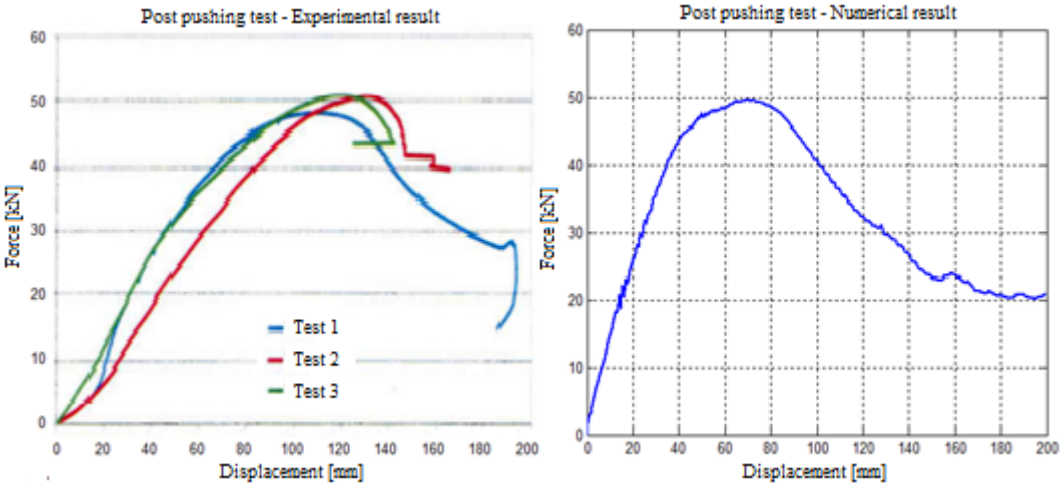

Figure 6.20. Post push test: force imposed by the machine as a function of displacement; three experimental cases (on the left) and numerical case (on the right).

Test TB11

In order to demonstrate the barrier numerical model reliability, a validation and verification procedure (V&V) has been carried out, according to what established by the regulation EN 1317 [21].
Initially, it has been verified, through a preliminary qualitative analysis, that the barrier behavior was acceptable: this implies that the restrain system is able to contain and redirect the errant vehicle with no roll-over, that no elements of the barrier penetrate into the vehicle cabin and that no ruptures occur to the longitudinal elements of the system.
Figures 6.21 and 6.22 show that the barrier qualitative behavior is acceptable and correlated with the experimental results as far as concerns the test TB11.

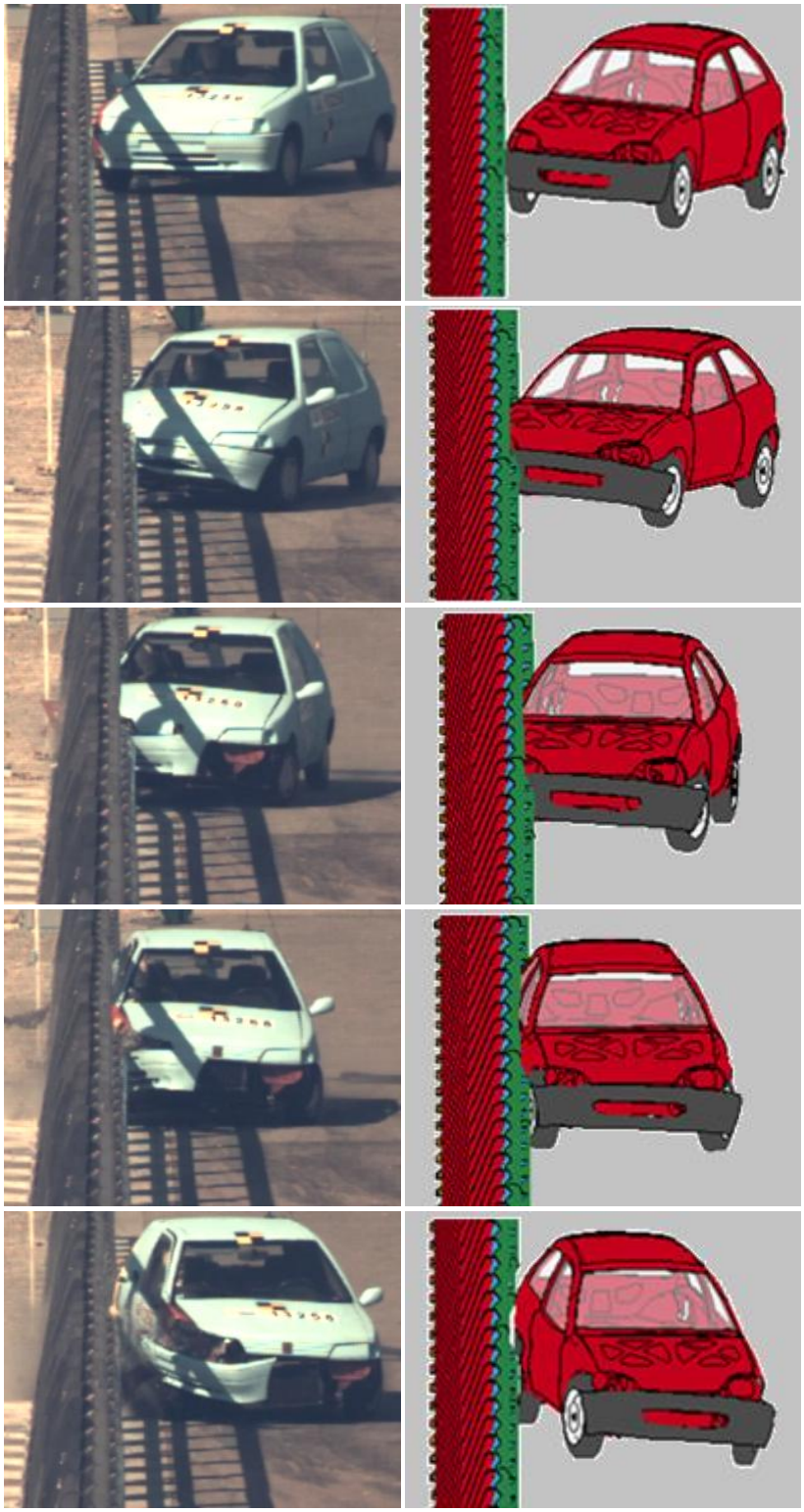

Figure 6.21. Test TB11: experimental-numerical comparison of the impact dynamics.

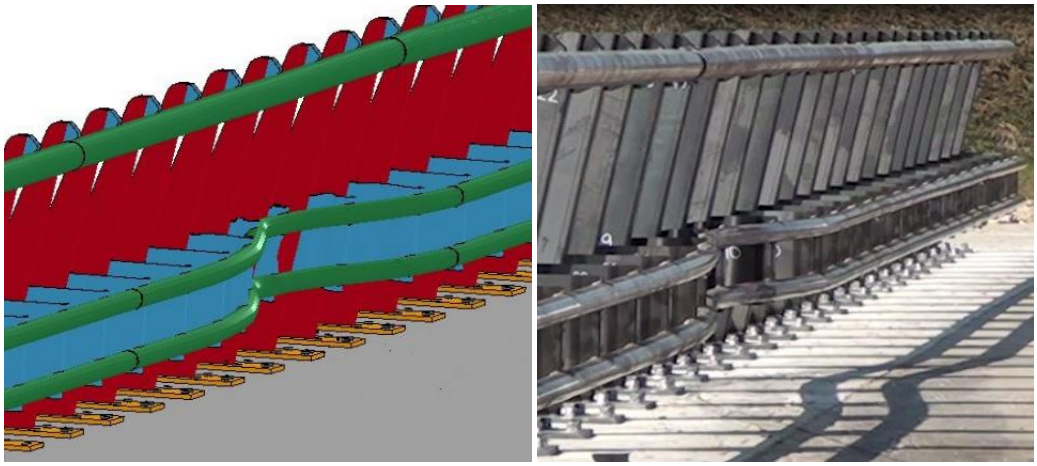

Figure 6.22. Test TB11: experimental-numerical comparison of the barrier deformation.

Secondly, the principal crash test parameters have been assessed, in order to verify their compliance with the prescribed values and to compare them with the experimental tests results.
The results achieved for the test TB11 are shown in Table 6.12.

Table 6.12. Test TB11: impact severity and barrier deformation indexes.

	Experimental crash test	Numerical simulation	Maximum admitted value
Working width [m]	-	0.66	-
Vehicle intrusion [m]	-	0.33	-
Dynamic deflection [m]	-	0.35	-
ASI [-]	1.2	1.37	1.4
THIV [km/h]	28	30.7	33
PHD [-]	-	9.8 g	20 g

Figure 6.23 shows the values of the indexes related to the barrier deformation achieved in the numerical simulation.

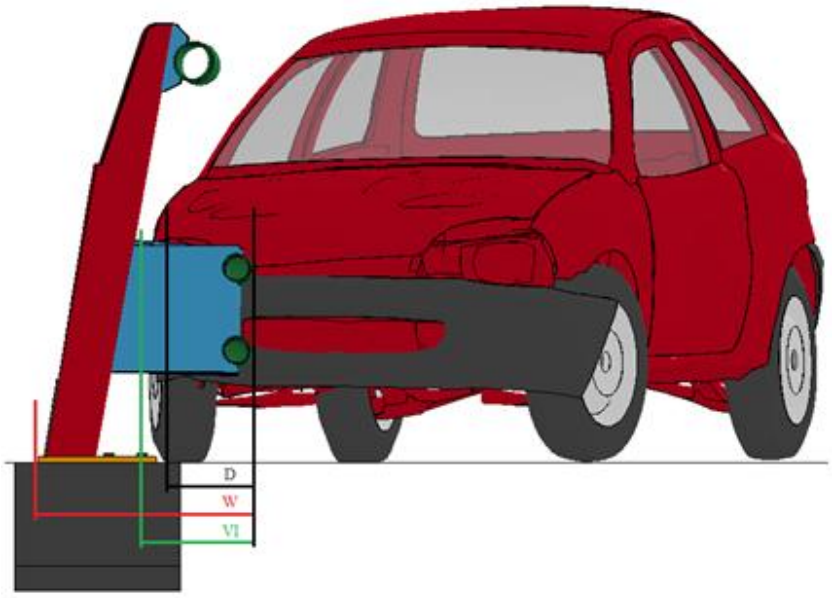

Figure 6.23. Test TB11: scheme of the barrier deformation parameters.

The impact severity level for this test, according to Table 6.4, is B.
The graphic in Figure 6.24 shows the trend of the index ASI during the impact time period.

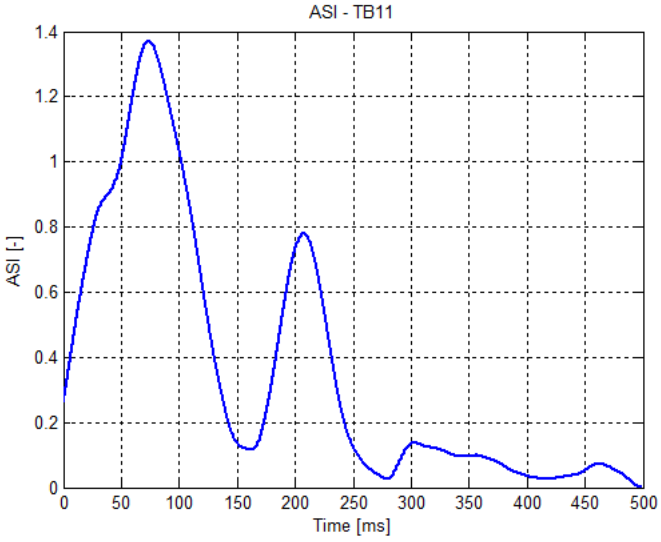

Figure 6.24. Test TB11: trend of the index ASI during the impact.

Lastly, to conclude the validation and verification procedure, it has been necessary to ensure that the simulation has not been affected by any possible

numerical issue, which might have compromised the results reliability; for this purpose, the checks listed in Table 6.13 have been executed.

Table 6.13. Test TB11: numerical checks.

Check	Result	Maximum admitted value
Total energy variation	0.73%	10%
Global hourglass energy vs. total energy	0.01%	5%
Global hourglass energy vs. global internal energy	0.50%	10%
Local hourglass energy vs. local internal energy	0.06%	10%
Global added mass	0.04%	5%
Local added mass	6.25%	10%
Added kinetic energy	0.26%	5%
Shooting nodes	0	0
Negative volumes	0	0

Test TB81

The same procedure has been carried out for the test TB81. As visible in Figures 6.25 and 6.26 the barrier overall behavior is acceptable.

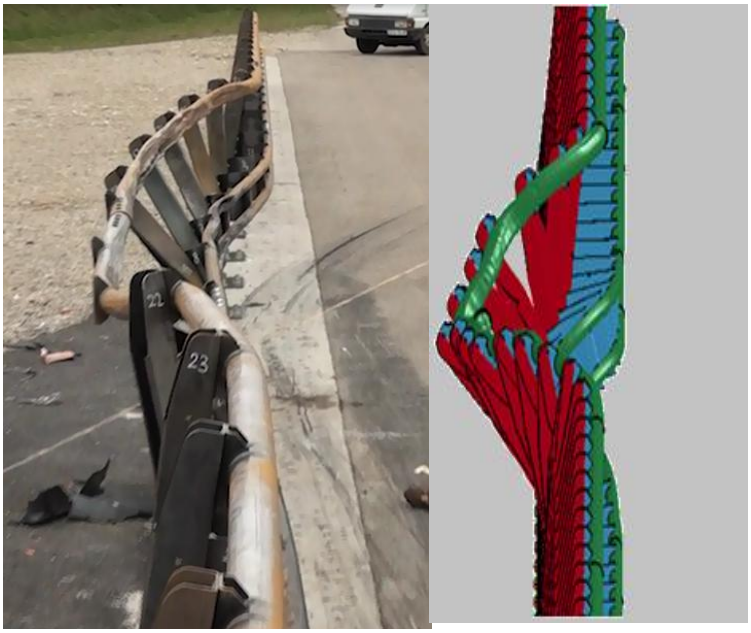

Figure 6.25. Test TB81: experimental-numerical comparison of the barrier deformation.

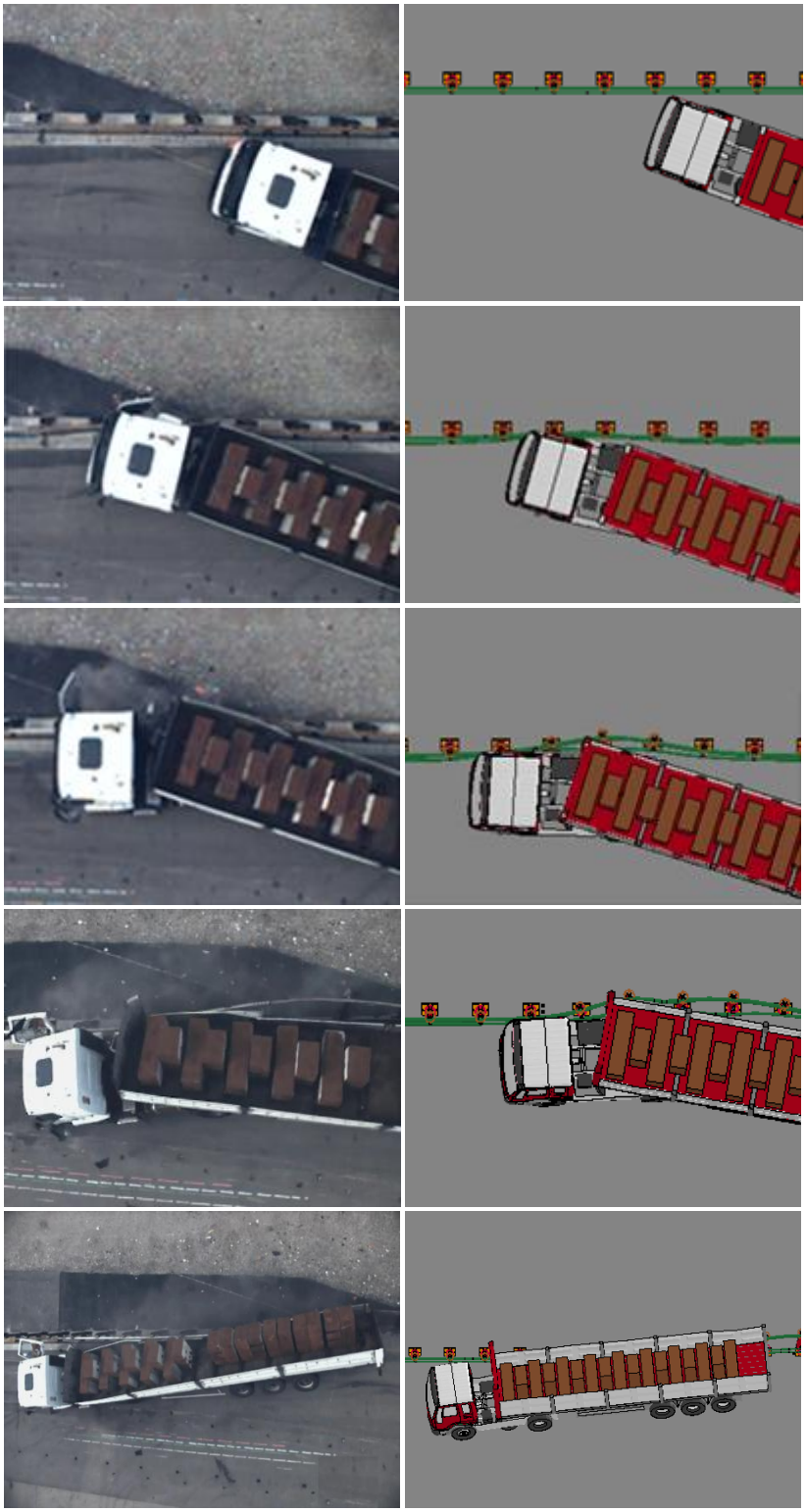

Figure 6.26. Test TB81: experimental-numerical comparison of the impact dynamics.

The deformation, as expected, is much more relevant than the previous test, as indicated by the parameters shown in Table 6.14.

Table 6.14. Test TB81: impact severity and barrier deformation indexes.

	Experimental crash test	Numerical simulation	Maximum admitted value
Working width [m]	1.30	1.10	-
Vehicle intrusion [m]	3.5	2.5	-
Dynamic deflection [m]	-	0.61	-
ASI [-]	-	0.82	1.4
THIV [km/h]	-	20.4	33
PHD [-]	-	12.2 g	20 g

The VI of the Heavy Goods Vehicles (HGV) is evaluated considering a notional load having the width and the length of the vehicle platform and a total height of 4 m. It shall be evaluated by measuring the position and the angle of the vehicle platform and assuming that the notional load remain undeformed.
Figure 6.27 shows the values of the indexes related to the barrier deformation achieved in the numerical simulation.

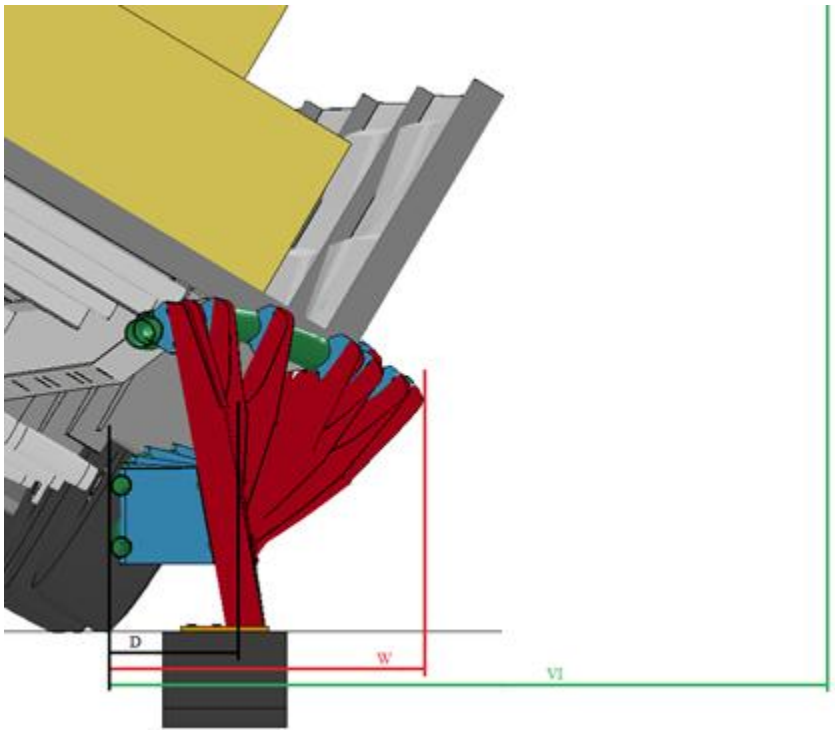

Figure 6.27. Test TB81: scheme of the barrier deformation parameters.

The impact severity level for this test, according to Table 6.4, is B.
The graphic in Figure 6.28 shows the trend of the index ASI during the impact time period.

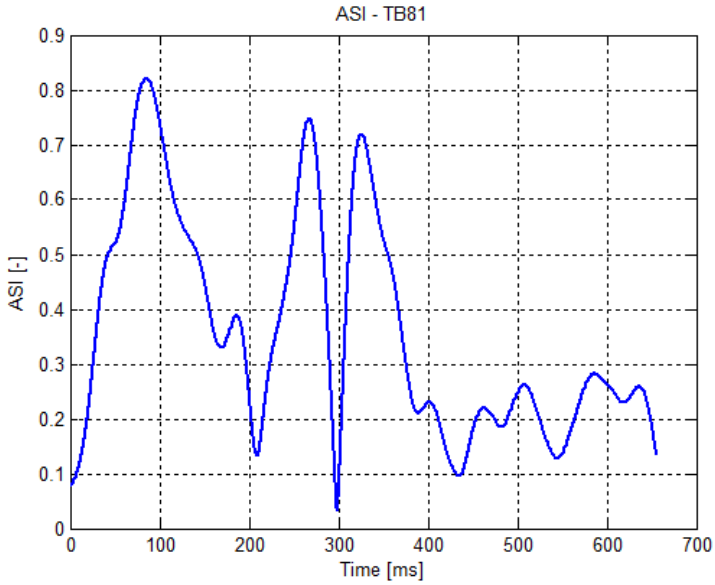

Figure 6.28. Test TB81: trend of the index ASI during the impact.

Lastly, the same checks have been executed in order to verify the model reliability.

Table 6.15. Test TB81: numerical checks.

Check	Result	Maximum admitted value
Total energy variation	1.85%	10%
Global hourglass energy vs. total energy	0.0006%	5%
Global hourglass energy vs. global internal energy	0.09%	10%
Local hourglass energy vs. local internal energy	4.58%	10%
Global added mass	0.03%	5%
Local added mass	0.47%	10%
Added kinetic energy	3.08%	5%
Shooting nodes	0	0
Negative volumes	0	0

In this test the vehicle had a problem of roll-over. From a comparison with the videos of the experimental crash test it has been seen that the behavior of the model is quite different from the one of the real truck.
Thus, a possible future development will be study and improve the model of truck used, in order to achieve a better results.
The barrier, instead, has been able to correctly restrain the vehicle and showed a behavior similar to the real crash test; hence, the barrier model can be considered acceptable in this preliminary analysis.

7. Conclusions and future developments

7.1. Conclusions

The study carried out in this thesis conducted to the development of a bridge safety barrier numerical model for crash test simulations, reliable and well representative of the physical reality of these structures.
The material characterization procedure and the numerical-experimental correlation of the tests provided satisfactory results.
The behavior of the model chosen to represent the link between the barrier and the bridge turned out adequate, both locally, in the posts push tests, and at a full-scale level, in the crash test simulations performed at the end of the work.
The model realized includes all the components present in a bridge safety barrier, hence it can be used to fulfill crash test numerical simulations on this type of structures, with the possibility of analyzing several aspects:

- Stresses and strains to which the elements of the barrier are subjected, e.g. the axial and shear stresses acting on the anchor bolts or the nuts during an impact, in order to verify the correct dimensioning (see Figure 7.1);
- Stresses at the interface between the anchor bolts and the concrete curb, so as to determine the minimum required strength of the bonding to realize;
- Loads transmitted from the barrier to the bridge structure during an impact; it is possible, indeed, to define horizontal or vertical plans, at the desired height along the curb, in correspondence of which the software can compute the forces and the moments generated, in order to have an idea about the loads to which the bridge is subjected during the impact and detect potential issues.

Once achieved the desired information, it is possible to proceed to an eventual design optimization, properly varying the parameters present in the model, such as the material properties or the geometrical characteristics, in order to obtain satisfactory results, for instance regarding the bonding strength or the loads transmitted to the bridge.

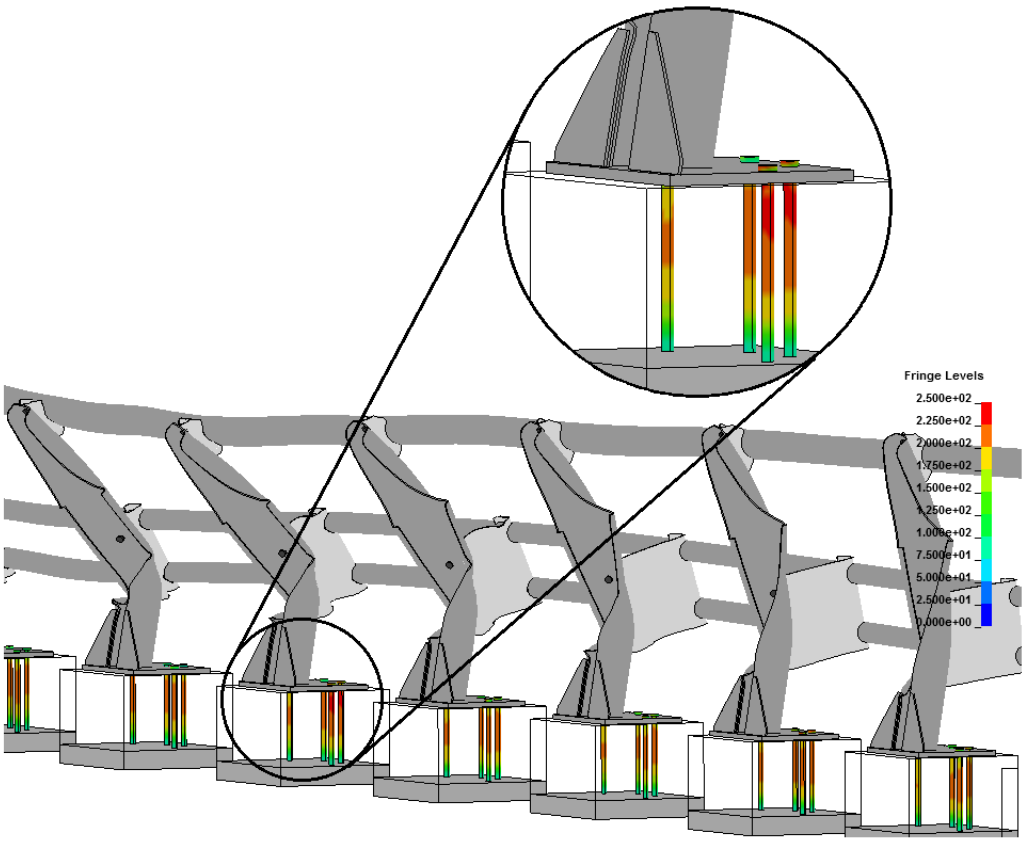

Figure 7.1. Example of Von Mises stress acting on the anchor bolts during an impact.

7.2. Future developments

The work performed in the last chapter had the purpose of verifying that the barrier model so realized showed an acceptable behavior, but did not provide for a numerical-experimental calibration procedure.
For that purpose, the first step could be try to further improve the barrier model, to achieve better results, closer to the experimental ones, concerning the impact severity indexes and the parameters related to the barrier deformation.
There are in fact many parameters on which it is possible to fulfill a study, just think that in the model there are four different types of steel and three types of bolting, of which it is possible to vary the σ-ε curve or the rupture loads.

Regarding the concrete, a characterization has been performed through the fulfillment of two experimental tests, the uniaxial compression of cubic and

cylindrical specimens, and the following numerical-experimental correlation of the developed models.
Further tests will be realized, i.e. triaxial compression and extension tests, hydrostatic compression tests and uniaxial strain tests; the results will be used to further improve the material characterization.

Eventually, regarding the representation of the contact between the anchor bolts and the concrete, in the developed model the settled failure stresses are the ones hypothesized for that type of bonding.
A more refined modeling would include some traction tests of bonded anchor bolts, similar to the ones performed numerically and described in Appendix A.2, from which it would be possible to determine the exact value of the failure stresses, related to that type of bonding.
Moreover, it was mentioned that this model takes in account the failure possibility of the link between the anchor bolts and the concrete curb, but the functioning of the defined contact consists just of the detachment of the two concerned parts once the stress on the interface reaches the settled value.
A further development could be modeling even the resin, hence taking in account its pliancy, e.g. by introducing a new part placed between the anchor bolts and the hole surface, to which it should be then assigned an elastic modulus, a shear modulus, a σ-ε curve, a failure strain, etc.

A. Details about the model development

A.1. Other models of the barriers anchoring systems

Numerical models commonly used to perform crash test simulations of road safety barriers differ from the one here developed because of their link with the soil [10].
In these cases, the posts are embedded into the ground for a certain length. Then, the simplest way to constrain the barrier into the soil is by rigidly fixing the posts under a certain level, so as to prevent every possible displacement and rotation of the nodes under that level, which may correspond to the ground itself or to a lower level; this second solution is often adopted in order to take somehow in consideration the influence of the soil deformability, which has a tendency to lower the point corresponding to the plastic joint which originates at the base of the post.
This type of modeling provides the advantage of a null computational cost added; moreover, the model is characterized by an extreme simplicity, but on the other hand its accuracy is quite low, particularly regarding the stress distribution on the area where the post yielding occurs.

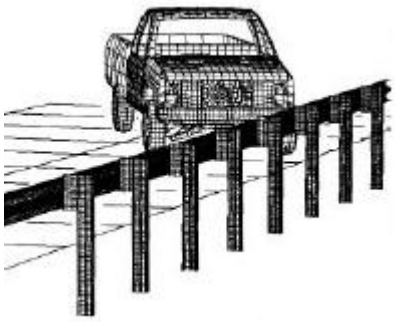

Figure A.1. Example of barrier-soil link: constrained nodes [10].

The influence of the soil may also be taken into account in a more accurate way by means of a set of non-linear spring elements applied to the embedded part of each post; an example of such a model is shown in Figure A.2.
Those springs are characterized by a stiffness curve which may be a function of the depth, the geometry of the post, the characteristics of the soil or the crushing.

Several empirical formulas, which take in account all these parameters, have been achieved from experimental data; through them, the force-displacement curve to be assigned to the springs can be obtained.
Such a model provides the advantage of a very low computational cost added, as well. The disadvantages are, besides the obvious higher complexity, which requires more work, the poor accuracy in case of large displacements of the post; furthermore, varying the soil characteristics is more difficult, since it is necessary to recalculate all the curves related to the springs.

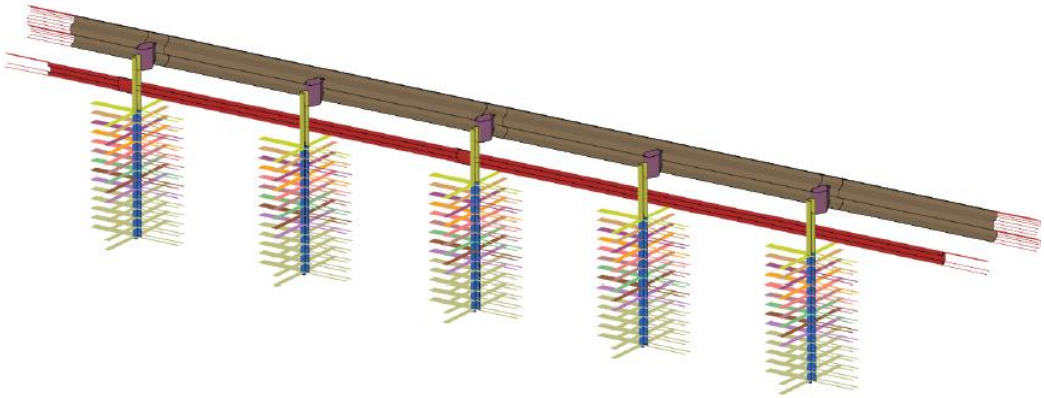

Figure A.2. Example of barrier-soil link: spring elements [22].

Of course all these models consider neither the anchor bolts nor the concrete failure possibilities, but the approximation is good if these are not the subjects of the simulation; indeed, they are often successfully utilized in order to analyze the behavior of the vehicle, the guardrail, the posts and the bolting which connects the posts to the spacers or the spacers to the guardrail.
Lastly, the soil can be modeled like a common structural element, which means by creating an appropriate volume, usually cylindrical, around each post, and meshing it by means of solid elements; afterwards it is necessary to define the material properties.
The main advantage which this solution provides is the high accuracy for low deformations; the disadvantages are the very high computational cost, with respect to the previously described models, due to the greatly increased number of elements, and the poor accuracy and computing efficiency in case of large displacements, owing to the high deformation which some soil solid elements are subjected to.

An example of a safety barrier whose posts are embedded into a soil so modeled is shown in Figure A.3.

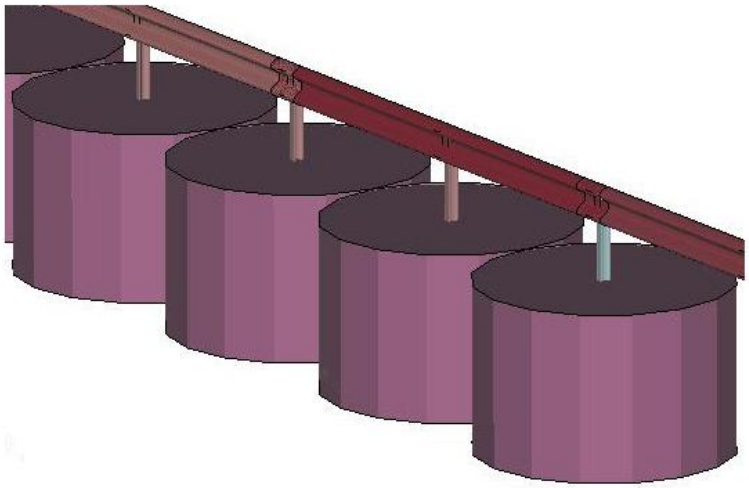

Figure A.3. Example of barrier-soil link: structural cylindrical volumes around the posts [10].

The models so far described are not suitable to correctly represent a bridge safety barrier, since the constraint between the posts and the soil is not realistic at all.

More refined models include the components of the bridge safety barrier anchoring system, which are the anchor bolts (shanks and nuts) and the plates.

Regarding the link between anchor bolts and concrete, there are several ways to model it. The simplest way is by means of merged nodes on the bottom and/or the lateral surface of the bolts and by imposing an adequate contact to avoid every possible penetrations; this can be achieved through a *CONTACT_AUTOMATIC_SURFACE_TO_SURFACE, including the bolts and the concrete in the set of parts which must not penetrate to each other. This contact works only if both the bolts and the concrete are modeled with solid elements.

If the bolts are modeled with beam elements, a more complicated contact should be used, since the beam surface is not considered by the software. In this case, a set of rings of "null beams" must be created on the hole lateral surface, along its entire length, and another "null beam" must be placed in correspondence of the bolt shank; all these "null beams" must be included in a set of parts and the *CONTACT_AUTOMATIC_GENERAL must be assigned to that set. This

kind of contact has been used to model the bolting between the posts and the spacers in the barrier complete model in Chapter 6.
Another way of model the interaction between the anchor bolts and the concrete is the use of a special constraint [23]. In this way, anchor bolts are coupled (rather than merged) to the surrounding concrete. This can be achieved by using the *CONSTRAINED_LAGRANGE_IN_SOLID feature in LS-Dyna®.
Through this constraint, the anchor bolts are treated as a slave part that is coupled with a master part constituted by the concrete. Using this methodology, the slave part can be placed anywhere inside the master part without any special mesh accommodation. Figure A.4 shows two meshing schemes: the one on the left uses merged nodes between beams and solids while the other uses coupling through the *CONSTRAINED_LAGRANGE_IN_SOLID feature between the two parts.

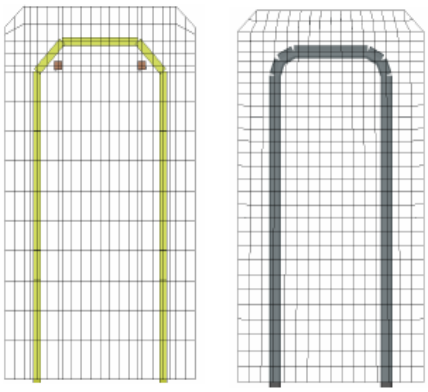

Figure A.4. Comparison between two meshing schemes [23].

This kind of interaction provides an important advantage: it is possible to avoid the holes in the concrete, which results in a simpler and more regular mesh.
None of these models take in consideration the possible failure of the contact between anchor bolts and concrete.

A.2. Verification of the contact used in the model

In this paragraph the two functional tests mentioned in Paragraph 2.2, performed to verify the effectiveness of the contact between anchor bolts and concrete, will be explained in a more detailed way.

In these tests, the bolt is tied to a slab made of the same material; this choice has been made in order to achieve a clearer view of the results, in particular the stress distribution on the slab, when the bolt is pulled.
In the first test, only the bottom surface of the bolt has been tied to the metallic slab. On the opposite surface of the bolt a prescribed linear displacement has been applied, while the bottom surface of the metallic slab has been rigidly constrained.
The *CONTACT_TIED_SURFACE_TO_SURFACE_FAILURE has been imposed between the lower surface of the bolt and the upper surface of the slab. The parameter FS has temporarily and arbitrarily been imposed equal to 100 N/mm^2, since most of the common industrial bonding resins are characterized by values that range from 80 N/mm^2 to 300 N/mm^2. It can be seen that when the axial stress on the bolt, due to the imposed displacement, reaches the settled value, the bolt is detached from the slab. During the time period when the bolt and the slab are tied to each other, a continuous distribution of stress between the two elements can be seen. The graphic in Figure A.5 reports the trend of the axial stress on the contact surface during the test.

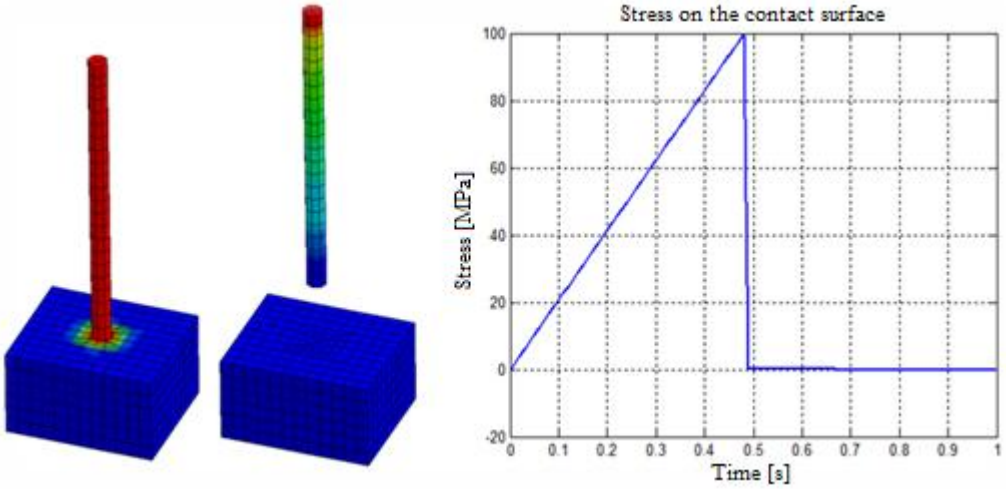

Figure A.5. First functional test of the contact. The graphic shows the trend of the stress on the contact surface.

In the second test, the bolt has been placed inside a drilled slab of the same material. The four lateral surfaces of the slab have been rigidly constrained, and an axial displacement has been applied to the bolt.

Figure A.6 shows a section of the model in correspondence of the hole. The distribution of stresses that the bolt transmits to the slab is clear. As happened in the previous test, once the stress on the contact surface reaches the settled value, the bolt is detached, as if the bonding resin failed.

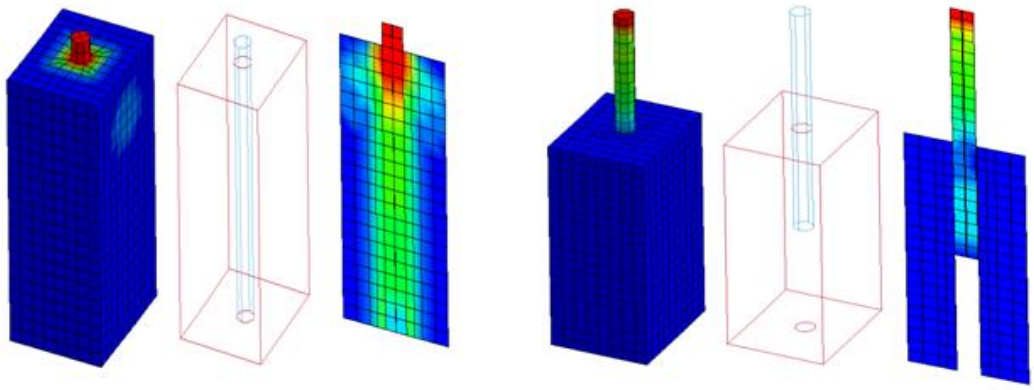

Figure A.6. Second functional test of the contact. The stress is transmitted between the two parts until the detachment.

Even in this model the value of the admissible stress, which in this case is the shear stress FD, has been set to 100 N/mm^2.
Both those parameters, FS and FD, are provisional and should be calibrated by means of experimental tests.

A.3. Introduction of a preloaded state through dynamic relaxation

Numerical models like the one here developed require the introduction of a steady preloaded state before performing the normal transient dynamic analysis. Usually this is due to several reasons, like the presence of rotating fan or turbine blades, rotating flywheels, gravity, pressure vessels, tires or, as in this case, stresses induced by a torque.
Explicit dynamic relaxation is typically used to preload a model before the onset of the regular transient loading. The dynamic relaxation is an optional transient analysis that takes place in a "pseudo-time", which means that precedes the regular transient analysis.
In the explicit dynamic relaxation, the computed nodal velocities are reduced each time-step by the dynamic relaxation factor (whose default value is 0.995).

Thus, the solution undergoes a form of damping during this phase. The preload stresses are typically elastic and the displacements are small.
The distortional kinetic energy is monitored and when it has been sufficiently reduced, i.e., the convergence factor has become sufficiently small, the dynamic relaxation phase terminates and the solution automatically proceeds to the following transient analysis phase. Alternately, dynamic relaxation can be terminated at a preset termination time.
The dynamic relaxation is typically invoked by setting the parameter SIDR in a load curve (settled through the card *DEFINE_CURVE) to 1 or 2. During the dynamic relaxation phase the load must be ramped and then held constant until solution converges. It must be ascertained that the convergence occurs after 100% of preload is applied.
After the dynamic relaxation phase, the preload must be maintained during the subsequent transient analysis phase: for this purpose, a separate load curve, without the ramp, must be set.

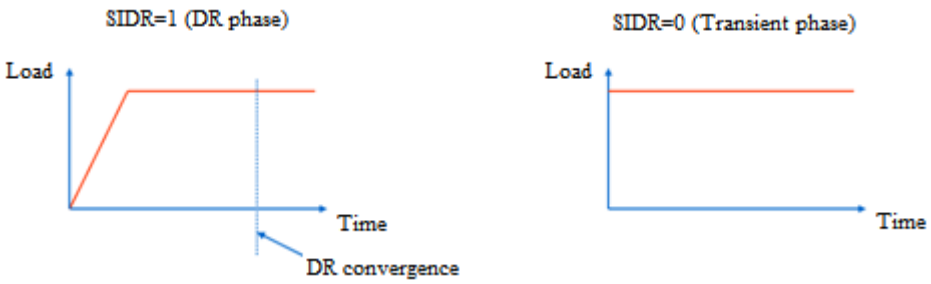

Figure A.7. Load curves to impose for dynamic relaxation and transient phase.

The card *CONTROL_DYNAMIC_RELAXATION can be imposed in order to control the dynamic relaxation phase development. The parameters present in this card are the following [24]:

- NRCYCK: Iterations between convergence check (default = 250).
- DRTOL: Convergence tolerance (default = 0.001), which is the ratio between the distorsional kinetic energy at convergence and its peak; a smaller value results in converged solution nearer to steady state but run takes longer to get there.
- DRFCTR: Dynamic relaxation factor (default = 0.995), that is the reduction factor for nodal velocities at each time-step; if this value is too small, the model never reaches the steady state because of overdamping.

- DRTERM: Optional termination time for dynamic relaxation (default = infinity); dynamic relaxation stops if time reaches DRTERM even if convergence criterion is not satisfied.
- TSSFDR: Time-step scale factor used during dynamic relaxation.
- IDRFLG: Flag to activate the dynamic relaxation (not required if dynamic relaxation is activated with *DEFINE_CURVE). Set to 2, it invokes a completely different and faster initialization approach, which is the initialization through prescribed geometry; it requires a supplemental input file containing nodal displacements and rotations. LS-DYNA® runs a short transient analysis of 100 time-steps to preload the model by imposing the nodal displacements and rotations; the solution then proceeds with regular transient analysis. Set to 5, it activates implicit method for the solution of the preloaded state.

Bolts preload

The models here developed include anchor bolts subjected to a torque. Hence, the preload stress due to this torque has been introduced.
There are four different ways to introduce the bolts preload:

- *LOAD_THERMAL_LOAD_CURVE
- *CONTACT_INTERFERENCE
- *INITIAL_STRESS_SECTION (usable for solid elements only)
- *INITIAL_AXIAL_FORCE_BEAM (usable for type 9 beams only)

In the first case, the idea is to shrink the bolt by cooling it; as bolt contracts during dynamic relaxation phase, the preload is induced.
The coefficient of thermal expansion must be assigned to the material which the bolt is made of via *MAT_ADD_THERMAL_EXPANSION.
A negative temperature variation must be then prescribed through the card *LOAD_THERMAL_LOAD_CURVE. The parameter LCID indicates the curve of temperature vs. time for transient phase (constant temperature), while the parameter LCIDDR indicates the curve of temperature vs. time for dynamic relaxation phase. As previously told, the value of SIDR in *DEFINE_CURVE must be set to 1 for the second curve and to 0 for the first one. In the dynamic relaxation phase, the curve must be constituted by a ramp and a constant part.

The second way to introduce a preload has been developed to model the shrinking of a certain element. The initial geometry must be defined to include

a finite initial penetration between two parts. The concerned parts are initially in an unstressed state; the initial penetration check, which the software usually fulfills, is not done for this contact type.
In order to avoid sudden, large contact forces, the contact stiffness is scaled with time using LCID1 (dynamic relaxation phase) and LCID2 (transient phase).
Shell thickness offsets are considered and segment orientation is important; indeed, the normals must be correctly oriented, that means facing the contact surface.
The types of contacts which fit this solution are:

- *CONTACT_NODES_TO_SURFACE_INTERFERENCE
- *CONTACT_ONE_WAY_SURFACE_ TO_SURFACE_INTERFERENCE
- *CONTACT_SURFACE_TO_SURFACE_INTERFERENCE

The third way consists of preloading a cross-section of a solid element, or a set of solid elements, by imposing therein a known stress. The card *INITIAL_STRESS_SECTION is used to define the section, the elements and the stress to apply.
The preload stress (which must be perpendicular to the cross-section) is settled via *DEFINE_CURVE, as made in the previous cases.
The physical location of cross-section is instead defined via *DATABASE_CROSS_SECTION.
A part set, together with the cross-section, identify the elements subjected to the prescribed preload stress.
The card *DAMPING_PART_STIFFNESS may promote convergence during dynamic relaxation phase.

The fourth technique can be applied when the preloaded element is a beam. The card *INITIAL_AXIAL_FORCE_BEAM is used to preload it by means of a prescribed axial force.
As in the previous cases, two curves must be defined to impose the preload: the first, constituted by a ramp and a constant stretch, to be used during the dynamic relaxation phase, and the second, constant, for the transient phase.
A set including all the beam elements which must be subjected to the imposed preload should be defined. The beam formulation (ELFORM) must be set to 9 (spotweld beam) and the material whose those elements are made of must be *MAT_SPOTWELD.

The card *DAMPING_PART_STIFFNESS may promote convergence during dynamic relaxation phase.

In the developed models, two of these preloading techniques have been used: the thermal contraction of the anchor bolts and the introduction of an axial force in the beam elements of the bolting.

B. Further concrete features

B.1. Concrete special additives

Concrete mixtures are almost always enriched with chemical additives which give them special further properties; the additives mostly used are the followings:

- Accelerators: they speed up the hydration (hardening) of the concrete. Typical materials used are $CaCl_2$, $Ca(NO_3)_2$ and $NaNO_3$. However, the usage of chlorides may cause corrosion of steel reinforcements and is prohibited in some countries, so that nitrates may be favored.
- Retarders: they slow the hydration of concrete and are used in large or difficult pours where a partial hardening before the pour is complete is undesirable; typical retarders are sucrose, sodium gluconate, glucose, citric acid and tartaric acid.
- Air entrainments: they add and entrain tiny air bubbles in the concrete, which reduces damage during freeze-thaw cycles, increasing durability. However, entrained air entails a strength reduction, as each 1% of air may decrease compressive strength of 5%.
- Plasticizers: they increase the workability of "fresh" concrete, allowing it to be placed more easily, with less consolidating effort. A typical plasticizer is lingosulfonate. Plasticizers can be used to reduce the water content of a concrete while maintaining workability and are sometimes called water-reducers because of this use. Such treatment improves its strength and durability characteristics. Superplasticizers (also called high-range water-reducers) are a class of plasticizers that have fewer deleterious effects and can be used to increase workability more than traditional plasticizers can do. Compounds used as superplasticizers include sulfonated naphthalene formaldehyde condensate, sulfonated melamine formaldehyde condensate, acetone formaldehyde condensate and polycarboxylate ethers.
- Pigments: they are used to change the color of concrete, for aesthetics.
- Corrosion inhibitors: they are used to minimize the corrosion of steel and steel bars in concrete.
- Bonding agents: they are used to create a bond between old and new concrete (typically they are polymers).
- Pumping aids: they improve pumpability, by thickening the paste and reducing separation and bleeding.

B.2. Concrete classification according to consistency

The concrete workability, indicated as consistency from the regulations, is the ability of the fresh concrete to properly fill the form/mold, with the desired work (vibration) and without reducing the concrete quality. The workability depends on the water content, the aggregates (shape, size and distribution), the cement content and the age (level of hydration) and can be modified by adding chemical admixtures, like superplasticizers. Raising the water content or adding chemical admixtures increases concrete workability.
According to the regulations [12], consistency is measured by means of the following methods:

- Concrete slump test
- Vebè test
- Measurement of compactibility
- Measurement of the spreading

The concrete slump test is carried out using a mold known as slump cone or Abrams cone. The cone is placed on a hard non-absorbent surface. It is then filled with fresh concrete in three stages, and each time it is tamped using a rod of standard dimensions. At the end of the third stage, concrete is struck off flush to the top of the mold. The mold is carefully lifted vertically upwards, so as not to disturb the concrete cone. Then concrete subsides and this subsidence, termed as slump, is measured.

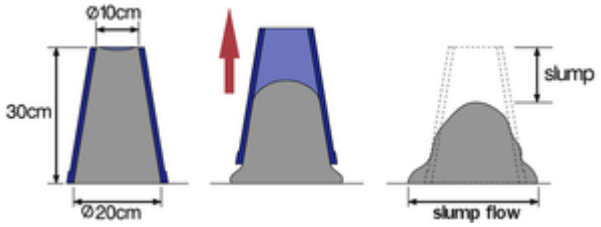

Figure B.1. Abrams cone and slump.

The Vebè method consists of the measurement of the time that concrete takes to cover a disk of a certain size, after being placed into the Abrams cone and subjected to vibrations.
The consistency classes, according to the above described criteria, are described in Tables B.1, B.2, B.3 and B.4.

Table B.1. Concrete classification according to the slump length.

Class	Slump [mm]
S1	10-40
S2	50-90
S3	100-150
S4	160-210
S5	≥220

Table B.2. Concrete classification according to the Vebè time.

Class	Vebè time [s]
V0	≥31
V1	30-21
V2	20-11
V3	10-6
V4	5-3

Table B.3. Concrete classification according to the compactibility.

Class	Compactibility index
C0	1.46
C1	1.45-1.26
C2	1.25-1.11
C3	1.10-1.04
C4	≤1.04

Table B.4. Concrete classification according to the spreading diameter.

Class	Spreading diameter [mm]
F1	≤340
F2	350-410
F3	420-480
F4	490-550
F5	560-620
F6	≥630

B.3. Other concrete numerical models

In this paragraph two further concrete numerical models, not considered in this work, will be shortly described [25].

Karagozian & Case concrete model

Intended for analyzing reinforced concrete structural responses to blast and impact loadings, this model allows automatic generation of all the parameters by inputting only the unconfined compressive strength and the density of concrete.
The KCC model has three independent strength surfaces and they can be formulated in a generalized form as:

$$F_i(p) = a_{0i} + \frac{p}{a_{1i} + a_{2i} \cdot p} \qquad (B.1)$$

where i = y, m, r, i.e., the yield strength surface, the maximum strength surface, and the residual strength surface, p is the pressure and a_{ji} (j = 0, 1, 2) are parameters calibrated from test data.
The failure surface is interpolated between the maximum strength surface and either the yield strength surface or the residual strength surface according to the following form:

$$F(I_1, J_2, J_3) = \begin{cases} r(J_3) \cdot \left[\eta(\lambda) \cdot \left(F_m(p) - F_y(p)\right) + F_y(p)\right] & \lambda \leq \lambda_m \\ r(J_3) \cdot \left[\eta(\lambda) \cdot \left(F_m(p) - F_r(p)\right) + F_r(p)\right] & \lambda > \lambda_m \end{cases} \qquad (B.2)$$

Here λ is the modified effective plastic strain or the internal damage parameter, which is a function of J_2 and other parameters (such as damage evolution parameter, hardening parameter). η(λ) is a function of the internal damage parameter λ, with η(0) = 0, $\eta(\lambda_m) = 1$, and $\eta(\lambda \geq \lambda_{max}) = 0$. This implies that the failure surface starts at the yield strength surface, and it reaches the maximum strength surface as λ increases to λ_m, and then it drops to the residual surface as λ further increases up to λ_{max}. λ_m, λ_{max}, and η(λ) are calibrated from experimental data. $r(J_3)$ is a scale factor in the form of William-Warnke equation, which

introduces the dependence to J_3 so that brittle (under low confinement) to ductile transition (under high confinement) is properly modeled.
The KCC model can properly capture the key concrete behaviors including post-peak softening, confinement effect, and strain rate effect. Structural analyses also show that the KCC model is suitable for quasi-static, blast and impact loads.

Winfrith model

The Winfrith concrete model is based upon the so called "four parameter model" proposed by Ottosen:

$$Y(I_1, J_2, J_3) = a \cdot J_2 + \lambda \cdot \sqrt{J_2} + b \cdot I_1 - 1 \qquad (B.3)$$

$$\lambda = \begin{cases} k_1 \cdot \cos\left[\frac{1}{3} \cdot \cos^{-1}(k_2 \cdot \cos(3 \cdot \theta))\right] & \cos(3 \cdot \theta) \geq 0 \\ k_1 \cdot \cos\left[\frac{\pi}{3} - \frac{1}{3} \cdot \cos^{-1}(-k_2 \cdot \cos(3 \cdot \theta))\right] & \cos(3 \cdot \theta) < 0 \end{cases} \qquad (B.4)$$

$$\cos(3 \cdot \theta) = \frac{3 \cdot \sqrt{3}}{2} \cdot \frac{J_3}{J_2^{\frac{3}{2}}} \qquad (B.5)$$

The four parameters a, b, k_1, and k_2 are functions of the ratio of tensile strength to compressive strength (f_t/f_c'), and they are determined from uniaxial compression, uniaxial tension, biaxial compression and triaxial compression tests.
The Winfrith model can model post-peak softening in tension but not compression. It can also simulate strain rate effect and confinement effect.
An attractive feature of this model is that it allows up to three orthogonal crack planes per element and the cracks are viewable through LS-Prepost®. However, the Winfrith model cannot represent shear dilation, therefore, the confinement effect exerted by reinforcements, such as steel stirrups and fiber reinforced polymer wraps, will not be predicted correctly with this model.

Nomenclature and list of acronyms

Nomenclature

A_{res}	Area of the resistant section
a_x	Average longitudinal acceleration
a_y	Average transversal acceleration
a_z	Average vertical acceleration
C_H	Elasticity limit surface second coefficient
D	Dynamic Deflection
d	Scalar damage parameter
d_{max}	Maximum damage level
d_n	Nominal diameter
E	Young's modulus
E_c	Instantaneous tangent modulus
E_{cm}	Instantaneous secant modulus
f	Shear surface equation
f_t	Concrete tensile strength
f'	Concrete strength in uniaxial stress state
F_C	Cup surface
f_{ck}	Concrete characteristic cylindrical strength
G	Shear modulus
I_1	First invariant of stress tensor
J	Moment of inertia
J_2	Second invariant of deviatoric stress tensor
J_3	Third invariant of deviatoric stress tensor
K	Bulk modulus
L_c	Level of containment
M	Mass
N_F	Axial force at failure
N_H	Elasticity limit surface first coefficient
p	Pressure
R	Rubin's function
r_0	Dynamic energy threshold
r_{0b}	Brittle damage threshold
r_{0d}	Ductile damage threshold

R_{ck}	Concrete characteristic cubic strength
R_F	Shear force at failure
r^s	Static energy threshold
$\mathbf{T}$	Stress tensor
$\mathbf{T_d}$	Deviatoric stress tensor
V	Velocity
v_x	Component of the vehicle velocity along the x local axis
v_y	Component of the vehicle velocity along the y local axis
W	Working Width
X	Cup surface ending point
Y	Yield function
α	Coefficient of thermal expansion
α	Triaxial compression surface constant term
α_1	Triaxial torsion surface constant term
α_2	Triaxial tension surface constant term
β	Angle of friction
β	Triaxial compression surface exponent
β_1	Triaxial torsion surface exponent
β_2	Triaxial tension surface exponent
γ	Angle of inclination of the thread
δ_{ij}	Kronecker's delta
ΔT	Temperature variation
ε	Strain
ε_1	Axial strain
ε_3	Lateral strain
ε_{c1}	Concrete strain at maximum strength
ε_{cu}	Concrete ultimate strain
ε_{ij}	Strain components
ε_{max}	Maximum principal strain
ε_r	Rupture strain
ε_v	Volumetric strain
$\dot{\varepsilon}$	Strain rate
θ	Triaxial compression surface linear term
θ_1	Triaxial torsion surface linear term
θ_2	Triaxial tension surface linear term
κ	Cup surface beginning point
λ	Triaxial compression surface non-linear term

λ_1	Triaxial torsion surface non-linear term
λ_2	Triaxial tension surface non-linear term
μ	Coefficient of friction
ν	Poisson's ratio
ρ	Density
σ	Stress
σ_1	First principal stress
σ_2	Second principal stress
σ_3	Third principal stress
σ_{cu}	Concrete ultimate stress
σ^d	Stress tensor with damage in uniaxial stress state
σ_{ij}	Stress components
σ_{ij}^d	Stress tensor with damage
σ_{ij}^{vp}	Stress tensor without damage
σ_{pr}	Preload stress
σ_r	Rupture stress
σ_y	Yield stress
τ	Shear stress
τ_b	Brittle damage parameter
τ_d	Ductile damage parameter
τ_r	Shear stress at failure

List of acronyms

ABS	Antilock brake system
ASI	Acceleration severity index
CSC	Continuous surface cap
DAT	Daily average traffic
EN	Norme Européenne - European Standard
ESP	Electronic stability program
FE	Finite elements
HGV	Heavy goods vehicles
HPC	High performances concretes
HSC	High strength concretes
HSC	Hydrostatic compression test
KCC	Karagozian & Case concrete
NSC	Normal strength concretes

PHD Post-impact head deceleration
SD Principal stress difference
THIV Theoretical head impact velocity
TXC Triaxial compression test
TXE Triaxial extension test
UTC Uniaxial compression test
UXE Uniaxial strain test
V&V Validation and verification
VI Vehicle intrusion

Bibliography

[2] *European Standard EN 1317-2. Performance classes, impact test acceptance criteria and test methods for safety barriers including vehicle parapets.* **European Committee for Standardization.**

[6] *ETAG 001 – Guideline for European Technical Approval. Metal anchors for use in concrete; part one: anchors in general.* **EOTA – European Organisation for Technical Approvals.**

[7] *ETAG 001 – Guideline for European Technical Approval. Metal anchors for use in concrete; part five: bonded anchors.* **EOTA – European Organisation for Technical Approvals.**

[8] *ETAG 001 – Guideline for European Technical Approval. Metal anchors for use in concrete; annexes C: anchors design methods.* **EOTA – European Organisation for Technical Approvals.**

[9] *Aspetti di interazione tra barriere di sicurezza ed opere d'arte.* **Lorenzo Domenichini, Francesca La Torre, Flavio Caputo.** Convegno Ponti e Viadotti – Aspetti progettuali, strutturali e di manutenzione. Pistoia, 28.09.2006

[10] *Modellazione euleriana del suolo per simulazioni di impatto con barriere stradali*. **Matteo Catania.** Politecnico di Milano, 2006.

[11] *Cemento armato, calcolo agli stati limite.* **Giandomenico Toniolo.** Masson S.p.A., 1996.

[12] *European Standard EN 206 – 1. Concrete – Part 1: Specification, performance, production and conformity*. **Unicemento.** 2006.

[13] *Etude et modélisation du dommage du béton sous une compression uniaxiale*. **Aurélien De Wolf, Coraline Guyot.** École Polytechnique de Louvain, 2011.

[14] *Etude et modélisation du béton sous chargement dynamique*. **Piedboeuf François, Vandervlies Loïc.** École Polytechnique de Louvain, 2010.

[15] *Users Manual for LS-Dyna Concrete Material Model 159.* **Livermore Software Technology corporation.** 2007.

[16] *Laboratory Tests for Characterizing Geomaterials.* **Len Schwer.** 2001

[17] *Parametric analysis of road safety barriers*. **Elena Di Silvestro.** Politecnico di Milano, 2013.

[18] *Il progetto della sicurezza stradale: i sistemi di contenimento dei veicoli.* **Andrea Demozzi.** Trento, 2004.

[19] *European Standard EN 1317-1. Terminology and general criteria for test methods.* **European Committee for Standardization.**

[20] *L'urto più probabile.* **Aurelio Marchionna, Paolo Perco.** Le Strade n°4/2009.

[21] *European Standard EN 1317-5. Certification of compliance.* **European Committee for Standardization.**

[22] *Computational simulations of road safety barriers using LS-Dyna.* **Matej Vesenjak, Matej Borovinšek, Zoran Ren.** LS-Dyna Anwenderforum, Frankenthal, 2007.

[23] *Application of New Concrete Model to Roadside Safety Barriers.* **Akram Abu-Odeh.** 9th International LS.Dyna Users Conference.

[24] *LS-Dyna Keyword User's Manual – Version 971*. **Livermore Software Technology corporation.** 2007.

[25] *Performance of LS-Dyna Concrete Constitutive Models.* **Youcai Wu, John E. Crawford, Joseph M. Magallanes.** 12th International LS.Dyna Users Conference.

[26] *LS-Dyna Theory Manual*. **John O. Hallquist.** 2006.

Webography

[1] *dati.istat.it*

[3] *www.lanazione.it*

[4] *www.ansa.it*

[5] *www.automoto.it*